Study of near-surface aerosols by means of concurrent observations with satellite sensors and ground-based instruments

衛星センサと地上測器の同時観測による地上付近のエアロゾル計測

January 2019

Jamrud Aminuddin

ジャムルドアミヌディン

Graduate School of

Advanced Integration Science

CHIBA UNIVERSITY

(千葉大学審査学位論文)

Study of near-surface aerosols by means of concurrent observations with satellite sensors and ground-based instruments

衛星センサと地上測器の同時観測による地上付近のエアロゾル計測

January 2019

Jamrud Aminuddin

ジャムルドアミヌディン

Graduate School of

Advanced Integration Science

CHIBA UNIVERSITY

ENDORSEMENT

This doctoral thesis with the title of **Study of near-surface aerosols by means of concurrent observations with satellite sensors and ground-based instruments** has been defended in the doctoral examination at the Graduate School of Integrated Sciences and Technology, Chiba University, Japan.

To cite this work, feel free to copy and paste the following:

Aminuddin J. (2019). **Study of near-surface aerosols by means of concurrent observations with satellite sensors and ground-based instruments**. Hiroaki Kuze (supervisor). Doctoral Thesis. Graduate School of Advanced Integrated Science – Chiba University, Japan.

Chiba-Japan, January, 2019

Author,

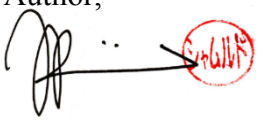

Jamrud Aminuddin

Doctoral Student at Center for Environmental Remote Sensing
Chiba University-Japan

Supervisor,

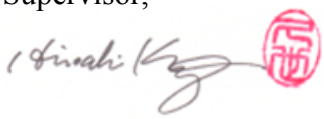

Hiroaki Kuze,

Professor at Center for Environmental Remote Sensing
Chiba University-Japan

SUMMARY

Aerosol particles are emitted from both natural and anthropogenic sources near the surface level and affect the radiation budget as well as the atmospheric environment. The existing approaches for aerosol measurement are either from satellite sensors or ground-based observations, providing data on regional or local scale environment, respectively. In the present research, a comprehensive method of investigating near-surface aerosol is proposed on the basis of the concurrent observations and analyses of the data from both space- and ground-based measurements. For the ground-based part, lidar data from plan-position indicator (PPI), slant-path, and vertical lidars are analyzed to monitor the spatial distribution and temporal variation of the aerosol extinction coefficient. For solving the lidar equation, ancillary data of the scattering coefficient, absorption coefficient, and size distribution are obtained from an integrating nephelometer, an aethalometer, and optical particle counters, respectively, and used to calculate the value of the lidar ratio. Also, a sunphotometer provides the aerosol optical thickness (AOT) during the daytime. The information on the spatial distribution of AOT, on the other hand, is obtained from the analysis of visible-band images of Landsat-8 and Himawari-8 satellites. The radiative transfer calculation is conducted using the MODTRAN code with the original aerosol type that has been determined from the ground sampling data coupled with the Mie scattering calculation. As a whole, the methodology proposed in this work has demonstrated the usefulness of such a comprehensive approach for studying aerosol behavior in the lower troposphere, where most of the sources of particles are located.

SUMMARY (JAPANESE)

エアロゾル粒子は、地表面付近の自然放出源や人為放出源から放出され、大気環境だけでなく放射収支にも影響を及ぼす。エアロゾル測定の既存の手法としては、衛星センサによる方法と地上観測の方法があり、それぞれ地域的環境またはその場の環境に関するデータを提供する。本研究では、宇宙および地上ベースの同時測定データの解析に基づき、地表エアロゾルを観測する包括的な方法を提案する。地上観測においては、PPI ライダー、斜め観測ライダー、鉛直ライダーからのデータを解析し、エアロゾル消散係数の時空間分布を導出する。ライダー方程式を解くために必要なライダー比は、散乱係数、吸収係数、粒径分布に関するデータを積分型ネフェロメータ、エーサロメーター、光学的粒子カウンターからそれぞれ取得し、Mie 散乱の計算を行って推定する。また、サンフォトメータにより、昼間のエアロゾル光学厚さ（AOT）を取得する。一方、Landsat-8 およびひまわり 8 号衛星の可視域画像の解析からは、AOT の空間分布に関する情報が得られる。MODTRAN コードを使用して放射伝達計算を行うが、その際に必要となるエアロゾル光学特性は、地上サンプリングデータをもとに Mie 散乱計算を行うことにより取得する。本研究は、全体として、ここで提案した包括的アプローチは、大部分の粒子発生源が存在する下部対流圏におけるエアロゾルの挙動を明らかにするために有用であることを実証した。

ACKNOWLEDGEMENT

I wish to thank my supervisor, Prof. Hiroaki Kuze, for his support, guidance, and collaboration in completing my doctoral study at the Center for Environmental Remote Sensing (CEReS) – Chiba University, Japan.

I also wish to appreciate the collaboration of all member of CEReS-Chiba University throughout the time period when I carried out my research. I wish to thank Dr. Naohiro Manago for his collaboration and guidance in setting instrument and processing data in python under Linux.

Also I am highly grateful to the Directorate General of Resource for Research, Technology and Higher Education (DG-RSTHE), the Ministry of Research, Technology, and the Higher Education Republic of Indonesia, for their financial support in my doctoral study with a program named BEASISWA DIKTI.

I also appreciate the administrative support from my institution, Department of Physics, Faculty of Mathematics and Natural Science, Universitas Jenderal Soedirman, Purwokerto, Indonesia.

Finally, and most significantly, I express my love and gratitude for my wife Veny Solihani, my first son Ahmad Giza Aminuddin, and my second son Muhammad Ghaisan Aminuddin for their togetherness, spirit, and patience to wait me for finishing my doctoral study.

Chiba-Japan, January, 2019

Jamrud Aminuddin

TABLE OF CONTENTS

TITLE PAGE ii
ENDORSEMENT iii
SUMMARY iii
SUMMARY (JAPANESE) iv
ACKNOWLEDGEMENT v
TABLE OF CONTENTS vi
LIST OF FIGURES ix
LIST OF TABLES xvii
LIST OF SYMBOLS AND ABBREVIATION xviii
1. INTRODUCTION 1
1.1 Research Background 1
1.2 Research Purposes 3
1.3 Significance of Research 4
2. SCIENTIFIC BACKGROUND AND THEORY 5
2.1 Aerosol Optical Properties 5
2.2 Ground Based-Sampling Instruments 6
2.3 Lidar Ratio Calculation 10
2.4 Lidar Measurement and Fernald Method 12
2.5 Aerosol Optical Thickness and Sunphotometer 15
2.6 Ångström Exponent 18
2.7 Landsat-8 Satellite 18
2.8 Himawari-8 Satellite 20
2.9 Radiative Transfer Calculation 22
2.10 Atmospheric Parameters and Weather Detector 24
2.11 Correction and Fitting 25
3. INSTRUMENTS AND METHODS 27
3.1 The Monitoring Technique and Location 27

3.2 Weather Monitor and Atmospheric Parameters 29
3.3 Aerosol Extinction Coefficient of Sampling Instruments and Mie Scattering Calculation..... 31
3.4 Aerosol Extinction Coefficient of Lidar System 39
3.5 Aerosol Optical Thickness of Ground Measurement 45
3.6 Aerosol Optical Thickness of Satellite Data 50
4. RESULTS AND DISCUSSION 53
4.1 Results 53
4.1.1 Atmospheric Condition..... 53
4.1.2 Extinction Coefficient of Sampling Instruments 54
4.1.3 Extinction to Backscattering Ratio 59
4.1.4 Extinction Coefficient of Lidars System 64
4.1.5 AOT of Sunphotometer and Skyradiometer 67
4.1.6 Ångström Exponent 72
4.1.7 Apparent Reflectance..... 74
4.1.8 Observed Radiance 78
4.1.9 Look up Table and Surface Reflectance 82
4.1.10 AOT Derived from Satellite Observation..... 84
4.2 Analysis and Discussion..... 89
4.2.1 Atmospheric and Aerosol Characterizations using Ground Instruments 89
4.2.2 Correlation between space distribution of AEC and AOT of the Blue-band of Satellites..... 90
4.2.3 Correlation between the Temporal change of AEC and AOT of the Green-band of Satellites..... 93
5. CONCLUSIONS AND RECOMMENDATION 98
5.1 Conclusions 98
5.2 Recommendation 100
REFERENCES.....102
APPENDIX A : SCATTERING THEORY 109
APPENDIX B : FERNALD METHOD.....113

APPENDIX C : TRANSMITTANCE AND RADIANCE 117
APPENDIX D : INTERPOLATION METHOD 121

LIST OF FIGURES

Figure 2.1: The scheme of three-wavelength integrating nephelometer (TSI, Model 3563) with backscatter photomultiplier tube housing, backscattering shutter, sensing volume, and additional sensors (temperature, humidity, and pressure). (http://www.tsi.com/ integrating-nephelome-ter-3563/)8

Figure 2.2: The scheme of an aethalometer algorithm in reporting BC concentration, completed by sample spot area, a column of the aerosol sample, filter, light source, sample light detector, and reference light detector..... 9

Figure 2.3: Block diagram of OPC in detecting aerosol size distribution. The OPC completed by laser beam, lens, and detector. (http://www.rion.co.jp)10

Figure 2.4: A principle of lidar measurement. The pulse from the generator is transmitted by laser expander. The inverted signal scattered by atmospheric aerosol is detected by telescope, then collected in the transient recorder. A personal computer controls the system. 13

Figure 2.5: A principle of sunphotometer in measuring solar intensity..... 16

Figure 2.6: Langley plot principle to determine solar intensity at TOA..... 16

Figure 2.7: Himawari-8 observation area and frequencies. The full disk is recorded every 10 minutes, three regions (1,2,3) are collected every 2.5 minute, and two others regions (5 and 6) are covered every 0.5 minutes..... 20

Figure 2.8: The scheme of RT formulation by Chandrasekhar which was taken. The scheme consists of six-components including surface reflectance and scattering in the atmosphere to compute the RT using MODTRAN. 23

Figure 3.1: The area of interest, the Center for Environmental Remote Sensing (CEReS) - Chiba University-Japan where the ground-based instrument and lidar systems are installed..... 27

Figure 3.2: Flowchart of the new monitoring technique..... 28

Figure 3.3: Weather monitor installed in CEReS-Chiba University for monitoring the temporal change of ambient RH, temperature, air pressure, wind speed, and wind direction..... 29

Figure 3.4: Weather monitor data in 2016-10-27..... 30

Figure 3.5: Weather monitor data in 2017-01-31..... 30

Figure 3.6: Weather monitor data in 2017-03-20..... 31

Figure 3.7: Weather monitor data in 2016-05-23..... 31

Figure 3.8: The ground-based sampling instruments (a nephelometer, an aethalometer, and an optical particle counter) installed on the 9th-floor engineering building..... 32

Figure 3.9: Nephelometer data in 2016-10-27. 33

Figure 3.10: Aethalometer data in 2016-10-27. 33

Figure 3.11: Optical particle counter data in 2016-10-27. 33

Figure 3.12: Nephelometer data in 2017-01-31. 34

Figure 3.13: Aethalometer data in 2017-01-31. 34

Figure 3.14: Optical particle counter data in 2017-01-31. 34

Figure 3.15: Nephelometer data in 2017-03-20. 35

Figure 3.16: Aethalometer data in 2017-03-20. 35

Figure 3.17: Optical particle counter data in 2017-03-20. 35

Figure 3.18: Nephelometer data in 2017-05-23. 36

Figure 3.19: Aethalometer data in 2017-05-23. 36

Figure 3.20: Optical particle counter data 2017-05-23. 36

Figure 3.21: The truncation correction of AEC for correcting the sampling procedure which is resulted from comparison between the sampling measurement (x) and the optical measurement (y). All the data involved in this procedure are combination of lower and higher RH for the periods of March and May, respectively. 37

Figure 3.22: The visibility-meter with the wavelength 550 nm installed on the 9th floor of engineering building..... 38

Figure 3.23: The PPI lidar installed on the 9th floor of engineering building is collected signal by rotating 360 near horizontal direction (~4 degrees). 40

Figure 3.24: The SP lidar installed on the 5th floor of CEReS building in the area of Chiba University with the signal in the north direction and ~30 degrees from the horizontal direction..... 41

Figure 3.25: The NIES lidar installed on Chiba University-Nishi Chiba Campus. 42

Figure 3.26: Instrument alignment and signal monitoring of PPI lidar. 42

Figure 3.27: Instrument alignment and signall monitoring of SP lidar..... 43

Figure 3.28: Lidar system installed in CEReS, Chiba University-Japan. 43

Figure 3.29: Sample of the raw signal, Corrected signal, and extinction coefficient of (a) PPI and (b) SP lidars in 2017-05-23. The PPI range signal is shorter than SP's, but the extinction coefficient of PPI in the far-end boundary layer is higher than SP's. The sample of this signal processing is computed using the Fernald method. This processing is implemented for all data in this study. The complete results in the spatial distribution of PPI and temporal change of SP are presented in Chapter 4: Results and Discussion..... 44

Figure 3.30: (a) The four-wavelength sunphotometer (368, 500, 678, and 778 nm) installed at the 5th floor of CEReS building, (b) The seven-wavelength (340, 380, 400, 500, 675, 870, and 1020 nm) of skyradiometer installed on the 9th floor of engineering building..... 46

Figure 3.31: The truncation correction of AOT for correcting the sampling procedure which is resulted from comparison between the sunphotometer (x) and the sampling procedure (y). All the data involved in this procedure are combination of lower and higher RH for the periods of March and May, respectively. 46

Figure 3.32: Data observed in 2017-02-12 on the clearest sky condition to determine the extra-terrestrial intensity of solar radiation. 47

Figure 3.33: Langley plot of the sunphotometer data observed on February 12, 2017. The extrapolation resulted logarithm of solar radiation at the top of atmosphere for every wavelengths (a) ln $I(369)$ = -14.797, (b) ln $I(500)$ = -13.383, (c) ln $I(675)$ = -13.119, and (d) ln $I(778)$ = -14.151. 47

Figure 3.34: (a) solar position and (b) sunphotometer data in 2016-10-27. 48

Figure 3.35: Total ozone in 2016-10-27 for Chiba area 247 DU (Dobson Unit). 48

Figure 3.36: (a) solar position and (b) sunphotometer data in 2017-01-31. 48

Figure 3.37: Total ozone in 2017-01-31 for Chiba area 314 DU (Dobson Unit). 49

Figure 3.38: (a) solar position and (b) sunphotometer data in 2017-03-20. 49

Figure 3.39: Total ozone in 2017-03-20 for Chiba area 303 DU (Dobson Unit). 49

Figure 3.40: (a) solar position and (b) sunphotometer data in 2017-05-23. 50

Figure 3.41: Total ozone in 2017-05-23 for Chiba area 289 DU (Dobson Unit). 50

Figure 3.42: Spectral response function of blue bands. 52

Figure 3.43: Spectral response function of green bands. 52

Figure 4.1: The atmospheric condition in 2016-10-27..... 53

Figure 4.2: The atmospheric condition in 2017-01-31..... 54

Figure 4.3: The atmospheric condition in 2017-03-20..... 54

Figure 4.4: The atmospheric condition in 2017-05-23..... 54

Figure 4.5: Extinction coefficient of sampling instruments in 2016-10-27. 55

Figure 4.6: Extinction coefficient of sampling instruments in 2017-01-31. 56

Figure 4.7: Extinction coefficient of sampling instruments in 2017-03-20. 56

Figure 4.8: Extinction coefficient of sampling instruments in 2017-05-23. 57

Figure 4.9: The corrected extinction coefficient in 2017-05-23 with $f(RH)$ correction..... 57

Figure 4.10: Interpolated extinction coefficient in 2016-10-27. 58

Figure 4.11: Interpolated extinction coefficient in 2017-01-31. 58

Figure 4.12: Interpolated extinction coefficient in 2017-03-20. 59

Figure 4.13: Interpolated extinction coefficient in 2017-05-23. 59

Figure 4.14: Mie scattering calculation in 2016-10-27. 60

Figure 4.15: Mie scattering calculation in 2017-01-31. 61

Figure 4.16: Mie scattering calculation in 2017-03-20. 61

Figure 4.17: Mie scattering calculation in 2017-05-23. 62

Figure 4.18: Temporal variation of lidar ratio in 2016-10-27..... 62

Figure 4.19: Temporal variation of lidar ratio in 2017-01-31..... 63

Figure 4.20: Temporal variation of lidar ratio in 2017-03-20..... 63
Figure 4.21: Temporal variation of lidar ratio in 2017-05-23..... 63
Figure 4.22: Spatial distribution of extinction coefficient in 2016-10-27. 64
Figure 4.23: Spatial distribution of extinction coefficient in 2017-01-31. 64
Figure 4.24: Spatial distribution of extinction coefficient in 2017-03-20. 65
Figure 4.25: Spatial distribution of extinction coefficient in 2017-05-23. 65
Figure 4.26: Temporal distribution of extinction coefficient in 2016-10-27. 66
Figure 4.27: Temporal distribution of extinction coefficient in 2017-01-31. 66
Figure 4.28: Temporal distribution of extinction coefficient in 2017-03-20. 66
Figure 4.29: Temporal distribution of extinction coefficient in 2017-05-23. 67
Figure 4.30: The temporal change of AOT in 2016-10-27. 67
Figure 4.31: The temporal change of AOT in 2017-01-31. 68
Figure 4.32: The temporal change of AOT in 2017-03-20. 68
Figure 4.33: The temporal change of AOT in 2017-05-23. 68
Figure 4.34: Interpolated AOT of sunphotometer in 2016-10-27. 69
Figure 4.35: Interpolated AOT of sunphotometer in 2017-01-31. 69
Figure 4.36: Interpolated AOT of sunphotometer in 2017-03-20. 70
Figure 4.37: Interpolated AOT of sunphotometer in 2017-05-23. 70
Figure 4.38: Interpolated AOT of skyradiometer in 2016-10-27..... 70
Figure 4.39: Interpolated AOT of skyradiometer in 2017-01-31..... 71
Figure 4.40: Interpolated AOT of skyradiometer in 2017-03-20..... 71
Figure 4.41: Interpolated AOT of skyradiometer in 2017-05-23..... 71
Figure 4.42: The temporal variability of Ångström exponent in 2016-10-27..... 72
Figure 4.43: The temporal variability of Ångström exponent in 2017-01-31..... 73
Figure 4.44: The temporal variability of Ångström exponent in 2017-03-20..... 73

Figure 4.45: The temporal variability of Ångström exponent in 2017-05-23..... 73

Figure 4.46: Apparent reflectance of Himawari-8 before overpass in 2016-10-27. 74

Figure 4.47: Apparent reflectance of Landsat-8 in 2016-10-27..... 75

Figure 4.48: Apparent reflectance of Himawari-8 after overpass in 2016-10-27. 75

Figure 4.49: Apparent reflectance of Himawari-8 before overpass in 2017-01-31. 75

Figure 4.50: Apparent reflectance of Landsat-8 in 2017-01-31..... 76

Figure 4.51: Apparent reflectance of Himawari-8 after overpass in 2017-01-31. 76

Figure 4.52: Apparent reflectance of Himawari-8 before overpass in 2017-03-20. 76

Figure 4.53: Apparent reflectance of Landsat-8 in 2017-03-20..... 77

Figure 4.54: Apparent reflectance of Himawari-8 after overpass in 2017-03-20. 77

Figure 4.55: Apparent reflectance of Himawari-8 before overpass in 2017-05-23. 77

Figure 4.56: Apparent reflectance of Landsat-8 in 2017-05-23..... 78

Figure 4.57: Apparent reflectance of Himawari-8 after overpass in 2017-05-23. 78

Figure 4.58: Radiance in 2016-10-27 with H8-BOP (SZA=51.49 and SAA=156.90), L8-OP (SZA=51.42 and SAA=158.88), and H8-AOP (SZA=50.74 and SAA=159.88). 80

Figure 4.59: Radiance in 2017-01-31 with H8-BOP (SZA=58.34 and SAA=150.86), L8-OP (SZA=58.14 and SAA=152.51), and H8-AOP (SZA=57.39 and SAA=153.44). 80

Figure 4.60: Radiance in 2017-03-20 with H8-BOP (SZA=41.17 and SAA=141.76), L8-OP (SZA=40.55 and SAA=143.42), and H8-AOP (SZA=39.96 and SAA=145.12). 81

Figure 4.61: Radiance in 2017-05-23 with H8-BOP (SZA=24.16 and SAA=122.73), L8-OP (SZA=23.47 and SAA=125.76), and H8-AOP (SZA=22.49 and SAA=126.88). 81

Figure 4.62: LUT of Landsat-8 and Himawari-8 satellites in 2016-10-27. 82

Figure 4.63: LUT of Landsat-8 and Himawari-8 satellites in 2017-01-31. 83

Figure 4.64: LUT of Landsat-8 and Himawari-8 satellites in 2017-03-20. 83

Figure 4.65: LUT of Landsat-8 and Himawari-8 satellites in 2017-05-23. 84

Figure 4.66: AOT of Himawari-8 before Landsat-8 overpass in 2016-10-27. 85

Figure 4.67: AOT of Landsat-8 in 2016-10-27. 85

Figure 4.68: AOT of Himawari-8 after Landsat-8 overpass in 2016-10-27. 85

Figure 4.69: AOT of Himawari-8 before Landsat-8 overpass in 2017-01-31. 86

Figure 4.70: AOT of Landsat-8 in 2017-01-31. 86

Figure 4.71: AOT of Himawari-8 after Landsat-8 overpass in 2017-01-31. 86

Figure 4.72: AOT of Himawari-8 before Landsat-8 overpass in 2017-03-20. 87

Figure 4.73: AOT of Landsat-8 in 2017-03-20. 87

Figure 4.74: AOT of Himawari-8 after Landsat-8 overpass in 2017-03-20. 87

Figure 4.75: AOT of Himawari-8 before Landsat-8 overpass in 2017-05-23. 88

Figure 4.76: AOT of Landsat-8 in 2017-05-23. 88

Figure 4.77: AOT of Himawari-8 after Landsat-8 overpass in 2017-05-23. 88

Figure 4.78: The near horizontal AEC distribution at 349 nm for 30 minute rotation at the time of Landsat-8 satellite overpass and Himawari-8 satellite cover Kanto area. 91

Figure 4.79: The spatial distribution of AOT at 482 nm derived from the analysis of band-2 images of Landsat-8 OLI, at the time of satellite overpass around 10:15 JST on (a) 27 October 2016, (b) 31 January 2017, (c) 20 March 2017, and (d) 23 May 2017. 92

Figure 4.80: The spatial distribution of AOT at 455 nm derived from the analysis of band-1 images of Himawari-8, at the time of after overpass of Landsat-8 satellite around 10:20 JST on (a) 27 October 2016, (b) 31 January 2017, (c) 20 March 2017, and (d) 23 May 2017. The AOT distributions are seen similar to the band-2 of Landsat-8 observation with uncertainty around 1-5%. 93

Figure 4.81: The temporal and column AEC distributions at 532 nm for 4 hours at the time of Landsat-8 satellite overpass and Himawari-8 satellite cover Kanto area. 94

Figure 4.82: The spatial distribution of AOT at 562 nm derived from the analysis of band-3 images of Landsat-8 OLI, at the time of satellite overpass around 10:00 JST on (a) 27 October 2016, (b) 31 January 2017, (c) 20 March 2017, and (d) 23 May 2017. The highest AOT distribution is seen in (c) (τ_{482}= 0.45-0.50) while the smallest in (b) (τ_{482}=0.05 – 0.07). 95

Figure 4.83: The spatial distribution of AOT at 510 nm derived from the analysis of band-2 images of Himawari-8, at the time of satellite overpass around 10:00 JST on (a) 27 October 2016, (b) 31 January 2017, (c) 20 March 2017, and (d) 23 May 2017. The AOT distributions are seen similar to the band-3 of Landsat-8 observation with uncertainty around 1-5%. 96

Figure 5.1: The scheme of LED-DOAS which is developing at CEReS-Chiba University 101

LIST OF TABLES

Table 2.1: List of the band, central wavelength [nm], spatial resolution [m], and legend of each band. The list is modified from (http://landsat.usgs.gov/). 19

Table 2.2: List of the channel, central wavelength [nm], spatial resolution [km], and legend of each band. 21

Table 4.1: Atmospheric model and aerosol type as input parameter for MODTRAN computation for calculating radiative transfer of Landsat-8 and Himawari-8 images over the Kanto area. The τ_{550} refers to the value of AOT at 550 nm interpolated from sunphotometer and skyradiometer. 79

Table 4.2: The average of atmospheric condition at the space observation based on Himawari-8 before Landsat overpass (H8-BOP), Landsat overpass time (L8-OP), and Himawari-8 after overpass (H8-AOP). 89

Table 4.3: The average of corrected AEC, AOT, and AE with the time observations are H8-BOP (Himawari-8 before overpass), L8-OP (Landsat-8 overpass), H8-AOP (Himawari-8 after overpass). Both blue and green result from interpolation of sampling and optical measurements. 90

LIST OF SYMBOLS AND ABBREVIATION

α_{ext}	:	extinction coefficient
α_{sca}	:	scattering coefficient
β	:	backscattering
σ	:	cross-section
θ	:	scattering angle
τ	:	total optical thickness
ξ	:	longitude of target
η	:	latitude of target
γ	:	satellite field of view
Δ	:	depolarization factor
θ_γ	:	satellite zenith angle
ϕ_γ	:	satellite azimuth angle
ω_0	:	ratio between cross-section of scattering and extinction
τ_A	:	aerosol optical thickness
α_{abs}	:	absorption coefficient
σ_{abs}	:	cross-section of absorption
ρ_{al}	:	total albedo of Himawari-8
ρ_{ar}	:	apparent reflectance
ρ_{sr}	:	surface reflectance
σ_{ext}	:	cross-section of extinction
τ_G	:	gases optical thickness
σ_i	:	standard deviation
μ_i	:	mixing ratio of density number and total density of the particle
σ_R	:	Rayleigh cross-section
τ_R	:	molecule optical thickness
θ_s	:	solar zenith angle
A	:	surface area
ATN	:	variable of the filter attenuation
AU	:	astronomical unit
b	:	turbidity coefficient
BC	:	black carbon concentration
d	:	earth-sun distance
$d\sigma/d\Omega$	:	differential cross-section
DN	:	digital number
E	:	an average of irradiance at the top of the atmosphere
$f(\lambda)$	:	signifies the absorption coefficient
g_i	:	Spectral response function

$G(z)$	:	overlapping function
h	:	high of the Himawari-8 satellite (35800 km)
I_λ	:	solar intensity at the boundary layer
I_c	:	solar intensity recorded by sunphotometer
L		total radiance
L_g	:	radiance from surface
L_{gd}	:	radiances reflected from the surface directly
L_{gi}	:	radiances reflected from surface indirectly
L_{MAX}	:	maximum spectral radiance
L_{MIN}	:	minimum spectral radiance
L_{obs}	:	observed radiance
L_p	:	radiance from the top of the atmosphere
L_{pix}	:	total radiance represented in pixel values
L_{pm}	:	path of radiance due to multiple scattering
L_{ps}	:	path of radiance due to single scattering
$m_{0,i}$	:	refractive index of dry particle-i
m_i	:	refractive index
m_w	:	the refractive index of water
n_i	:	lognormal distribution
N_i	:	number of density
N_{tot}	:	total density of the particle
O	:	total gases (Ozone and Carbon dioxide)
P	:	air pressure
p	:	Ångström exponent
$P(z)$	:	lidar equation
P_0	:	standard of air pressure (1013.26 hP)
PSL	:	polystyrene latex
Q_{back}	:	backscattering efficiency
Q_{CALMAX}	:	maximum pixel values
Q_{CALMIN}	:	minimum pixel values
Q_{ext}	:	extinction efficiency
r	:	aerosol particle radius
R	:	the radius of the earth (6371 km)
$r_{0,i}$	:	average radius in wet condition
$r_{m,i}$	:	average radius in dry condition
S_λ	:	solar intensity at the top of the atmosphere
S_1	:	aerosol lidar ratio (extinction to backscattering ratio)
S_2	:	molecule lidar ratio
S_2	:	molecule lidar ratio
SG	:	specific attenuation cross-section
T	:	light transmission

T_0	:	sample spot
T_r	:	transmittance
V	:	element volume
$X(z)$	:	range corrected signal
z		signal range
λ	:	wavelength

6S	:	second simulation of a satellite signal in the solar spectrum
AEC	:	aerosol extinction coefficient
AOT	:	aerosol optical thickness
CEReS	:	center for environmental remote sensing
LOWTRAN	:	low resolution atmospheric radiance and transmittance
MODTRAN	:	moderate resolution atmospheric transmission
OLI	:	operational land imager
OPC	:	optical particle counter
PMT	:	photo multiplier detector
RH	:	relative humidity
RT		radiative transfer
TIRS	:	thermal infrared sensor

1. INTRODUCTION

1.1 Research Background

Atmospheric aerosols play an important role in the Earth's radiation budget through the reflection of incoming solar radiation and formation of cloud droplets working as cloud condensation nuclei. Therefore, the precise measurement of aerosol parameters is important for increasing the level of understanding their real characteristics, especially in the lower troposphere, for precise evaluation of their impact on environmental conditions. However, our knowledge on aerosol behavior is still insufficient for the accurate prediction of future climate [1,2].

The analysis of aerosol impact on climate is generally made by estimating aerosol radiative forcing within the atmosphere. There are various parameters relating to aerosol radiative effects such as aerosol optical thickness (AOT), single scattering albedo (SSA), asymmetry parameter, and aerosol extinction coefficient (AEC) [3]. For obtaining a better understanding of aerosols, what is needed is the monitoring technique that enables the retrieval of their optical properties [4,5]. Several previous studies used sunphotometers as ground-based instrument to analyze the aerosol information derived from the imagery of moderate resolution imaging spectroradiometer (MODIS) [6], Landsat-8 Operational Land Imager (OLI) [7], and Himawari-8 Advanced Himawari Imager (AHI) [8]. By means of lidar equipment and Fernald analysis, the spatial profile of AEC can be obtained by estimating some aerosol parameters as reported in references [9]–[11].

Since the atmospheric group of Center for Environmental Remote Sensing (CEReS), Chiba University has routinely monitored aerosol parameters using lidar systems, we propose the combined use of optical and sampling data from ground-based instrument (surface measurement) and the atmospheric data derived from the high-resolution satellite imagery (space measurement) for monitoring aerosol optical properties. The lidar systems consist of a multi-wavelength lidar system [14,15], a portable automated lidar (PAL) system [12], a system of atmospheric data collection lidar (ADCL) including a plan position indicator lidar (PPI) and a slant-path (SP) lidar [4,5,17]. Our group developed a monitoring technique based on the

data from several ground-based instruments during the overpass of Landsat 8 satellite or daytime observation of Himawari 8 satellite over the Kanto plain. The PPI and SP lidars can be utilized as the main instrument for studying aerosol profile that can be compared with the data from other ground sampling instruments. For this comparison, the Mie scattering calculation is carried out with the addition of relative humidity (RH) effect that represents aerosol growth/evaporation due to hygroscopic particles [14]–[16].

In this study, we describe the results of campaign measurements, in which the horizontal distribution of AEC is observed by means of the PPI lidar with the temporal information from the SP lidar, with ancillary data from other ground-based instruments during the overpass of Landsat-8 satellite over the Kanto area. Here we employ the Fernald method [9], which have been described in previous literatures [5], [10], [11], [13]. Since the elevation angles of these lidars are small (~4° for PPI and ~30° for SP), the major target of these instruments is the aerosol particles in the atmospheric boundary layer. Therefor, the far-end boundary values cannot usually be obtained for these lidars when applying the Klett [17] or Fernald analysis [9]. Instead, we propose the use of near-end boundary conditions that are available from the ground-based sampling instruments. In this procedure, we also consider the change of RH from the ambient (humid) to instrumental (dry) conditions [15]. Such an effect can be considered by introducing a factor of $f(RH)$, which is defined as the ratio between the aerosol scattering cross-section $\sigma(RH)$ and the corresponding cross-section under dry condition, $\sigma(RH_{dry})$ [16], [18].

The novel aspect of this study as compare with previous aerosol studies [19]–[21] is the use of the PPI lidar. Although our PPI lidar can monitor aerosol in the near surface layer by scanning 360^{o}, other instruments scan over limited sectors. Furthermore, through the present analysis, good consistency can be found between the spatial distribution of AEC from the PPI lidar and that of the AOT from the blue band of Landsat-8 and Himawari-8 satellite sensors [6]–[8], [22]. The additional aspect that is innovative in this study is the method for real-time observation of AOT by combining the sampling and optical measurements for both day- and nighttime [23], as compared with the previous study based on daytime data [24].

1.2 Research Purposes

The aims of this present research are the development of a new monitoring technique by observation of aerosol optical properties using a lidar system, ground-sampling instruments (nephelometer, aethalometer, and optical particle counter), sunphotometer, and satellites (Landsat-8 and Himawari-8). The specific purpose of this measurement method is the determination of several parameters listed below:

1. Temporal change of weather condition (relative humidity, temperature, air pressure, wind speed, and wind direction) which has a contribution to aerosol characteristics.
2. Temporal change of aerosol extinction coefficient in the boundary layer using ground sampling instruments (nephelometer and aethalometer).
3. Temporal change of lidar ratio (extinction to backscattering ratio) by fitting Mie scattering calculation and ground-sampling instruments (nephelometer, aethalometer, and optical particle counter) as an indispensable parameter in Fernald analysis.
4. Spatial and temporal distribution of aerosol extinction coefficient by analyzing PPI and SP lidar signals using Fernald analysis.
5. Temporal change of AOT based on sunphotometer data using Lambert-Beer law and Langley extrapolation methods, together with skyradiometer data.
6. Temporal change of Ångström exponent based on scattering of nephelometer and AOT of sunphotometer, coupled with that of a skyradiometer.
7. Apparent reflectance of Landsat-8 and Himawari-8 satellites.
8. Radiance using moderate resolution atmospheric transmission (MODTRAN) based on surface reflectance, AOT, solar zenith angle, solar azimuth angle, satellite zenith angle, and satellite azimuth angle.
9. Surface reflectance of both Landsat-8 and Himawari-8 satellites by establishing look-up table (LUT) based on apparent reflectance and AOT.
10. Spatial distribution of AOT derived from satellite sensors of Landsat-8 and Himawari-8.

1.3 Significance of Research

The significance of this research resides in obtaining detailed insight into the spatial and temporal distribution of near-surface aerosol, which also yields better constraint on the atmospheric correction of satellite remote sensing data. Besides, most of ambient parameters that are indispensable for understanding aerosol are retrieved directly from several instruments installed and routinely operated in CEReS, Chiba University. The additional innovation made in this study is the determinaiton of correction factors for sampling instruments using the concurrent data of optical measurements. The two main correction factors considered in this study are first, the truncation correction and second, the relative humidity correction, both of which are applied to convert the sammpling data of an integrating nephelometer to ambient values.

2. SCIENTIFIC BACKGROUND AND THEORY

In this research, a new monitoring technique is developed by concurrent measurement and observation using lidar systems and other ground-based instruments when the overpass time of Landsat-8 satellite and Himawari-8 observtion over the Kanto plan. The lidar systems consist of plan position indicator (PPI, 349 nm) and slant path (SP, 532 nm) lidars, in addition to the vertical observation lidars (532 and 1064 nm) operated on the campus of Chiba University by the National Institute for Environmental Studies (NIES). The data from sampling instruments, namely, an integrating nephelometer, an aethalometer, and particle counters are effectively utilized to characterize near surface aeorosl, with the help of the data from a sunphotometer and weather monitor. All these insrumens are operated routinely in CEReS-Chiba University. On the other hand, radiative transfer calculation is implemented on the image data of Landsat-8 and Himawari-8 satellites by utilizing the aerosol model directly derived from the ground observations mentioned above. Therefore, many concepts are coupled together to investigate and establish the data processing. This part consists of 11 sections that explain how the scientific and empirical concepts have been developed in the course of the data formulation and analysis.

2.1 Aerosol Optical Properties

A precise measurement of aerosol parameters is indispensable for better understanding of their real characteristics, especially in the lower troposphere. For analyzing their characteristics, various aerosol optical properties can be monitored using conventional methods of both passive and active remote sensing. The most fundamental parameters are the extinction coefficient and optical thickness [25]–[27], both of which have been discussed in the context of light attenuation due to the presence of aerosol particles.

When propagating in the atmosphere, the light intensity decreases because of the interaction with aerosol particles floating in the atmosphere. Attenuation of light intensity is generally described with a parameter known as the aerosol extinction coefficient (AEC), which is given as a linear summation of aerosol scattering and

absorption coeeficients [25]–[27]. The major scattering phenomenon in the atmosphere can be classified into two types, namely, Rayleigh scattering and Mie scattering. The Rayleigh scattering is the elastic interaction between light and molecules where the wavelength of light is much larger than the particle size. On the other hand, the theory of Mie scattering is employed to describe the light interaction with aerosols, which have diameters larger that or nearly equivalent to the light wavelength. The detection of back-scattering intensity is the main issue for the lidar measurement. Another phenomenon that leads to the attenuation of light in the atmosphere is absorption due to both molecules and aerosols. For the molecular part, the major absorbers near the visible range of the spectrum are ozone, water vapor and oxygen [28], though more minor species such as NO_2 and SO_2 are also important from the viewpoint of air-pollution studies. For the aerosol part, both scattering and absorption processes are considered simultaneously in the treatment based on the Mie scattering theory in the form of the complex refractive index. Generally the larger value of the imaginary part of the refractive index indicates the more significane of absorption, and hence, the lower values of the single scattering albedo [4], [10], [11].

The aerosol optical thickness (AOT) is defined as the integral of the AEC from ground to a reference height, which is often assumet to be the top of the atmosphere. More generally, however, AOT can be defined as the integration of AEC over the light propagation range under consideration [3], [4]. As a consequence, the basic form of the Lambert-Beer Law can be represented as a function of either AEC or AOT. When the value of AEC is homogeneous, AOT equals to the multiplication between the AEC and propagation range [29]–[31]. It is further noted that both of these parameters are given a function of wavelength.

2.2 Ground Based-Sampling Instruments

Ground-based sampling instruments employed in this monitoring technique are the three-wavelengths integrating nephelometer (TSI, Model 3563), the seven-wavelengths aethalometer (Magee Scientific, AE-31), and particle counters (Rion, KC-22B, KC-01D, KC-01E). These instruments can provide continuous information on scattering, absorption, and size distribution, respectively, of aerosol

particles sampled near the ground level. By means of sampling instrument, the value of AEC (α_{ext}) can be calculated using:

$$\alpha_{ext}^{S} = \alpha_{sca} + \alpha_{abs} \ , \tag{2-1}$$

where scattering coefficient (α_{sca}) is retrieved from the nephelometer and absorption coefficient (α_{abs}) from the aethalometer. Superscript *S* denotes that the value is derived from the sampling measurement.

The three-wavelength integrating nephelometer (TSI, Model 3563) installed and operated in CEReS is equipped with a backscatter shutter. The scheme of the nephelometer is showed in Figure 2.1. This instrument is operated by filtering small particle within the air sample inlet. During operation, a small turbine attached samples aerosol particles through the large diameter inlet port into the sensing volume. Then, the sample is illuminated by a halogen lamp over an angle 7 to 170 degrees. For measuring the scattering coefficient, the light scattered by the aerosol sample is split into three colors using dichroic filters placed in front of photo multiplier tube (PMT) detectors. The three wavelengths are blue (450 nm), green (550 nm), and red (700 nm).

On the other hand, the backscattering coefficients at the same wavelength are measured by blocking light over the range of 90 to 170 degrees. Simultaneously ancillary sensors of the nephelometer measure air pressure (hPa), temperature (K) both outside and inside, and relative humidity (%) inside the scattering volume. The maximum sensitivity of this instrument corresponds to the AEC value of 2.0×10^{-7} per meter (m^{-1}) at the longest averaging time of 30 s [5], [10], [32].

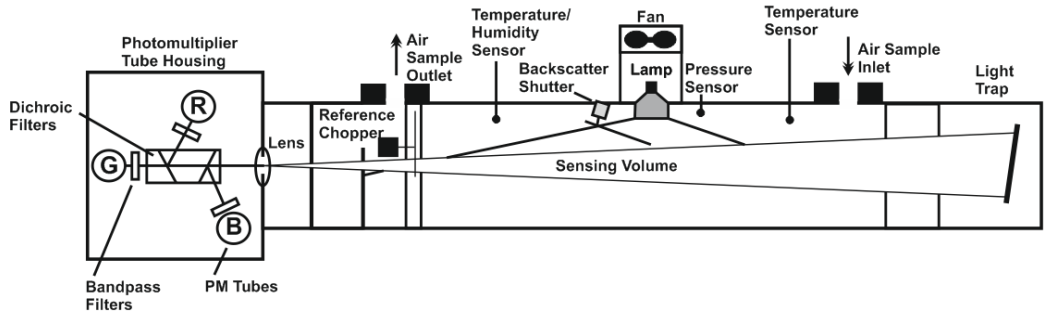

Figure 2.1: The scheme of three-wavelength integrating nephelometer (TSI, Model 3563) with backscatter photomultiplier tube housing, backscattering shutter, sensing volume, and additional sensors (temperature, humidity, and pressure). (http://www.tsi.com/integrating-nephelome-ter-3563/)

Figure 2.2 illustrates the essential scheme for developing the aethalometer algorithm that reports the black carbon (BC) concentration. The BC concentration is measured in nanogram per meter cubic (ng/m^3) by drawing air sample through the filter. The flow rate of the aerosol sample is monitored by an internal mass flow meter and is stabilized electronically for database report. For deriving the BC concentration, the filter attenuation through the sample spot is formulated as

$$ATN = -\ln\left[\frac{T}{T_0}\right], \tag{2-2}$$

where parameters T_0 and T are the light transmissions through the pristine portion of the filter and the sample spot on the filter. From time t to time t+dt, particles are collected on the filter spot from the column of aerosol-laden air sample, leading to the increase in the value of ATN. The BC concentration at wavelength λ can be calculated as

$$BC(\lambda) = -\frac{d(ATN(\lambda,t))}{dt}\,\frac{1}{SG(\lambda)}\,\frac{A}{V}. \tag{2-3}$$

Here, parameters A and V represent the sample spot area and the rate flow volume, respectively. According to the mannual of the manufacturer, SG in meter square per gram [m^2/g] is the specific attenuation cross-section of BC particle accumulated in the filter (which is later represented as [6834/λ], where λ is the wavelength in

nanometer [nm]). To develop an emphirical algorithm for converting BC (λ) measurements to aerosol light–absorption coefficient, the attenuation of light, $-d(ATN)/dt$, on the filter with the sample point, A/V, is assumed as absorption coefficient, (α_{abs}). Furthermore, the dimension are converted into nm. Consequently, the formula of absorption coefficient (α_{abs}) for every wavelength (λ) based on black carbon (BC) concentration measurement is given as

$$\alpha_{abs}(\lambda) = \left(BC(\lambda) \times 10^{-9}\right) \frac{6834}{\lambda}. \tag{2-4}$$

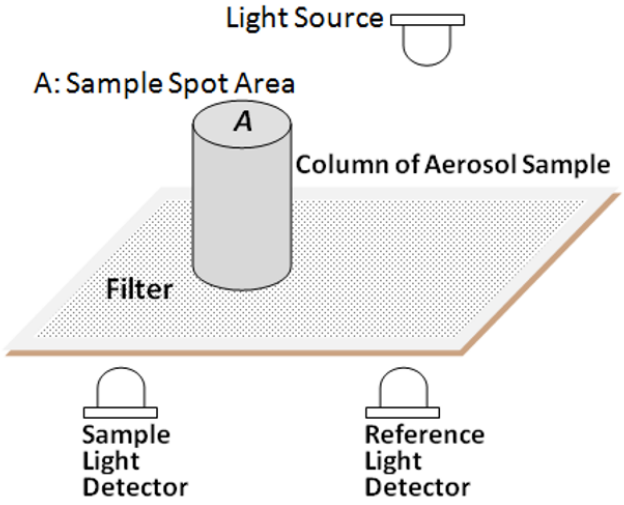

Figure 2.2: The scheme of an aethalometer algorithm in reporting BC concentration, completed by sample spot area, a column of the aerosol sample, filter, light source, sample light detector, and reference light detector.

The AE-31 aethalometer (Magee Scientific) is routinely operated in CEReS to acquire data in seven channels at wavelengths ranging from the ultraviolet to near-infrared, namely 370, 450, 571, 615, 660, 880 and 950 nm. The time interval of BC concentration recording is 5 minutes [33], [34].

The optical particle counter (OPC) is an instrument that measures particles floating in gases and liquid phases using the technique of light scattering. Figure 2.3 explains the principle of OPC (Rion, KC-22B, KC-01D, KC-01E) in reporting aerosol size distribution based on sample particulate. The entire aerosol sample with 300 mL/min of flow rate, the particle detection block, is optically adjusted by transparent quartz material with polystyrene latex (PSL) particles (refractive index

1.6) in clean air. Furthermore, the laser beam generated by laser-diode-pumped Nd:YVO_4 with wavelength 1064 nm (rated output power 1 W, wavelength 800 nm) irradiate the aerosol sample. As a result, Rayleigh (Mie) scattering occurs for particles with sizes smaller (larger) than the irradiated wavelength. Moreover, the light intensity scattered at 90-degree sideway is focused by aspherical lenses (condensing half-angle 40 degrees) to a photodiode detector. Finally, the size of the particle is recorded based on detector sensitivity in sensing the signal of light scattered. Detectable range of OPC (Rion KC-22B) installed in CEReS is divided into five channel i.e: 0.08, 0.1, 0.2, 0.3, and 0.5 μm. It can record concentration of particle number in count per liter (count/L) for every 2 minutes and 10 seconds (02:10) [4], [10], [11], [13].

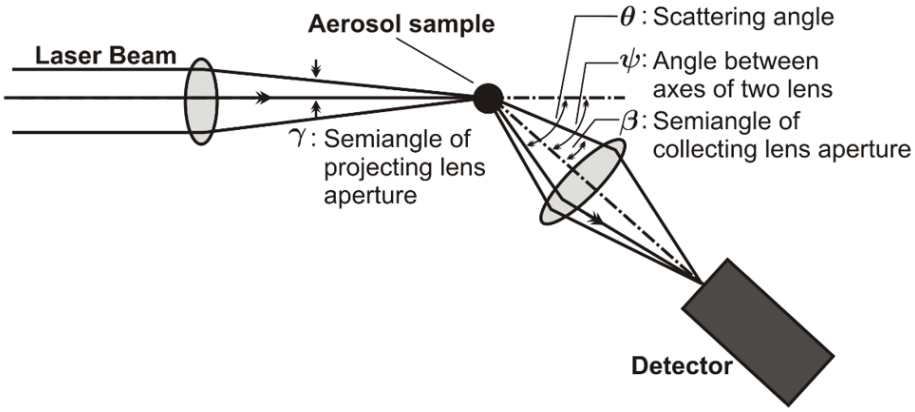

Figure 2.3: Block diagram of OPC in detecting aerosol size distribution. The OPC completed by laser beam, lens, and detector. (http://www.rion.co.jp)

2.3 Lidar Ratio Calculation

Lidar ratio, the ratio between the extinction coeffcieint (α) and backscattering coefficient (β), is an indispensable parameter for retrieving AEC distribution using the Fernald method. The value of lidar ratio depends on not only the wavelength of the scattered light but also aerosol characteristics (structure, size, and composition) [28]. The other factor that can affect lidar ratio is relative humidity through the process of growth/evaporation of hygroscopic particles [35]. Consequently, it is desirable to determine lidar ratio in accordance with the actual condition of the

atmosphere [34]. The calculation of lidar ratio is based on the Mie theory, and can be formulated as follows.

The numerical computation is based on the assumption that aerosol is an external mixture of the external component. The number size distribution (n_i) of i-th aerosol component is given as a function of aerosol particle radius (r) as

$$n_i(r) = \frac{N_{tot}\,\mu_i}{\sqrt{2\pi}\,\ln\sigma_i\,r}\,\exp\left[-\frac{\ln^2(r/r_{m,i})}{2\ln^2\sigma_i}\right]. \tag{2-5}$$

Here, parameters $r_{m,i}$, and σ_i stand for the average radius and standard deviation of the lognormal distribution, respectively. In the numerator, the term $N_{tot}\,\mu_i$ is the number density of the i-th component expressed by using the mixing ratio μ_i between the number of density and total density of particle ($\mu_i=N_i/N_{tot}$). Under the influence of relative humidity, the refractive index (m_i) can be expressed as

$$m_i = m_w + (m_{0,i} - m_w)\left(\frac{r_{0,i}}{r_{m,i}}\right)^3, \tag{2-6}$$

where m_w is the refractive index of water (=1.33-0i) and $m_{0,i}$ is the refractive index of dry particle-i. The median values of volume-weighted average of the particle radius under dry and wet conditions are written as $r_{0,i}$ and $r_{m,i}$, respectively. Moreover, by employing Mie theory to calculate both the extinction (Q_{ext}) and backscattering (Q_{back}) efficiencies, we can write the lidar ratio, $S_1=\alpha/\beta$, as

$$S_1 = \frac{\sum_{i=1}^{M}\int_0^{\infty} Q_{ext}(r,m_i,\lambda)\,\pi\,r^2 n_i(r)dr}{\sum_{i=1}^{M}\int_0^{\infty} Q_{back}(r,m_i,\lambda)\,\pi\,r^2 n_i(r)dr}. \tag{2-7}$$

Equation (2-7) is used to evaluate how the value of S_1 changes according to the variations in wavelength (λ), particle radius (r), and refractive index (m_i).

On the other hand, by involving ground sampling instruments, lidar ratio can be calculated with the same principle but different approach. Since scattering is the linear difference between extinction and absorption, in the case of existing

absorption, cross-section of both extinction (σ_{ext}) and absorption (σ_{abs}) is determined using:

$$\sigma_{sca} = \frac{2\pi}{k^2} \sum_{l=1}^{\infty}(2l+1) \ [|a_l|^2 + |b_l|^2] \tag{2-8}$$

$$\sigma_{abs} = \frac{4\pi}{k^2} \sum_{l=1}^{\infty}\left(2l+\frac{1}{2}\right) \mathrm{Re} \ [|a_l|^2 + |b_l|^2] \tag{2-9}$$

Here, notation "Re" and "Im" express real and imaginary part of the complex number, respectively, as explained in Appendix A1 (Scattering Theory). In the case of non-negligible absorption, the scattering parameter is derived from the single-scattering albedo, which is defined by the ratio between scattering and extinction ($\omega_0 = \sigma_{sca} / \sigma_{ext}$). When the incident light interacts with the aerosol particle, the angular distribution of scattered energy is described by the phase function. If we denote the scattering angle as θ, the phase function, $f(\cos\theta)$ is defined as the ratio between the differential cross-section $(d\sigma/d\Omega)_\theta$ and total scattering cross-section (σ_{sca}):

$$f(\cos\theta) = \frac{1}{\sigma_{sca}} \left(\frac{d\sigma}{d\Omega}\right)_\theta . \tag{2-10}$$

Since the extinction coefficient is given by $\alpha_{ext} = n\sigma_{ext} = n\sigma_{sca} / \omega_0$ and the back-scattering coefficient is given by $\beta = n(d\sigma/d\Omega)_{\theta=\pi}$, we obtain

$$S_1 = \frac{\sigma_{ext}}{\left(\frac{d\sigma}{d\Omega}\right)_{\theta=\pi}} = \frac{1}{\omega_0 f(\cos\pi)} . \tag{2-11}$$

This procedure needs the data from a nephelometer, an aethalometer, and an optical particle counter for implementing the calculation of lidar ratio [4], [10], [11].

2.4 Lidar Measurement and Fernald Method

Among various techniques of optical remote sensing, the advantage of lidar (Light Detection and Ranging) measurement is the capability of both temporal and spatial monitoring of aerosol particles in the atmosphere. The signals back-scattered by aerosol particles located at different heights are detected by the lidar receiver

system. The strength of the signal is affected also by the attenuation in the light propagation path due to scattering and absorption processes. Generally, a Mie-scattering lidar system consists of the transmitter and reciever sub-systems. The transmitter is usually a pulsed laser coupled to a beam expander, while the receiver sub-system consits of a telescope equipped with a narrow band-pass filter, a photomultiplier tube (PMT), a transient recorder, and a PC. A schematic illustration of lidar measurement is shown in Figure 2.4.

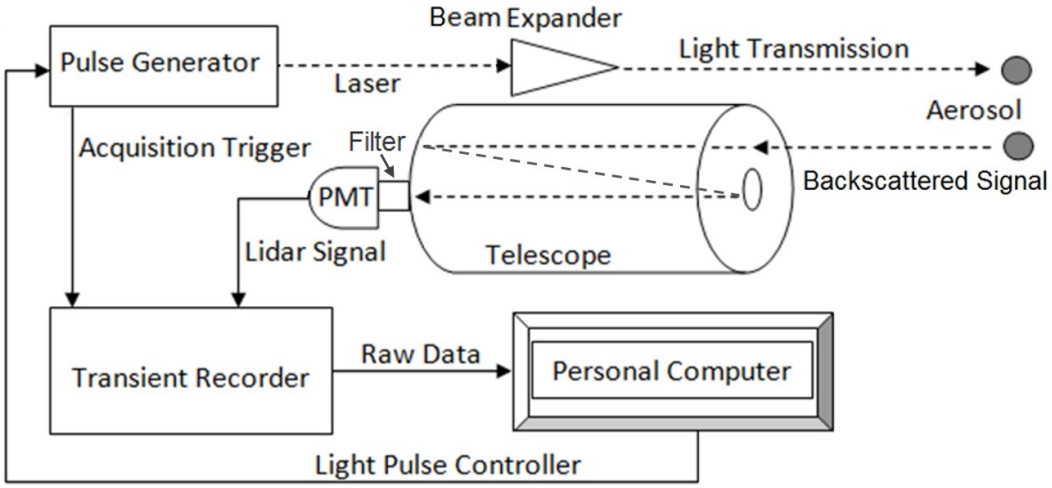

Figure 2.4: A principle of lidar measurement. The pulse from the generator is transmitted by laser expander. The inverted signal scattered by atmospheric aerosol is detected by telescope, then collected in the transient recorder. A personal computer controls the system.

Fernald method is a procedure develoed for processing lidar signal to determine the extinction coefficient. After the background correction, the raw lidar signal is converrted to the range corrected signal, and subsequently, the inversion of this range corrected signal is carried out to retrieve the backscattering coefficient. Conventionally, the lidar signal processing using the Fernald method is carried out by solving lidar equation

$$P(z) = A\,\frac{G(z)}{z^2}\left(\beta_1(z) + \beta_2(z)\right)\exp\left[-2\int_0^z \alpha_1(z')dz' - 2\int_0^z \alpha_2(z')dz'\right], \quad (2\text{-}12)$$

where A and G represent the system constant and overlapping function, respectively. Both extinction coefficient (α) and backscattering (β) coefficent are

determined as a function of signal range (z) for aerosol (α_1 and β_1) and air molecule (α_2 and β_2).

For solving the lidar equation, the first step is assuming a relationship between the extinction and backscattering coeeficients:

$$\alpha_1(z) = S_1(z)\beta_1(z) \tag{2-13}$$

$$\alpha_2(z) = S_2(z)\beta_2(z) \tag{2-14}$$

Here $S_1(z)$ and $S_2(z)$ are the lidar ratio for aerosol and air molecule. Since aerosol loading is up to around 2 km near the ground level and the molecular composition is stable below 80 km, aerosol lidar ratio (S_1) is represented as a function of altitude while molecule lidar ratio (S_2) is a constant. Another assumption needed for solving equation (2-12) is the range corrected signal as:

$$X(z) = \frac{P(z)\, z^2}{G(z)} \tag{2-15}$$

By adjusting several conditions, wherein the actual analysis $G(z)$ is unity and S_1 is a constant, distribution of aerosol extinction coefficient is analytically derived from the equation:

$$\alpha_1(z) = -\frac{S_1(z)}{S_2}\,\alpha_2(z) + \frac{S_1(z)\,X(z)\exp[I(z)]}{\frac{X(z_c)}{\frac{\alpha_1(z_c)}{S_1(z_c)}+\frac{\alpha_2(z)}{S_2}}+J(z)} \tag{2-16}$$

Here $S_1(z)$ means a constant which is obtained from Mie theory calculation and S_2 value is 8.52 sr which is derived from Rayleigh scattering principle. The function of $I(z)$ is defined as:

$$I(z) = 2\int_z^{z_c}\left[\frac{S_1(z')}{S_2} - 1\right]\alpha_2(z')dz' \tag{2-17}$$

while $J(z)$ is:

$$J(z) = \int_z^{z_c} S_1(z')X(z')\exp[I(z')]\,dz \tag{2-18}$$

Here, z_c is an expression of minimum altitude at which a far-end boundary coefficient is assumed as $\alpha_1(z_c)$. In the clear sky condition, the value of $\alpha_1(z_c)$ is often assumed as same as 0 (zero) as a consequence of free aerosol loading [4], [9], [17]. The complete description of the Fernald method is formulated in Appendix B (Fernald Method).

2.5 Aerosol Optical Thickness and Sunphotometer

Aerosol optical thickness (AOT) measured using a sunphotometer is a parameter that describes the attenuation of solar radiation from the top of the atmosphere to the ground level [3]. Besides, the AOT is an important parameter for atmospheric correction of satellite remote sensing imagery in relation to visibility degradation due to air pollution [36]. Bisides, better understanding of the spectral dependence of AOT is significant for analyzing the effect of aerosols on the earth radiation budget. The wavelength variation in AOT is also important for obtaining aerosol parameters from satellite remote sensing because of their difference due to the changes in physical and chemical characteristics [37].

The AOT parameter in this research is derived from the sunphotometer (Prede PSF-100) data processing which is employed to estimate the solar intensity as illustrated in Figure 2.5. Before raching the ground, the solar radiation is attenuated by scattering due to air molecule and aerosol, and also by absorption due to gases such as ozone, oxygen, and water vapor [38], [39]. Derivation of AOT can be carried out by employing Langley plot and Lambert-Beer law [3], [29], [31].

Langley plot is utilized for calibrating the sunphotometer under a condition of minimal (and stable) aerosol loading. The basic equation can be written as

$$\ln(I_\lambda) = -\frac{\tau_\lambda}{\mu} + \ln(S_\lambda). \tag{2-19}$$

Here, I_λ and S_λ are solar intensity for every wavelength (λ) at far-end boundary layer (derived from sunphotometer in the clearest condition) and at the top of atmosphere (TOA), respectively. The Langley plot is carried out by defining $x = 1/\mu = \sec \theta_s$, where θ_s is the solar zenith angle. Then, a linear equation in the form $y = mx + c$ is constructed from $y = \ln (I_\lambda)$, with the slope of linear line of $m = -\tau_\lambda$

(total optical thickness), and with the *y*-intercept of $c = \ln(S_\lambda)$. To determine τ_λ and S_λ parameters, both *x* and *y* data are plotted by using a procedure which is shown in Figure 2.6.

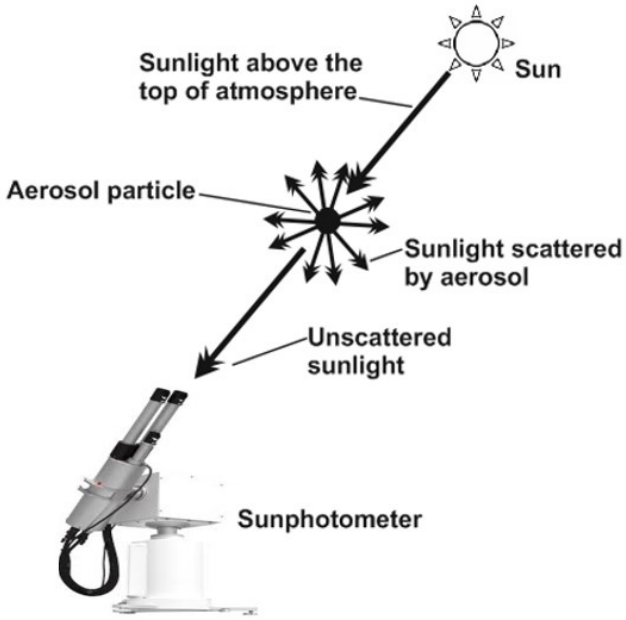

Figure 2.5: A principle of sunphotometer in measuring solar intensity.

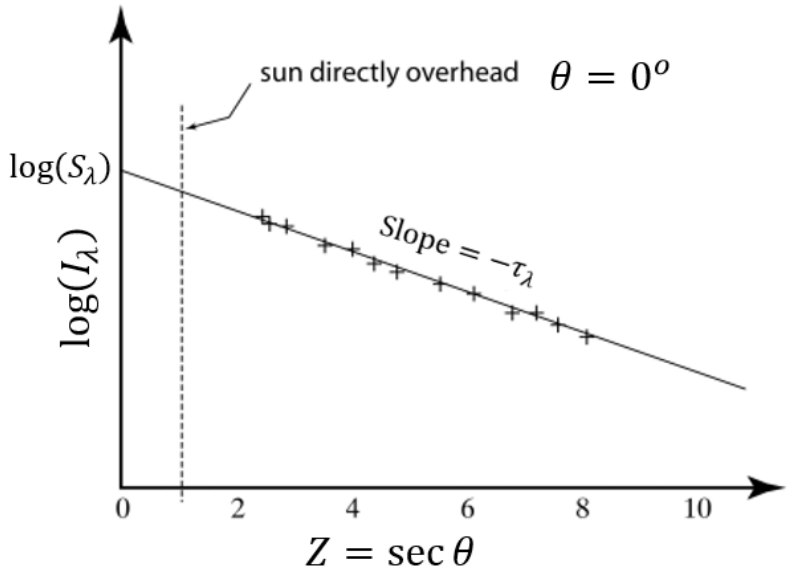

Figure 2.6: Langley plot principle to determine solar intensity at TOA.

In accordance with the Lambert-Beer law and Langley extrapolation methods [3], [31], [40], and considering some data records from the sunphotometer and other supporting data, an equation for calculating AOT can be written as

$$\tau_A(\lambda) = \tau(\lambda) - \tau_G(\lambda) - \tau_R(\lambda). \quad (2\text{-}20)$$

Here the index *A*, *G*, and *R* refer to the AOT of aerosol, the optical thickness of absorbing gases and air molecules (Rayleigh scattering), respectively. In this calculation we derive $\tau(\lambda)$ using the formula of

$$\tau(\lambda) = \frac{\ln I_c(\lambda) - 2\ln R - \ln I(\lambda)}{m(\theta)}. \quad (2\text{-}21)$$

Here, I_c is the solar radiation intensity equal to 1 AU (astronomical unit), I is the solar radiation intensity measured by sun photometer, R is the distance from the Earth to the Sun, and m is the air mass based on the solar zenith angle (θ). The solar radiation intensity at the top of the atmosphere (I_c) is determined using the Langley extrapolation method by linearization of Beer's Law equation [31], [40]. The values of optical thickness of both absorbing gases and molecule in equation (2-20) are calculated as

$$\tau_G(\lambda) = O \times 10^{-3} \times f(\lambda), \quad (2\text{-}22)$$

$$\tau_R(\lambda) = \frac{P}{P_0} \times 0.00000864 \times \lambda^{-(3.916+0.000074\,\lambda+\frac{50}{\lambda})}. \quad (2\text{-}23)$$

In equation (2-22), parameters *O* represents the average of ozone and water vapor in the observation point which can be taken from the website: http:// lap.physics.auth.gr/ozonnemaps2/ and $f(\lambda)$ indicates the absorption coefficient at each wavelength which can be accessed from the JMA website: http://www.jma-net.go.jp/kousou/obs-third-diu/. The ozone concentration is represented in Dobson Unit (DU), where 1 DU is equivalent to a 0.01 mm thick layer of pure ozone at standard temperature and pressure. Furthermore, P and P_0 in equation (2-23) denote the air pressure and standard of air pressure (1013.26 hP), respectively which can

be seen in sunphotometer system data at the same time of the solar radiation intensity.

2.6 Ångström Exponent

The light spectrum traversed in the atmosphere is affected by the particle size distribution which is qualitatively indicated by Ångström exponent. Many studies of AOT rely on the Ångström exponent (p) to quantify the spectral dependence. An empirical expression was written by Angtrom (1972) in a simple equation [41]. The value of Ångström exponent, p, can be calculated from the spectral values of either aerosol extinction coefficient (α) or AOT (τ). In the case of AOT, we have

$$\tau(\lambda) = \tau(\lambda_0)\left(\frac{\lambda}{\lambda_0}\right)^{-p} = b(\lambda)\,\lambda^{-p}\,. \tag{2-24}$$

Here the turbidity coefficient (b) is defined as

$$b(\lambda) = \tau(\lambda_0)\,\lambda_0^{-p}\,. \tag{2-25}$$

The typical value of p is around 1. When the aerosol distribution is dominated with fine mode particles, a higher value such as p~1.5 is observed. On the contrary, when the coarse mode particles dominate, we have a smaller value such as p~0.5.

2.7 Landsat-8 Satellite

Landsat-8 satellite, the eighth generation of Landsat programs, has a high spatial resolution of 15/30/100 meters (panchromatic/multispectral/thermal) but long overpass period of 16 days. Launched on February 11, 2013, and operated on May 30, 2013, Landsat-8 has 11 bands: the operational land imager (OLI) for bands 1-9 and thermal infrared sensor (TIRS) for band 10-11. It floats on the high level of 705 km and has 170 km × 183 km of scan area [7], [42], [43]. The channels and wavelength of the Landsat-8 satellite are listed in Table 2.1.

Table 2.1: List of the band, central wavelength [nm], spatial resolution [m], and legend of each band. The list is modified from (http://landsat.usgs.gov/).

Band	Central Wavelength [nm]	Spatial Resolution [m]	Legend
1	435 - 451	30	Coastal / Aerosol
2	452 - 512	30	Blue
3	533 - 590	30	Green
4	636 - 673	30	Red
5	851 - 879	30	NIR
6	1,566 - 1,651	30	SWIR-1
7	2,107 - 2,294	30	SWIR-2
8	503 - 676	15	Panchromatic
9	1,363 - 1,384	30	Cirrus
10	10,600 - 11,190	100	TIR-1
11	11,500 - 12,510	100	TIR-2

The significant parameters related to image data of satellite are a pixel value in digital number (*DN*), radiance (w/m^2 Sr μm), and apparent reflectance (dimensionless). Every satellite has their empiric equation in calculating radiance (L) and apparent reflectance (ρ_{ap}) as a function of wavelength (λ). Equations (2.26) and (2.27) are apparent reflectance and radiance of Landsat-8, respectively,

$$\rho_{ap}(\lambda) = \frac{\pi\ d^2}{E(\lambda)\cos\theta_s} \times L_{obs}(\lambda) \tag{2-26}$$

$$L_{obs}(\lambda) = \frac{L_{MAX} - L_{MIN}}{Q_{CALMAX} - Q_{CALMIN}} \times (DN - Q_{CALMIN}) + L_{MIN} \tag{2-27}$$

In equation (2-26), parameters d, E, and θ_s are earth-sun distance in astronomical unit (AU), average of irradiance at the top of atmosphere, and solar zenith angle, while in equation (2-27) parameters L_{MAX} and L_{MIN} are spectral radiance scaled to pixel values, Q_{CALMAX} and Q_{CALMIN}, respectively [7].

To determine surface reflectance of Landsat-8 satellite, separation of atmospheric and land reflectance is estimated by means of solar zenith and azimuth angles, together with satellite zenith and azimuth angles to the target. For the Landsat-8 satellite, information for calculating surface reflectance is provided in its metadata.

2.8 Himawari-8 Satellite

Himawari-8 satellite, the world's first third-generation geostationary meteorological satellite, has a low spatial resolution of 500-2000 meter but the high temporal resolution of 2.5 minutes for Japan area. Himawari 8 was launched on October 7, 2014, and then it has been operating since July 7, 2015. It has 16 bands, visible (VIS) of bands 1-3, near infrared (NIR) of band 4-5, and infrared (IR) bands 7-16. The IR bands are classified to IR-4 (bands 7-8), IR-3 (bands 8-12), IR-1 (bands 13-14), and IR-2 (bands 15-16). As a geostationary satellite, the Himawari 8 records surface and atmosphere of earth at approximation 35.800 kilometer high above the equator at around 140^{o}E. By carrying an Advanced Himawari Imager (AHI) sensor, the satellite has the capability in scanning five areas: Full Disk (images of the whole area as seen from the satellite), the Japan Area (regions 1 and 2), the target area (region 3) and two landmark areas (regions 4 and 5)[44]–[46]. The scheme of Himawari-8's observation area and frequencies are presented in Figure 2.8. The Himawari-8' channels are listed in Table 2.2.

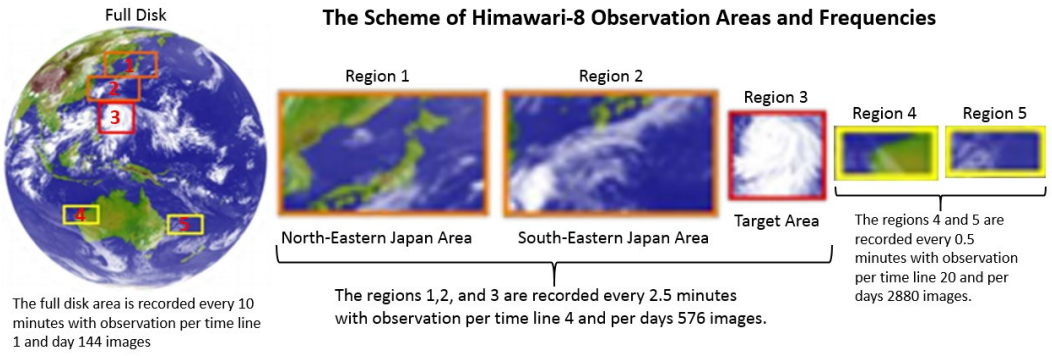

Figure 2.7: Himawari-8 observation area and frequencies. The full disk is recorded every 10 minutes, three regions (1,2,3) are collected every 2.5 minute, and two others regions (5 and 6) are covered every 0.5 minutes.

Table 2.2: List of the channel, central wavelength [nm], spatial resolution [km], and legend of each band.

Channel	Central Wavelength [nm]	Spatial Resolution [km]	Legend
1	430 - 480	1	Blue
2	500 - 520	1	Green
3	630 - 660	0.5	Red
4	850 - 870	2	---
5	1,600 - 1,620	2	---
6	2,250 - 2,270	2	---
7	3,740 - 3,960	2	---
8	6,060 - 6,043	2	Water Vapor
9	6,890 - 7.010	2	Water Vapor
10	7,260 - 7,430	2	Water Vapor
11	8,440 - 8,760	2	SO_2
12	9,540 - 9,720	2	O_3
13	10,300 - 10,600	2	Atmospheric Window
14	11,100 - 11,300	2	Atmospheric Window
15	12,200 - 12,500	2	Atmospheric Window
16	13,200 - 13,400	2	CO_2

The Himawari-8 apparent reflectance calculation, different from the Landsat-8 satellite. The apparent reflectance (ρ_{ap}) of the Himawari-8 satellite is estimated using equation (2-28) based on the total albedo (ρ_{tot}) in equation (2-29), the average distance from the earth to the sun (d), and solar azimuth angle (θ_s). The total albedo is computed from observed radiance (L_{obs}) by means of the pixel value (DN) of the Himawari-8 satellite. Below are the formula of the Himawari-8:

$$\rho_{ap}(\lambda) = \rho_{tot}(\lambda)\frac{d^2}{\cos\theta_s} \tag{2-28}$$

$$\rho_{tot}(\lambda) = 0.001559 \times L_{obs}(\lambda) \tag{2-29}$$

$$L_{obs}(\lambda) = (0.377358 \times DN(\lambda)) - 7.547167 \tag{2-30}$$

Equations (2-28), (2-29), and (2-30) consist of several constant determined empirically for Himawari-8 satellite [44], [45].

The surface reflectance of the Himawari-8 satellite is estimated by separating the contribution of reflectance from atmosphere and surface. The separation process is carried out solar zenith and azimuth angles, accompanied by satellite zenith and

azimuth angles. For the Himawari-8, satellite zenith (θ_γ) and azimuth (ϕ_γ) angle are estimated using formulas, respectively:

$$\theta_\gamma = \tan^{-1}\left[\frac{(R+h)\sin\gamma}{(R+h)\cos(\gamma-R)}\right] \tag{2-31}$$

$$\phi_\gamma = 180^o - \sin^{-1}\left[\frac{\sin(\xi-\eta)}{\sin\gamma}\right]. \tag{2-32}$$

Where R, h, ξ, and η are the radius of the earth (6371 km), high of the Himawari-8 satellite (35800 km), longitude of tathe rget, and latitude of the target. The γ - parameter is the satellite field of view which is calculated using:

$$\gamma = \cos^{-1}[\cos\eta\cos(\xi_{sat}-\xi)]. \tag{2-33}$$

2.9 Radiative Transfer Calculation

The features collected by satellite sensors are exerted by both the ground reflectance and atmospheric conditions where the scheme is presented in Figure 2.8. The value of ground reflectance is affected by a land surface condition such as vegetation, soil, and sea surface. Besides, scattering and absorption of air molecules and aerosol particles have a vital contribution to image quality recorded by a satellite sensor. Therefore, the atmospheric correction process is necessary to retrieve the valid information from satellite image named the radiative transfer (RT) calculation of satellite scene. By formulating transmittance of the solar radiation, Chandrasekhar has developed the RT equation where the scattering and absorption process due to air molecule were considered [47], [48][47]. The RT parameter including various atmospheric and observational conditions has been provided in codes Low Resolution Atmospheric Radiance and Transmittance (LOWTRAN) [49], Moderate Resolution Atmospheric Transmission (MODTRAN) [50] and Second Simulation of a Satellite Signal in the Solar Spectrum (6S) [51]. Since the codes has been improved and applied in modeling RT of satellite signal processing in reference [4], [51]–[57] for the satellite, in this study, we apply the code for both Landsat-8 and Himawari-8.

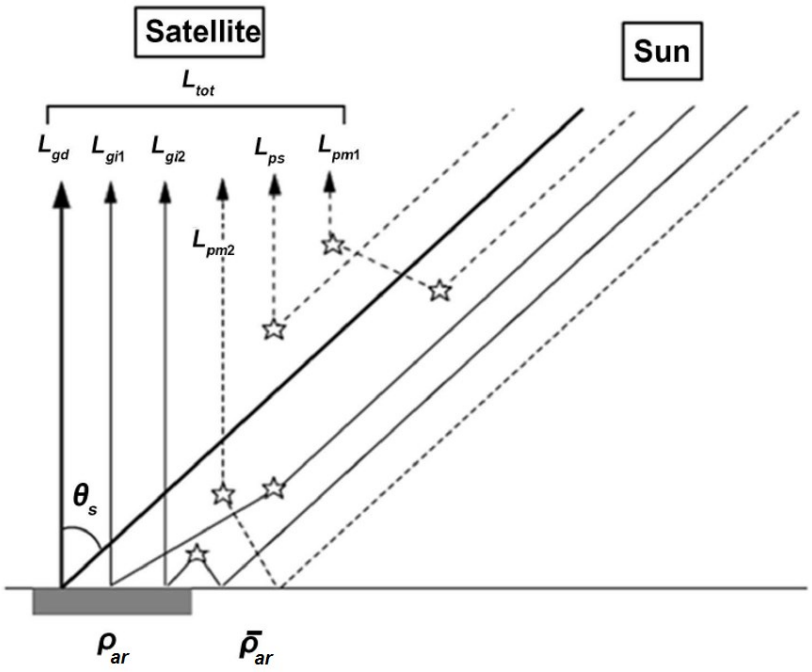

Figure 2.8: The scheme of RT formulation by Chandrasekhar which was taken. The scheme consists of six-components including surface reflectance and scattering in the atmosphere to compute the RT using MODTRAN.

The RT code of MODTRAN is developed by the Air Force Research Laboratory in collaboration with Spectral Science-Incorporated. As a passive and optics remote sensing case, the basic equation of RT is formulated by assuming that the irradiance from the sun detected by satellite sensor in radiance information after reflected by atmosphere and surface both directly and indirectly. The total radiance represented in pixel values which are observed by sensor satellite (L_{pix}) is separated in six-components as a function of reflectance and average reflectance. The concept is written in the form:

$$L_{pix} = L_{gd}(\rho_{ar}) + L_{gi_1}(\rho_{ar}) + L_{gi_2}(\rho_{ar}, \overline{\rho_{ar}}) + L_{ps} + L_{pm_1} + L_{pm_2} \quad (2\text{-}34)$$

Here, L_{gd} and L_{gi} are the radiances reflected from the surface directly and indirectly while L_{ps} and L_{pm} are the paths of radiance due to single and multiple scatterings, respectively. Formulation of both radiance from the surface (L_g) and top of atmosphere (L_p) are:

$$L_g = \frac{1}{\pi}\,\rho_{ar}(\lambda)\,E(\lambda)\cos\theta_s\,T_r(\lambda,\theta_s) \tag{2-35}$$

$$L_p = \frac{1}{\pi}\,\rho_{ar}(\lambda)\,E(\lambda)\cos\theta_s\,T_r(\lambda,\theta_s)\,T_r(\lambda,0) \tag{2-36}$$

The differences from equations (9) and (10) are transmittance process. In equation (9) as a representation of the surface, reflectance considers only transmittance (T_r) of solar irradiance (E) and equation (10) as an illustration of atmospheric scattering involve both transmittance from solar irradiance with solar zenith angle (θs) and radiance from surface reflectance [50]. Apparent reflectance (ρ_{ap}) obtained from image data is different from every satellite. Detail formulation and modification of the RT equation including the target reflectance (ρ_{ap}), average reflectance ($\overline{\rho_{ap}}$), the transmittance (T_r), and some parameters can be seen in satellite guide and in references [55]. The significant parameters related to imagery data of satellite are a pixel value in digital number (DN), radiance (W/m2 Sr μm), and apparent reflectance (dimensionless). Every satellites have their own empiric equation in calculating radiance (L) and apparent reflectance (ρ_{ap}) as a function of wavelength (λ). Apparent reflectance is calculated using the procedure in references [7], [42], [43] for Landsat-8 and procedure in references [44]–[46] for Himawari-8 satellites. The complete formulation of radiance and transmittance are presented in Appendix C (Radiance and Transmittance).

2.10 Atmospheric Parameters and Weather Detector

Weather, the state of the the atmosphere, occur in the near ground level [58]. Several weather elements are involved in computing and analyzing of aerosol parameters. The old studies about refractive index and Rayleigh scattering for correcting atmospheric optics measurements were employed temperature and air pressure [59]. Furthermore, in aerosol optical thickness calculation, Rayleigh scattering of air molecule was explicitly used air pressure [30], [60]. In CERes, both temperature and relative humidity are employed in aerosol mass concentration analysis [15]. Then, several temporal changes of weather conditions (temperature, relative humidity, wind direction, and wind speed) are involved as supporting data for analyzing the CO_2 measurement in the urban atmosphere [61].

2.11 Correction and Fitting

The correction factor employed in this study is the truncation error and the enhancement factor of the aerosol particle. The truncation correction is applied for estimating the loss of signal intensity due to relatively coarse particles. The other correction is for converting instruments to ambient values due to a reduction of aerosol particle diameter [62]. Below are explanation about the two corrections.

The truncation correction is intended for two main factor. The first factor is aerodynamic loss during the sampling procedure, and the second one is due to the limited range of the acceptance angle (between 7^o and 170^o) of the scattering measurement of the nephelometer (TSI3563). Comparison between extinction coefficient at 550 nm of sampling measurement (using nephelometer and aethalometer) and optical measurement using visibilitymeter is a compatible procedure in obtaining a truncation magnitude of truncation correction. The extinction coefficient of sampling observation is estimated using equation (2-1), by employing the equation formulated by Köschmeider where the considered attenuation ratio is approximately 5% [59]. The Köschmeider equation used in this correction is combination of the wavelength and substraction the Rayleigh contribution. The main purpose of the procedure is for obtaining a formula to retrive extinction coefficient of optical measurement (superscript *O*):

$$\alpha_{ext}^{O}(\lambda) = \frac{K_a}{V}\left(\frac{\lambda}{550}\right)^{-q} - \frac{PT_0}{P_0T}(1.095 \times 10^{-5})\left(\frac{\lambda}{550}\right)^{-4.05}. \quad (2\text{-}37)$$

Here, the wavelength, λ is represented in nanometer. The K_a=ln(1/0.05)=2.996 is the Köschmieder coefficient [63]. The visibility data, V, is retrieved from the visibilitymeter installed in CEReS hiba Universitry. The contribution of molecule as Rayleigh scattering is corrected by using the approximation which is formulated by Dutton et al. in reference [30]. The Rayleigh correction in equation (2-37) involve the pressure (P) and temperature (T). Both parameter are compared with their standard values (P_0=1013.25 hPa and T_0 = 288.15 K). This approximation has been implemented under relatively dry condition where the ambient RH below ~50% [23].

The aerosol growth process with the change of RH is an additional correction in the case of the ambient RH more than ~50%. Here, we assume that the aerosol particle with a higher diameter in the higher RH is reduced rapidly due to the scattering volume of TSI 3563, where it kept relatively warm and dry to avoid the potentially harmful deformation inside the instrument. Thus, to correct the measured value of the scattering coefficient from sampling measurement (indexed by *S*) into the near real value retrieved from optical measurement, we employ the *f*(*RH*) correction factor below:

$$f(RH,\lambda) = \frac{\sigma(RH,\lambda)}{\sigma(RH_{dry},\lambda)}. \tag{2-38}$$

Both $\sigma(RH,\lambda)$ and $\sigma(RH_{dry},\lambda)$ are representation of the aerosol scattering cross-section at the wavelength λ under ambient and inside instrument, respectively [37]. The dependence of $f(RH,\lambda)$ on RH has been reported in the other previous study at five European sites [25], North China plain [26], and southern Spain [27].

A fitting procedure, on the other hand, is the method for estimating the unknown target values using known data. In this study, we employed polynomial interpolation:

$$f_n(x) = \sum_{i=0}^{n} L_i(x) f(x_i). \tag{2-39}$$

Here, $f_n(x)$ is an unknown parameter which will be estimated based on several known data, $f(x_i)$. The number of data used in interpolation procedure is unlimited, n, where the $L_i(x)$ is the multiplication series of known data, x. The $L_i(x)$ is computed using:

$$L_i(x) = \prod_{\substack{i=0 \\ i\neq j}}^{n} \frac{(x-x_j)}{(x_i-x_j)} \tag{2-40}$$

Formulation in equations (2-39) and (2-40) are summarized from references [64], [65], and [66]. This method has been applied in remote sensing phenomena for computing sub-pixel disparity of the image [67]. The formulation of interpolation methods is explained in Appendix-D.

3. INSTRUMENTS AND METHODS

3.1 The Monitoring Technique and Location

The monitoring technique developed in this research is implemented in Center for Environmental Remote Sensing-Chiba University area (35°37'30" and 140°06'14"), south-east of Tokyo metropolitan, the capital city of Japan (Figure 3.1). Due to this observation ground-based instrument from the surface and employed satellite from space, measurements are carried out in clear sky condition when Landsat-8 satellite overpass. The overpass time which has been choices are on October 27, 2017, January 31, 2017, March 20, 2017, and May 23, 2017. At that time both PPI and SP lidar is operated while others ground-based instruments are routinely recorded aerosol and weather parameters. At the same time, Himawari-8 satellite with geostationary orbit covered Kanto area. In this observation, Himawari-8 data is employed for 5 minutes before and after the overpass of Landsat-8.

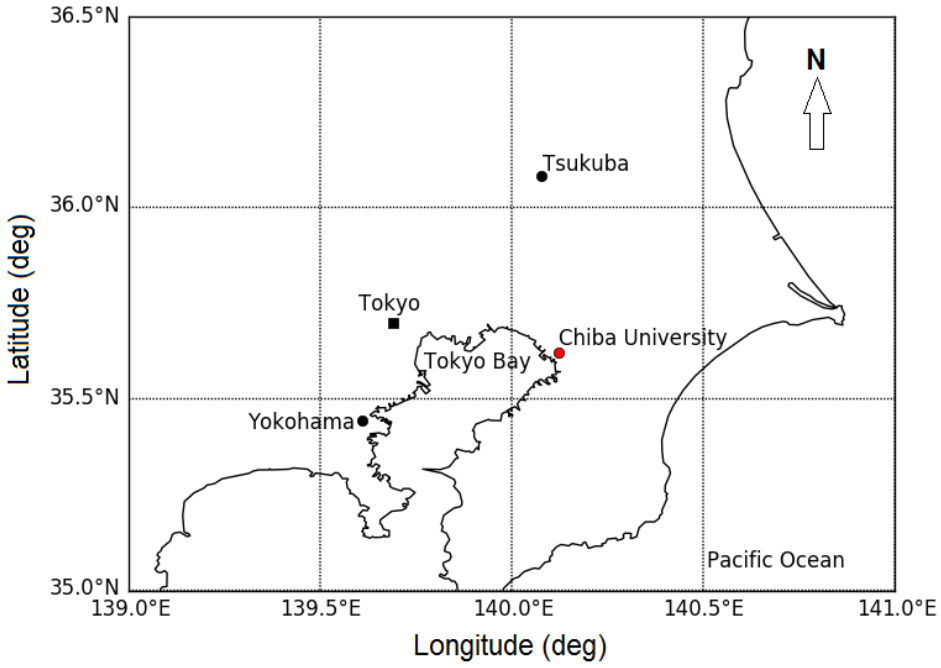

Figure 3.1: The area of interest, the Center for Environmental Remote Sensing (CEReS) - Chiba University-Japan where the ground-based instrument and lidar systems are installed.

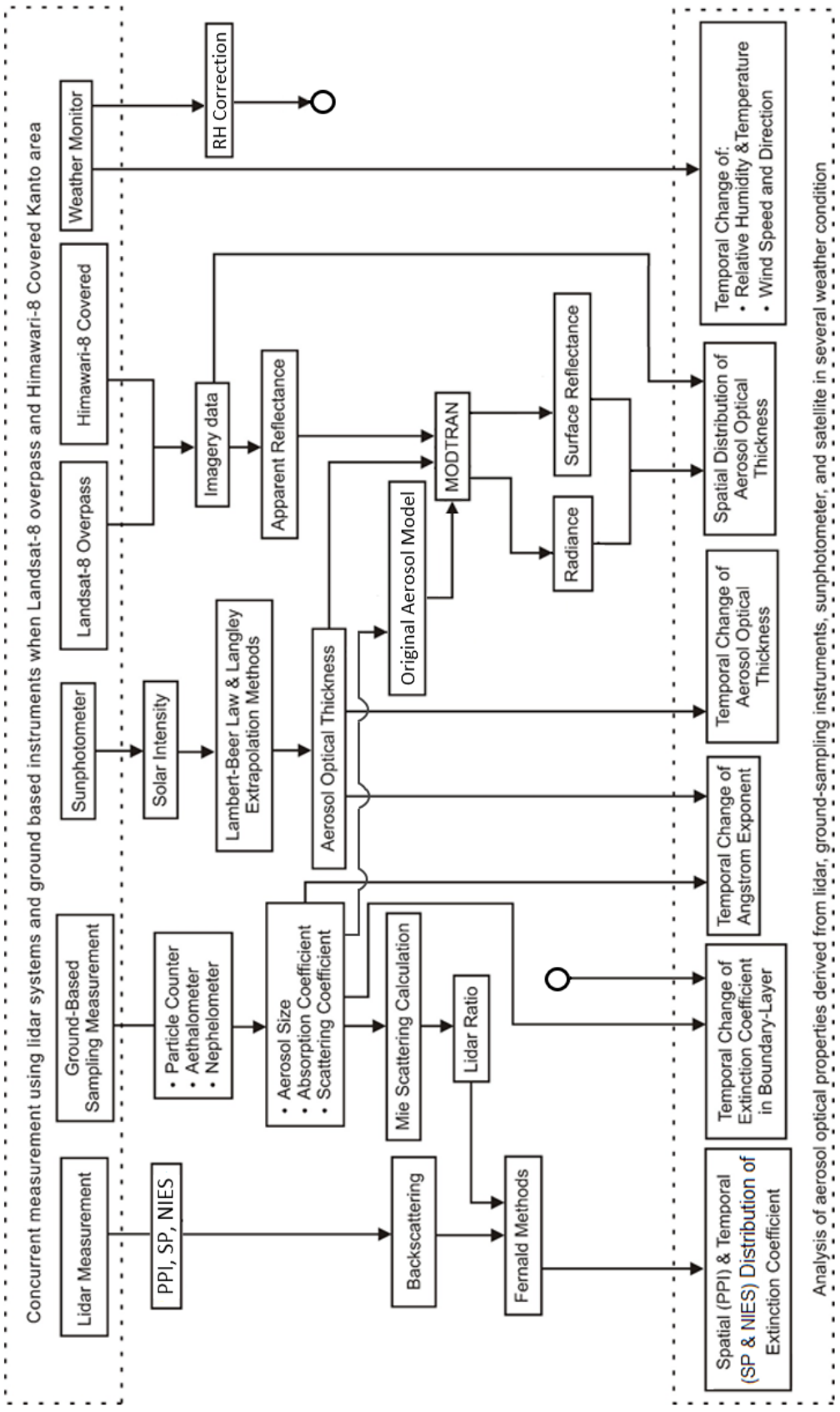

Figure 3.2: Flowchart of the new monitoring technique.

Description of instruments, observation method, data processing, and observed data in this monitoring technique is illustrated in Figure 3.2 and separated into six sections. In section 3.2, weather monitor and atmospheric condition data are presented. The ground sampling instruments and formulation in calculating far-end boundary extinction coefficient are explained in section 3.3, together with Mie scattering calculation for retrieving lidar ratio. Information about instruments and methods in processing PPI, SP, and NIES lidars' signal elucidated in section 3.4 using lidar ratio in the previous section. Furthermore, the sunphotometer data with processing method to retrieve AOT, accompanied by skyradiometer is described in section 3.5. Finally, explanation about satellite data processing is displayed in section 3.6.

3.2 Weather Monitor and Atmospheric Parameters

The weather monitor installed in CEReS is Vantage Pro 2 which is produced by Davis Instruments Corp. USA [68]. The scheme and model of weather monitor are showed in Figure 2.9. This instrument routinely operated for monitoring weather conditions in CEReS and around with 5 minutes range. Atmospheric condition detected using are: air pressure (hPa), wind direction (^{o}), wind speed (m/s), relative humidity (%), absolute humidity (g/m^3), rain rate (mm/h), temperature (^{o}C).

Figure 3.3: Weather monitor installed in CEReS-Chiba University for monitoring the temporal change of ambient RH, temperature, air pressure, wind speed, and wind direction.

Figures 3.4 to 3.7 show the original data which are recorded by Vantage Pro 2 weather monitor installed in CEReS – Chiba University. The real-time data collected on the day Landsat-8 satellite overpass and Himawari-8 satellite cover Kanto plan.

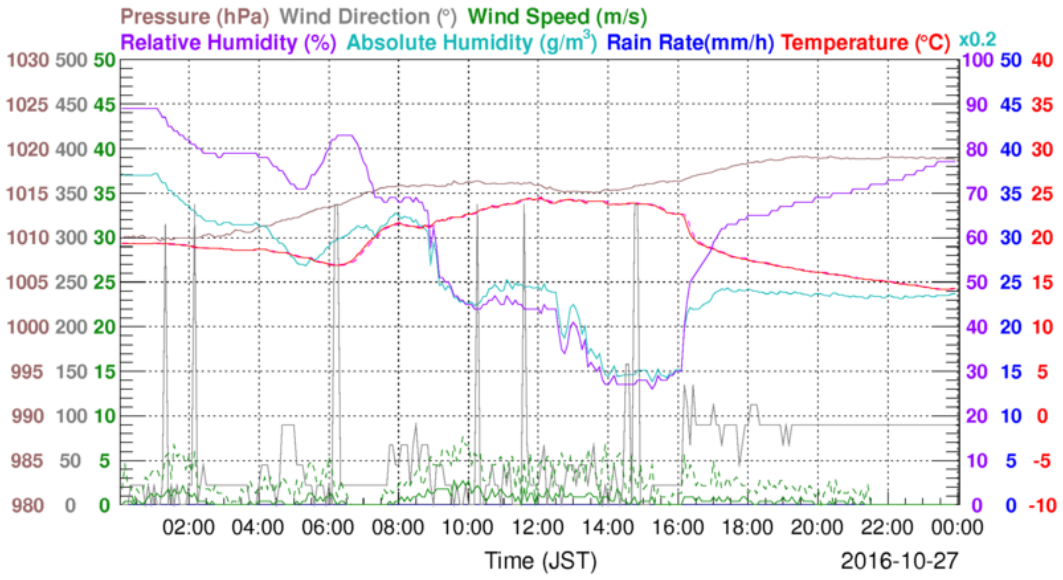

Figure 3.4: Weather monitor data in 2016-10-27.

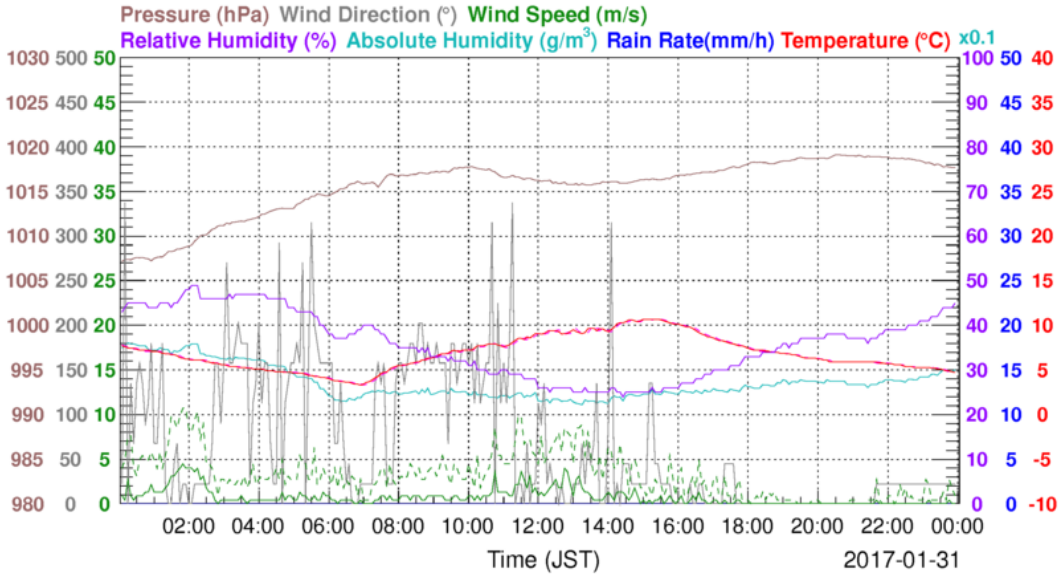

Figure 3.5: Weather monitor data in 2017-01-31.

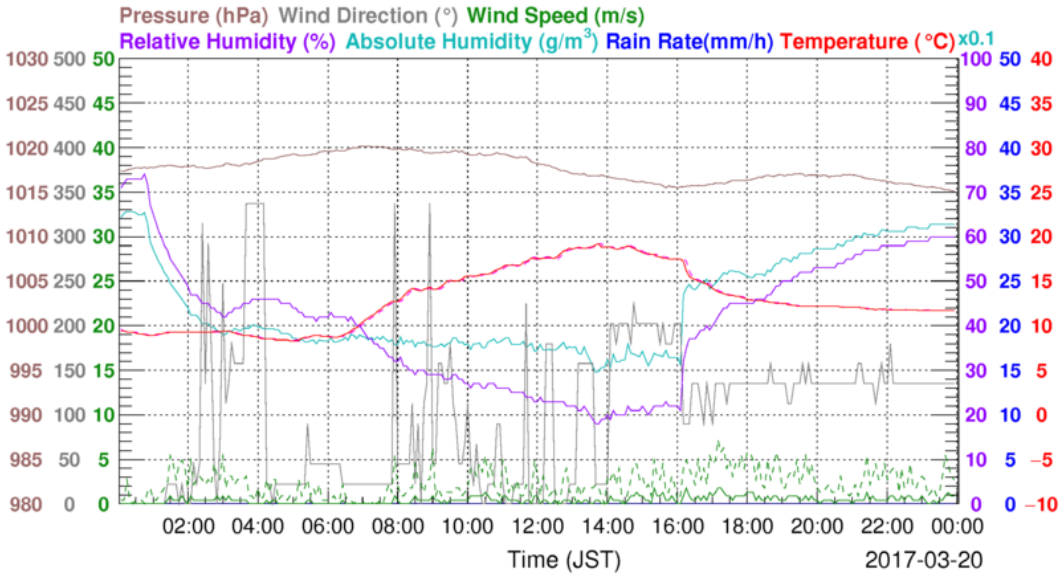

Figure 3.6: Weather monitor data in 2017-03-20.

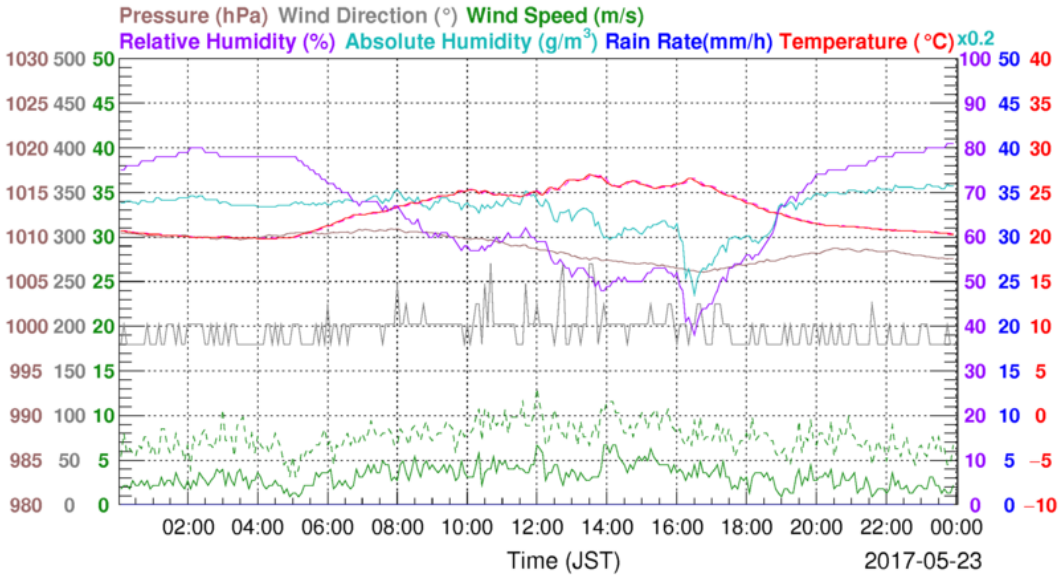

Figure 3.7: Weather monitor data in 2016-05-23.

3.3 Aerosol Extinction Coefficient of Sampling Instruments and Mie Scattering Calculation

To monitor the aerosol optical properties inside the boundary layer, the following ground-sampling instruments are routinely operated on the same rooftop as the PPI lidar. The upper part is the scheme of ground sampling instruments while the under part of this figure consist of a three-wavelength integrating nephelometer

(TSI, Model 3563), an aethalometer (Magee Scientific, AE-31), and an optical particle counter (Rion, KC-22B, KC-01D, KC-01E) respectively.

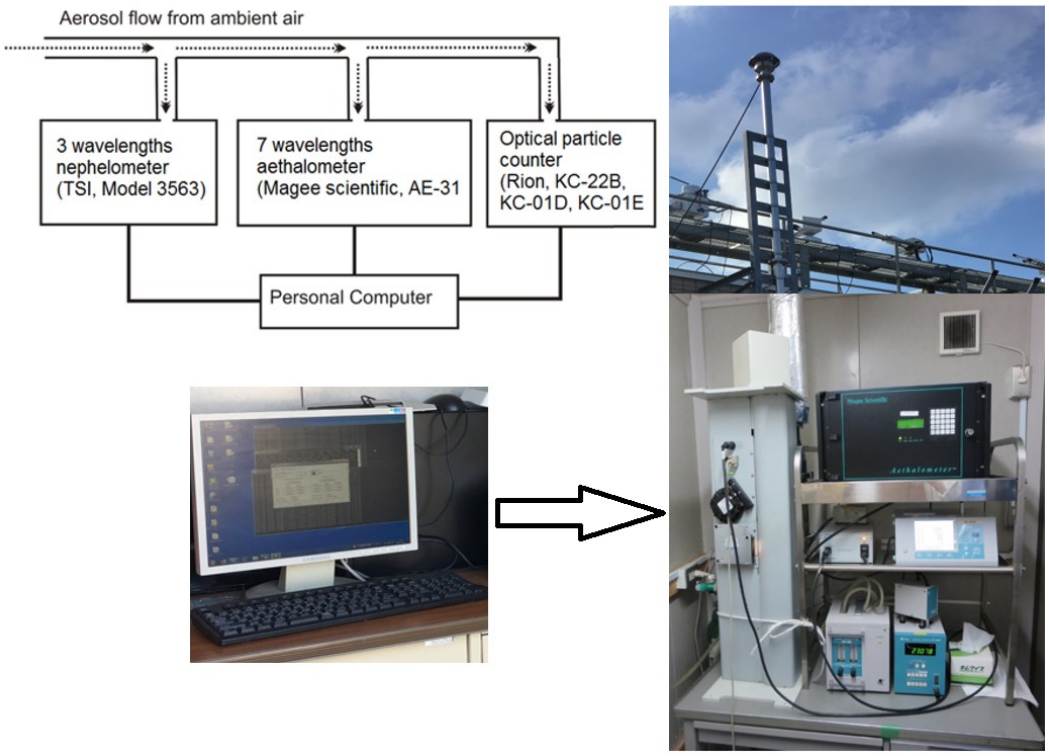

Figure 3.8: The ground-based sampling instruments (a nephelometer, an aethalometer, and an optical particle counter) installed on the 9th-floor engineering building.

The data employed in this analysis is recorded at the day Landsat-8 overpass. Both original and time stamp data of the three ground-sampling instruments are shown in Figures 3.9 to 3.20. The turns are started from a nephelometer, an aethalometer, and an optical particle counter. Time stamps data for aethalometer for every figure below are different from two others instruments, where absorption coefficient (α_{abs}) for every wavelength (λ) is calculated based on black carbon (BC) concentration using the formula:

$$\boldsymbol{\alpha_{abs}(\lambda) = \left(BC(\lambda) \times 10^{-9}\right) \frac{6834}{\lambda}} \quad (3\text{-}1)$$

All pictures in Figures 3.9 to 3.20 consist of (a) original and (b) time stamp for every 1 hour.

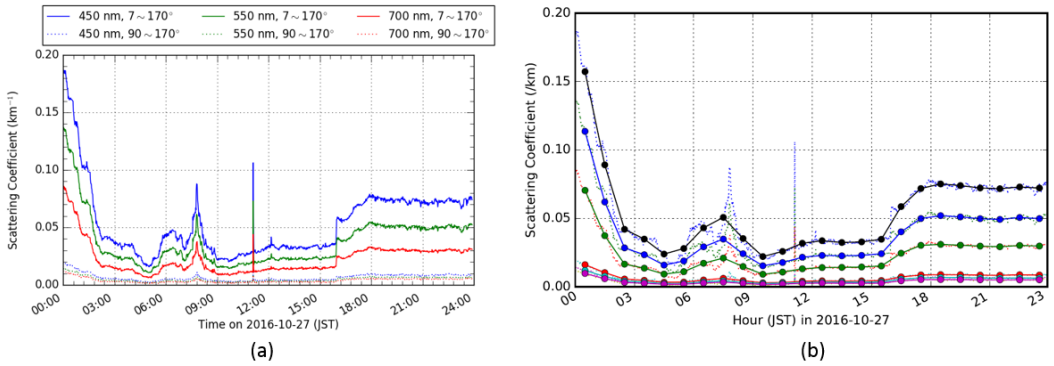

Figure 3.9: Nephelometer data in 2016-10-27.

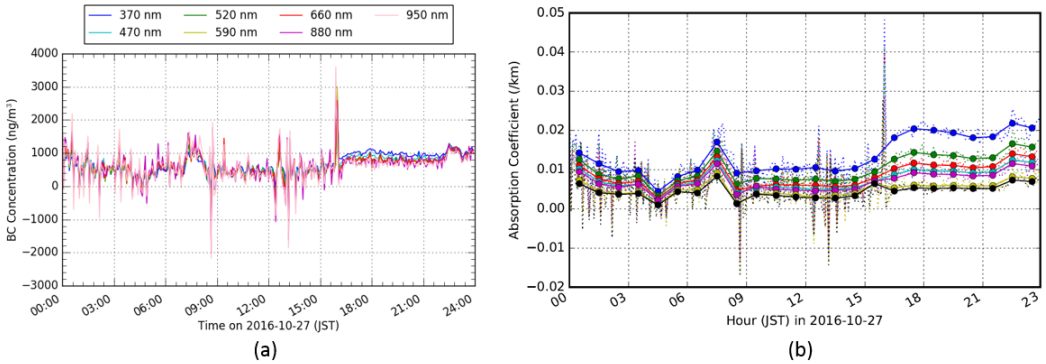

Figure 3.10: Aethalometer data in 2016-10-27.

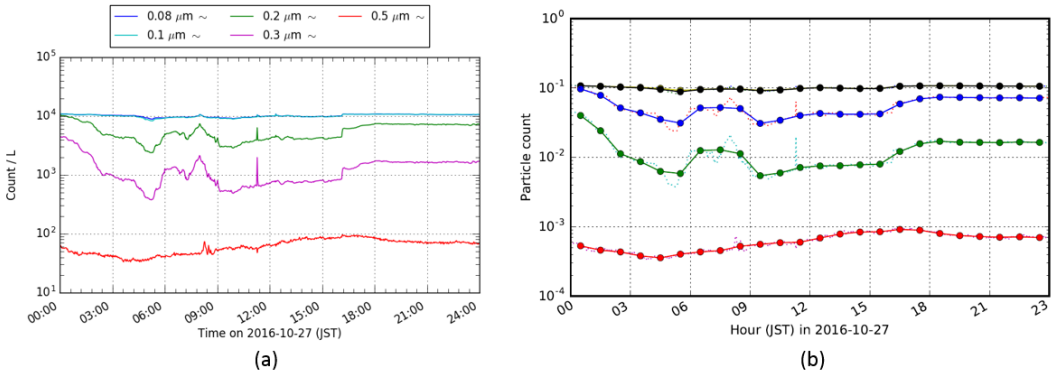

Figure 3.11: Optical particle counter data in 2016-10-27.

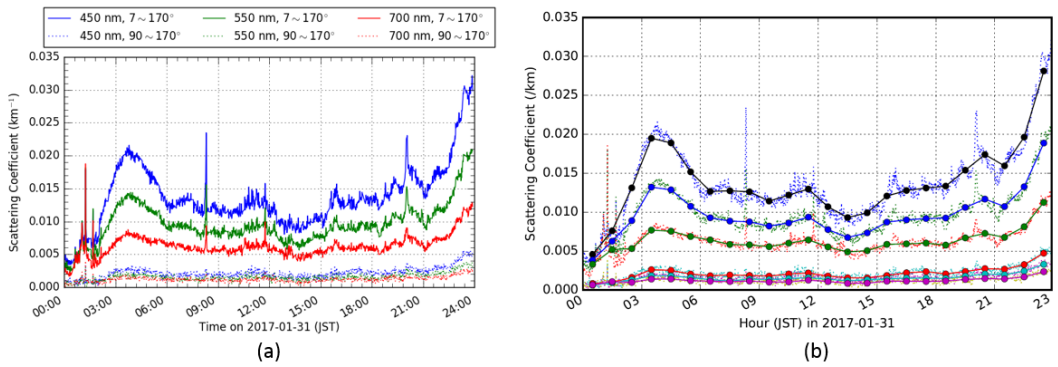

Figure 3.12: Nephelometer data in 2017-01-31.

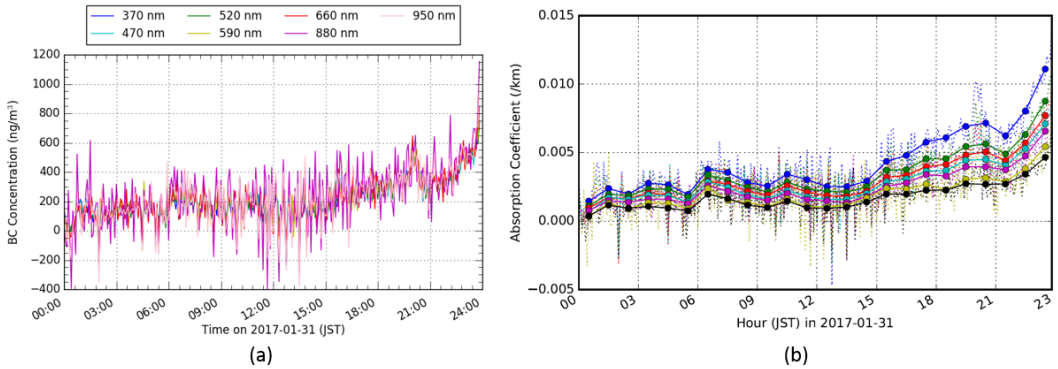

Figure 3.13: Aethalometer data in 2017-01-31.

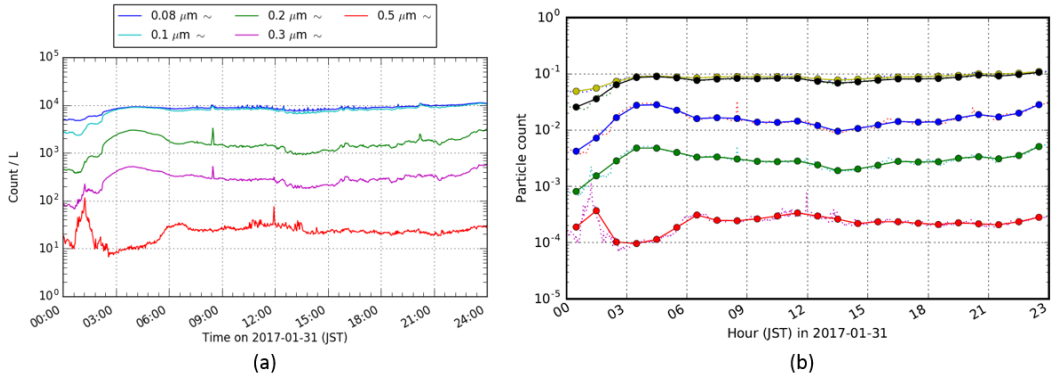

Figure 3.14: Optical particle counter data in 2017-01-31.

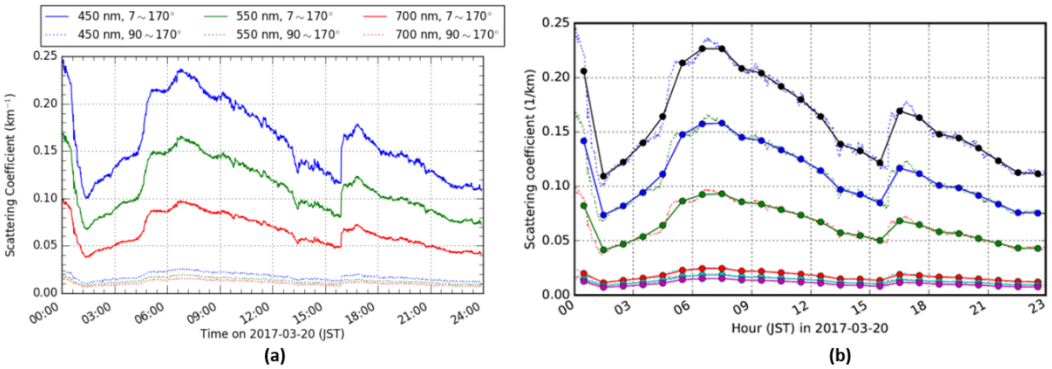

Figure 3.15: Nephelometer data in 2017-03-20.

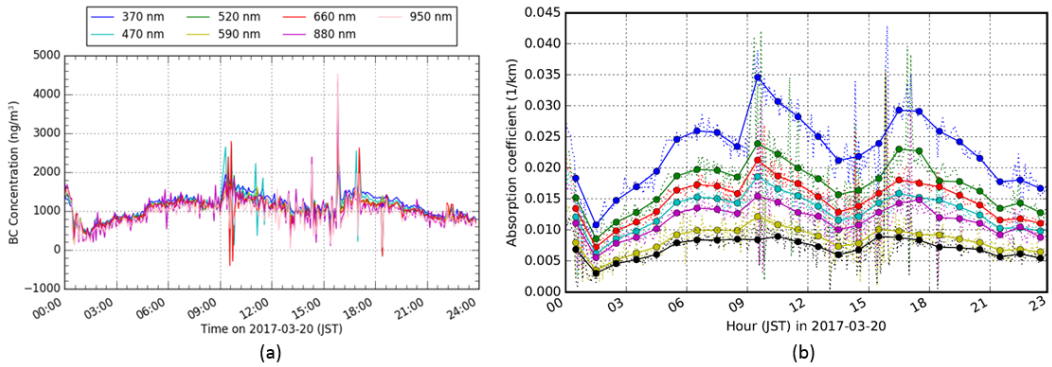

Figure 3.16: Aethalometer data in 2017-03-20.

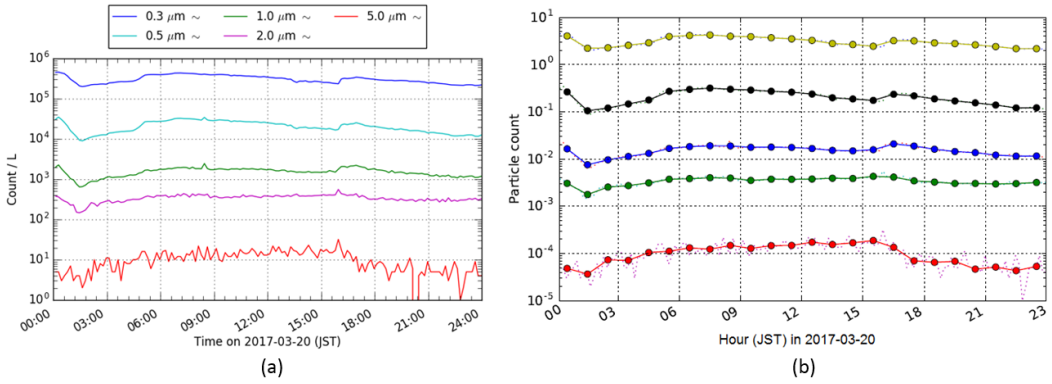

Figure 3.17: Optical particle counter data in 2017-03-20.

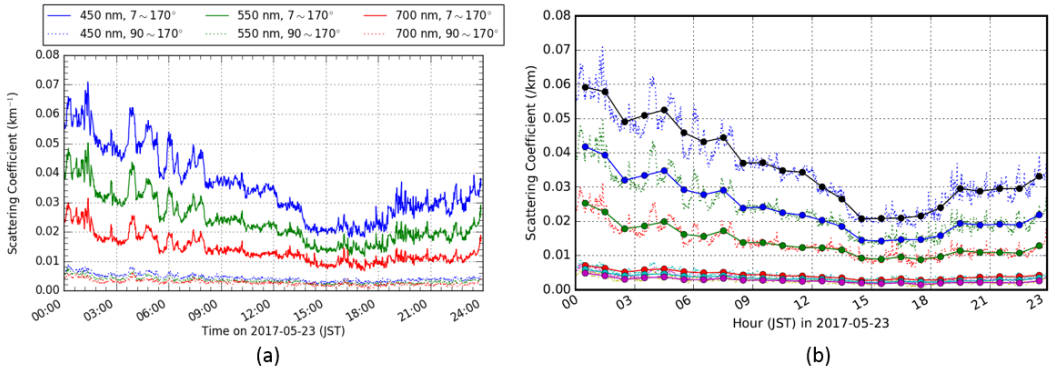

Figure 3.18: Nephelometer data in 2017-05-23.

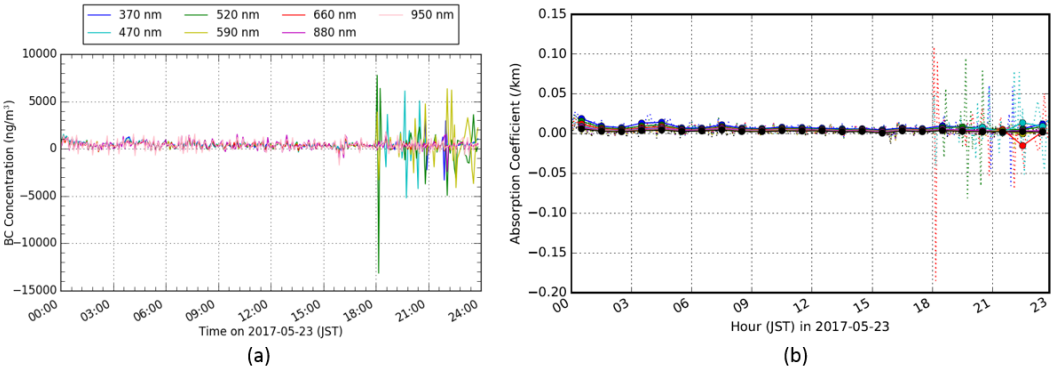

Figure 3.19: Aethalometer data in 2017-05-23.

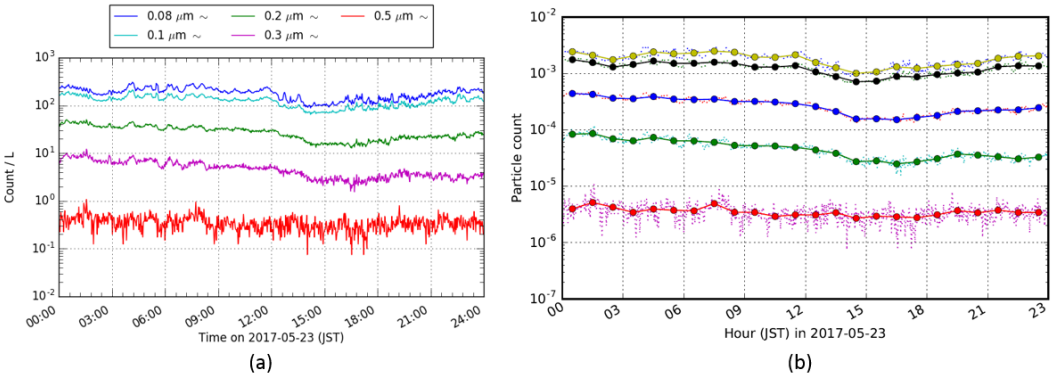

Figure 3.20: Optical particle counter data 2017-05-23.

By means of scattering (α_{sca}) of nephelometer and absorption (α_{abs}) of aethalometer, extinction coefficient (α_{ext}) as a function of wavelength (λ) can be calculated using the equation below:

$$\boldsymbol{\alpha_{ext}(\lambda) = \alpha_{sca}(\lambda) + \alpha_{abs}(\lambda)} \qquad (3\text{-}2)$$

The data employed in this calculation are corrected by using a combination of data in lower and higher RH. Also, the correction procedure represents the turbid and clear atmospheric condition. The correction factor has been published in reference [23] with the formula displayed in Figure 3.21. The optical measurement employed in this correction procedure is visibility-meter (Figure 3.23) which is installed at the CEReS-Chiba University.

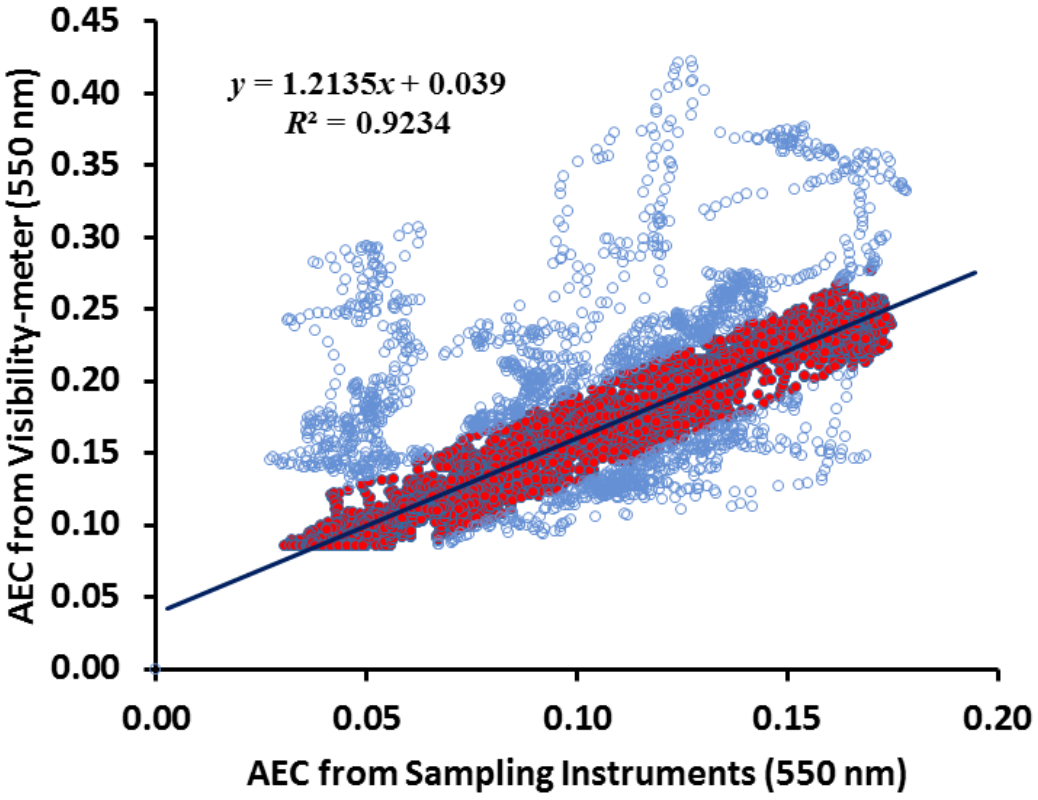

Figure 3.21: The truncation correction of AEC for correcting the sampling procedure which is resulted from comparison between the sampling measurement (x) and the optical measurement (y). All the data involved in this procedure are combination of lower and higher RH for the periods of March and May, respectively.

Figure 3.22: The visibility-meter with the wavelength 550 nm installed on the 9th floor of engineering building.

Lidar ratios for 349 nm and 532 nm of PPI and SP lidars respectively are calculated by applying the Mie scattering calculation to the sampling data. For the formula of Mie calculation to determine extinction (α) to backscattering (β) ratio or lidar ratio (S_1) given as

$$\boldsymbol{S_1 = \frac{\alpha_{ext}}{\beta} = \frac{\int_0^\infty n^{(model)}(r)\,\sigma_{ext}\,d(\log r)}{\int_0^\infty n^{(model)}(r)\left(\frac{d\sigma_{sca}}{d\Omega}\right)_{\theta=\pi} d(\log r)}} \tag{3-3}$$

In this computation, we use the mode concentration (N_i), mode radius ($r_i^{(m)}$), width ($\log r_i$), and refractive index. The refractive index consist of real and imaginary parts. The general procedure of Mie scattering calculation fitted with the real data of ground-sampling instruments (scattering, absorption, and particle size) is developed from references [14], [17],[18],[69],[32]. Furthermore, the lognormal size distribution is computed using:

$$\boldsymbol{n^{(model)}(r) = \frac{dN(r)}{d(\log r)} = \sum_i^k \frac{N_i}{\sqrt{2\pi}\,\log\sqrt{2\pi}\log\sigma_i} \exp\left[-\frac{\left(\log r/r_i^{(m)}\right)^2}{2\,(\log\sigma_i)^2}\right]}, \tag{3-4}$$

and the differential cross-section is related to the total cross-section as:

$$\frac{d\sigma_{sca}}{d\Omega} = \sigma_{sca} f(\cos\theta), \quad (3\text{-}5)$$

The differential cross-section in equation (3-5) employ the phase function of scattering $f(\cos\theta)$ derived from the interpolated data of the nephelometer data.

The lidar ratio value is determined by a fitting parameter of Mie calculation (mode radius, variance, and both real and imaginary parts refractive index) to real data of ground instruments (scattering, absorption, and size particles) [5], [10], [11], [13]. The value of lidar ratio which is obtained in this step is used in Fernald calculation method. Also, the resulting aerosol parameters are used in the radiative transfer calculation using MODTRAN for computing both Landsat-8 and Himawari-8 satellites data.

3.4 Aerosol Extinction Coefficient of Lidar System

The PPI lidar is installed at the rooftop of 9th floor of CEReS building about 30 m above the ground. The transmitted light of PPI lidar is generated from a diode-laser-pumped Nd:YLFat 349 nm with 60 μJ/pulse and 300 Hz pulse repetition rate. For correcting the backscattered signals, we use a 30-cm diameter Cassegrainian telescope coupled with a flat mirror tilted at ~45°. The recorder spare part consist of a photomultiplier tube (Hamamatsu, H10304-00) and a transient recorder (Licel, TR20-160). The whole system of PPI lidar showed in Figure 3.22 can be rotated over 360^{o} for covering all the horizontal directions. The maximum range of PPI observation is approximately 3 km. At the same time, the SP lidar is employed for covering the non-overlapping region of the vertical observation lidars. The SP lidar utilizes a diode-laser-pumped Nd:YAG laser at 532 nm with 200 μJ/pulse and 1000-3000 Hz pulse repetition rate. A photo multiplier tube and a transient recorder for recording the signals as shown in Figure 3.23 [5], [13], [70]. To confirm the temporal change of extinction coefficient derived from SP lidar, the 532 nm of NIES lidar also employed in this study with the scheme is showed in Figure 3.24.

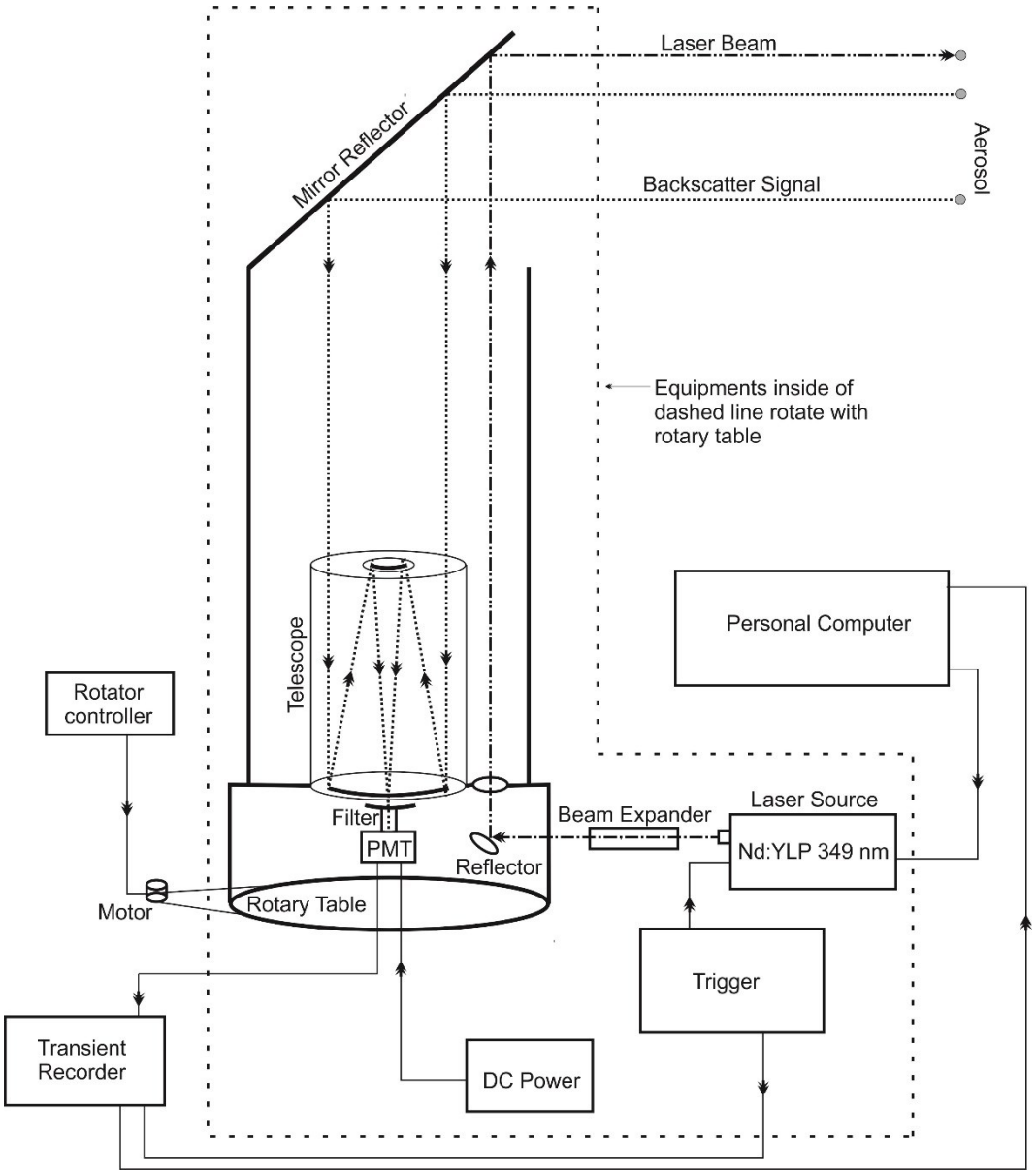

Figure 3.23: The PPI lidar installed on the 9th floor of engineering building is collected signal by rotating 360 near horizontal direction (~4 degrees).

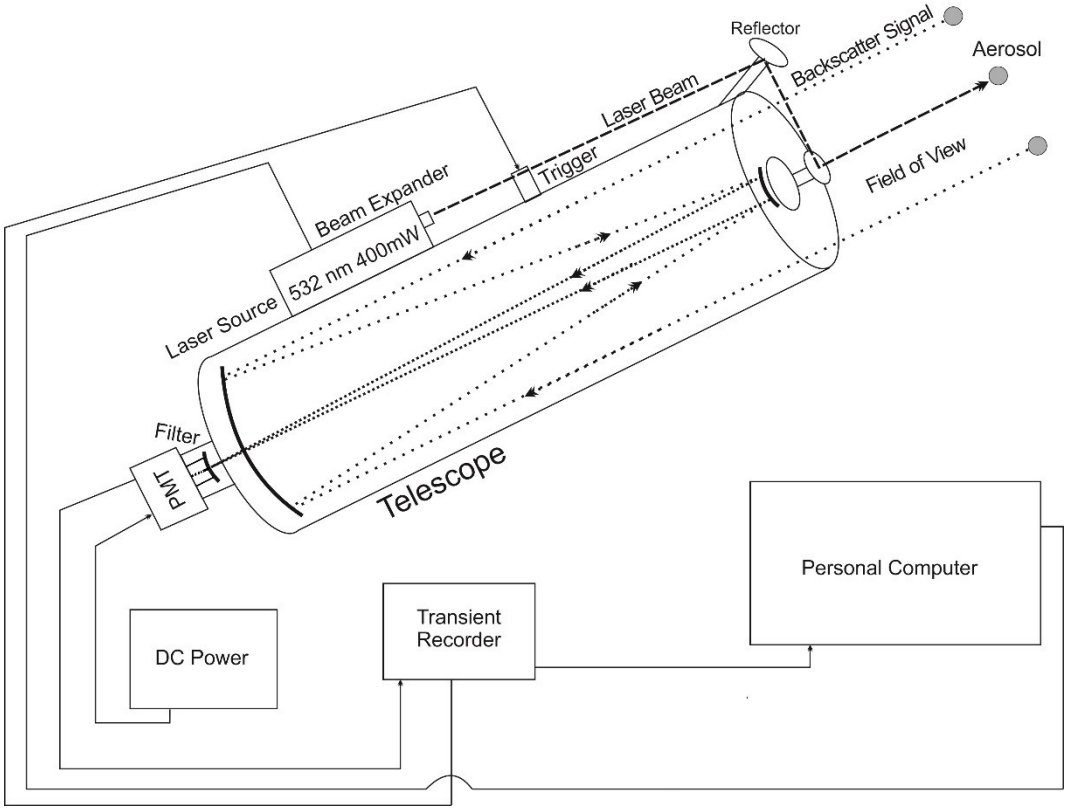

Figure 3.24: The SP lidar installed on the 5th floor of CEReS building in the area of Chiba University with the signal in the north direction and ~30 degrees from the horizontal direction.

Due to diode-laser-pump0ed Nd:YLFat 349 nm of PPI lidar operated in 300 Hz pulse repetition rate and 18000 shots, this system collected raw signal in 1 minute. Therefore, by adjusting the angular speed 0.2 degrees per second we obtained 360 degrees scanning time in around 30 minutes to display the special distribution of extinction coefficient. Furthermore, to collect raw signal in 1 minute for SP lidar with diode-laser-pumped Nd:YAG 532 nm we operated the system in 1000 Hz pulse repetition rate and 60000 shots. Then, the temporal distribution of aerosol extinction coefficient is displayed in time high indicator for SP at the same time with PPI. Figure 3.25 and 3.26 show instrument alignment and signal of PPI and SP lidars respectively. The range of SP lidar is longer than PPI lidar. Finally, Figure 3.27 shows the three lidar system installed in Chiba University which is used in this study.

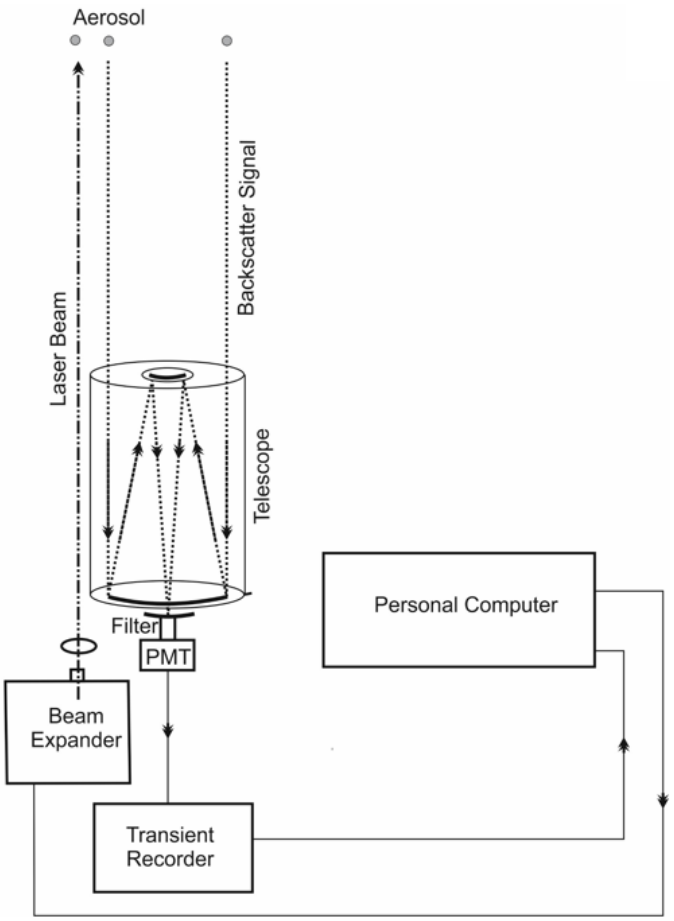

Figure 3.25: The NIES lidar installed on Chiba University-Nishi Chiba Campus.

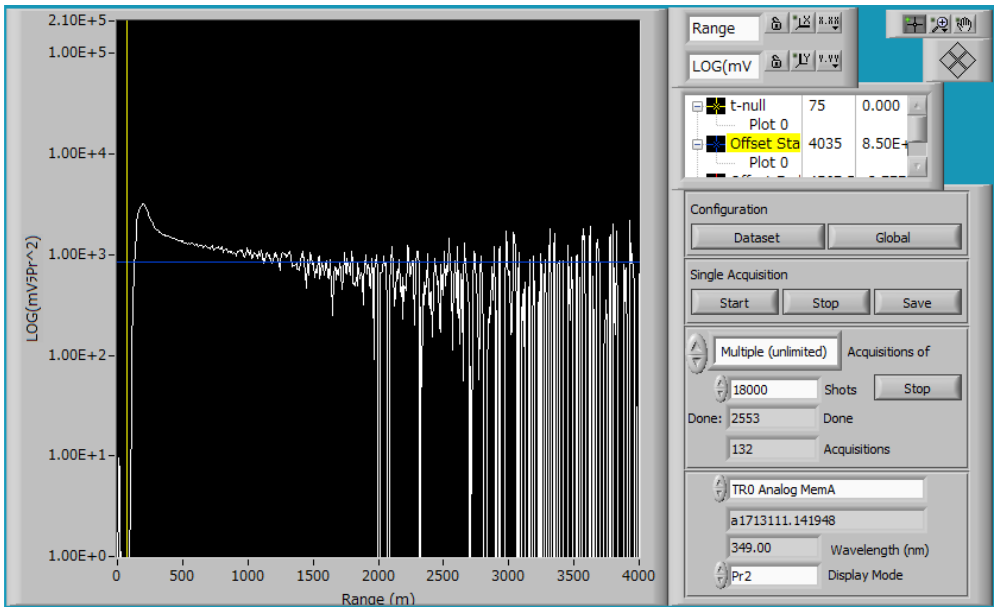

Figure 3.26: Instrument alignment and signal monitoring of PPI lidar.

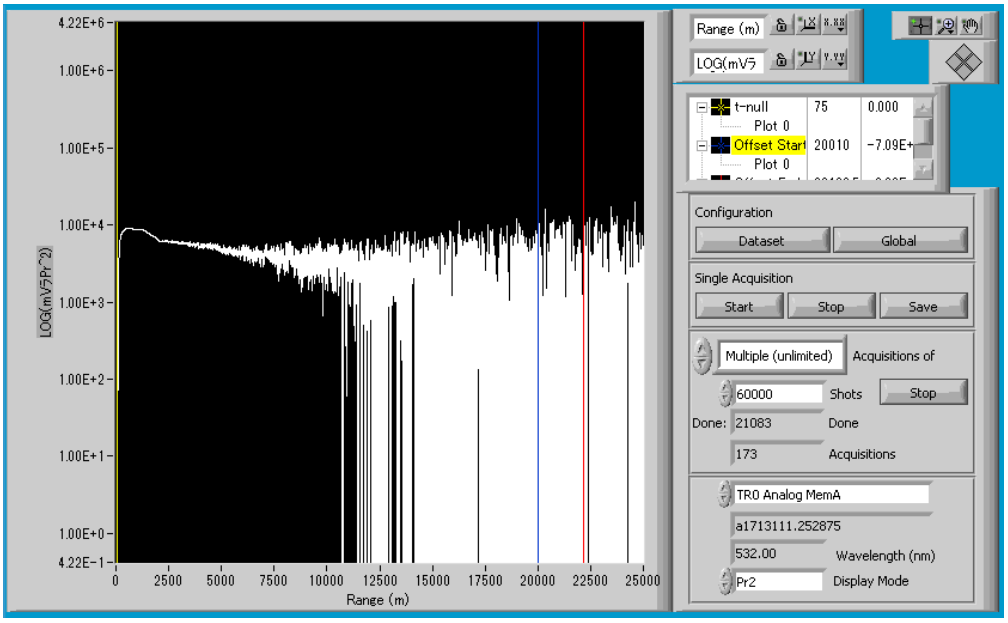

Figure 3.27: Instrument alignment and signall monitoring of SP lidar.

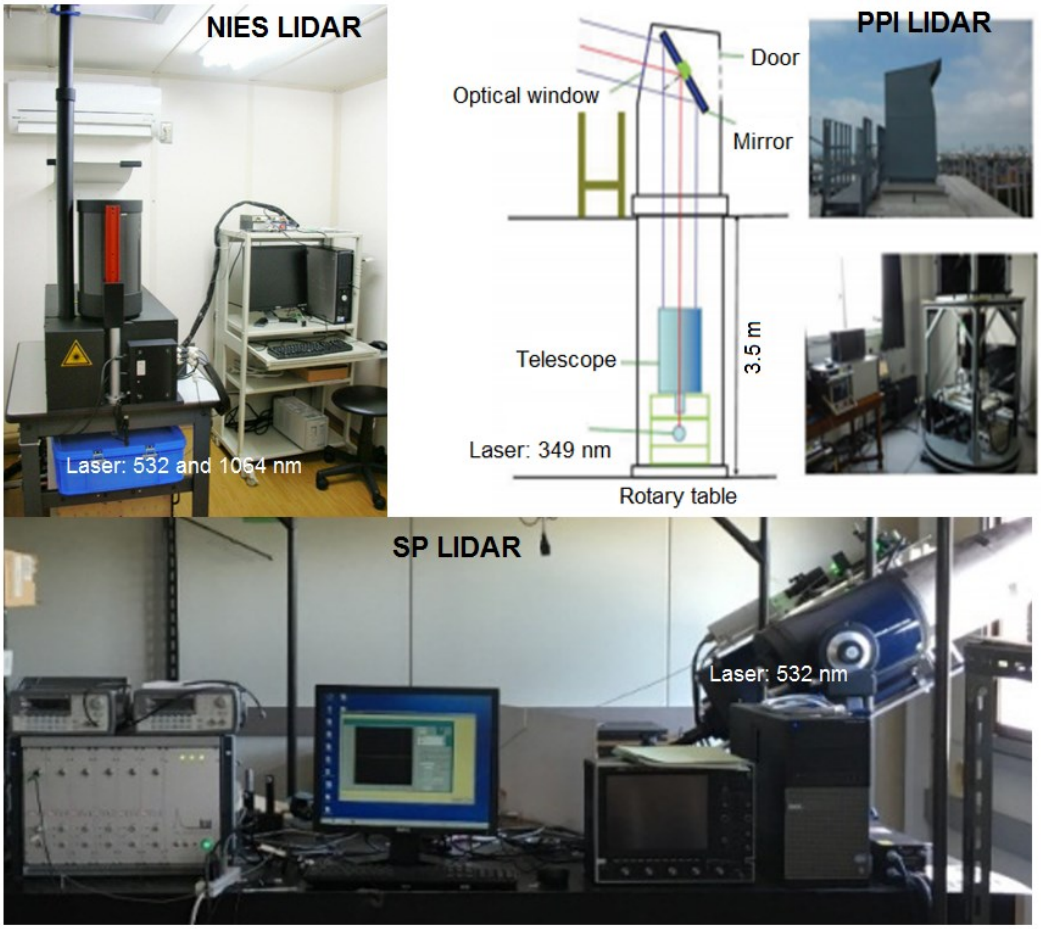

Figure 3.28: Lidar system installed in CEReS, Chiba University-Japan.

Inversion signals recorded by both PPI and SP lidars are analyzed using Fernald methods to obtain aerosol extinction coefficient. The solution of the lidar equation is analytically described as

$$\alpha_1(R) = -\frac{S_1(R)}{S_2}\alpha_1(R) + \frac{\boldsymbol{S_1(R)\,X(R)\exp\left\{2\int_R^{RC}\left[\frac{S_1(R')\,X(R')}{S_2}-1\right]\alpha_1(R')\,dR'\right\}}}{\boldsymbol{\frac{X(R_C)}{\frac{\alpha_1(R_C)}{S_1(R)}+\frac{\alpha_2(R_C)}{S_2(R)}}+\int_R^{RC}S_1(R')\,X(R')2\int_R^{RC}\left[\frac{S_1(R')\,X(R')}{S_2}-1\right]\alpha_1(R')\,dR'}}. \quad (3\text{-}6)$$

Where R is the range, $X(R)=R_2P(R)$ is the range-signal where RC is the range-corrected-signal, both S_1 and S_2 are the ratios between the extinction coefficient and backscattering coefficient for aerosol and air molecule respectively [9]. From general property of the Rayleigh scattering of the molecule, S_2 is assumed to equal to 8.52 1/sr [5], [13] while parameter for aerosol (S_1), or lidar ratio, is determined using Mie scattering calculation. The sample of the Fernald method implementation for lidar signal processing is showed in Figure 3.28.

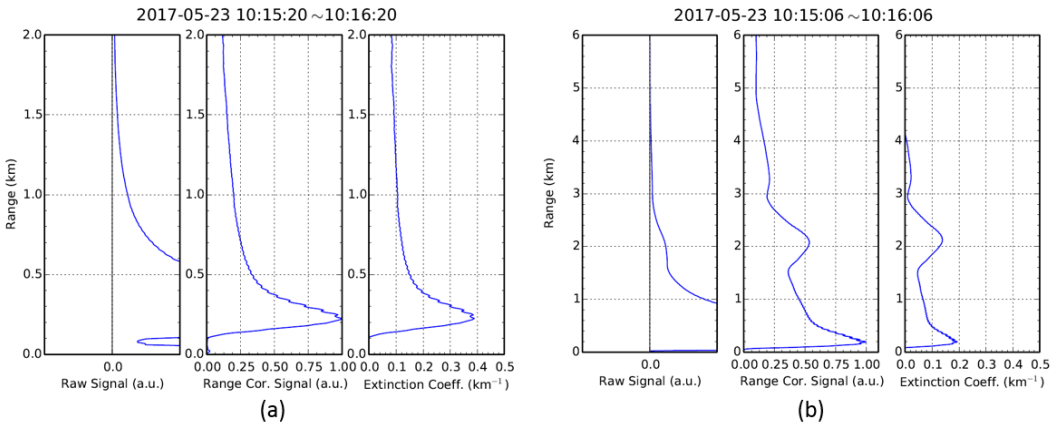

Figure 3.29: Sample of the raw signal, Corrected signal, and extinction coefficient of (a) PPI and (b) SP lidars in 2017-05-23. The PPI range signal is shorter than SP's, but the extinction coefficient of PPI in the far-end boundary layer is higher than SP's. The sample of this signal processing is computed using the Fernald method. This processing is implemented for all data in this study. The complete results in the spatial distribution of PPI and temporal change of SP are presented in Chapter 4: Results and Discussion.

3.5 Aerosol Optical Thickness of Ground Measurement

The AOT measurement process is derived from sunphotometer data at the same time with lidars and ground-based instrument when Landsat 8 overpass and Himawari 8 cover area of interest (Kanto plan). A four-wavelength sunphotometer (368, 500,678, and 778 nm) which is used in this monitoring is routinely operated to monitor solar intensity during the daytime. The sunphotometer is installed on the same floor of the SP lidar (5th floor of CEReS Building- Chiba University). When the cloud influence is insignificant, the sunphotometer data can give good constraint on the aerosol retrieval from lidar measurements. Since the instruments operated real time to measure solar radiation intensity the AOT can be represented in temporal variability. To confirm the AOT of sunphotometer, the independent measurement of skyradiometer with 7 wavelengths (340, 380, 400, 500,675, 870, and 1020 nm) is also employed in this study. Both sunphotometer and skyradiometer used in this study are displayed in Figure 3.27.

The governed of Lambert-Beer law combined with the Langley plot [3], [29], [31] is applied to estimate the AOT of sunphotometer:

$$\boldsymbol{\tau_A(\lambda)} = \frac{\ln \boldsymbol{I_0(\lambda)} - \ln \boldsymbol{I(\lambda)}}{\boldsymbol{m(\theta)}} - \boldsymbol{\tau_G(\lambda)} - \boldsymbol{\tau_R(\lambda)}. \tag{3-7}$$

In this formula, we use variables τ_A, as the aerosol optical thickness corrected with absorbing gases (ozon) and Rayleigh scattering which are symbolize as τ_G and τ_R, respectively. Parameters I_0 is the intensity of solar radiation at the top of atmosphere. The values of I_0 is dependent on the seasonal change of the Sun-Earth distance. Furthermore, the *I*-parameter is the solar radiation intensity measured real time using the sunphotometer, and *m* is the air mass estimated using the temporal change of the solar zenith angle (θ). By means of the sunphotometer data in clear-sky condition where the small aerosol loading, the value of ln I_0 is extrapolated using the Langley plot based on procedure in reference [31].

Figure 3.30: (a) The four-wavelength sunphotometer (368, 500, 678, and 778 nm) installed at the 5th floor of CEReS building, (b) The seven-wavelength (340, 380, 400, 500, 675, 870, and 1020 nm) of skyradiometer installed on the 9th floor of engineering building.

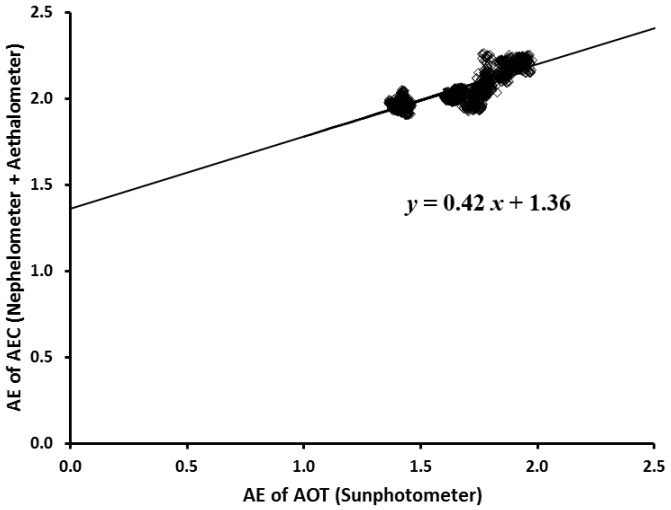

Figure 3.31: The truncation correction of AOT for correcting the sampling procedure which is resulted from comparison between the sunphotometer (x) and the sampling procedure (y). All the data involved in this procedure are combination of lower and higher RH for the periods of March and May, respectively.

Furthermore, the Ångström exponent (p) is inferred from the wavelengths dependence of AOT to derive the information on aerosol size distribution using [31],[71],[72]:

$$\boldsymbol{p = -\ln\left[\frac{\tau_A(\lambda_2)}{\tau_A(\lambda_1)}\right] / \ln\left(\frac{\lambda_2}{\lambda_1}\right)}, \tag{3-8}$$

The value of Ångström exponent is the order of unity which becomes larger in the condition of the dominance of fine-mode aerosol, and smaller for the dominance of

coarse-mode particles [36], [37], [73]. The Ångström exponent values retrieved using equation (3-8) are also confirmed to the independent measurement of skyradiometer. The truncation correction of Ångström exponent employed in this study is used formulation in reference [23] which is presented in Figure 3.29.

In this analysis, the I_0 parameter retrieves by employing sunphotometer data in most clear sky condition which is sought on February 12, 2017 (see Figures 3.30 and 3.31). The sunphotometer data, together with the temporal change of solar zenith and azimuth angles, on that day Landsat-8 satellite overpass Kanto plan, are represented in Figures 3.32 to 3.39. On the figure, panel (a) and (b) are solar position and sunphotometer data, respectively.

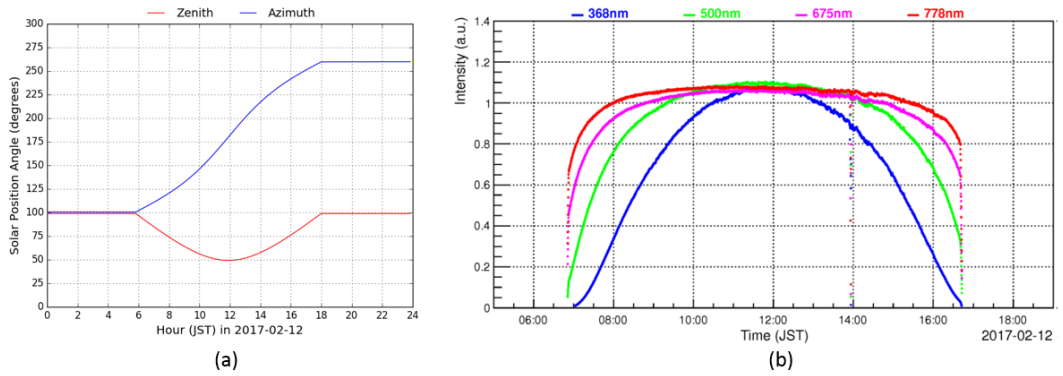

Figure 3.32: Data observed in 2017-02-12 on the clearest sky condition to determine the extra-terrestrial intensity of solar radiation.

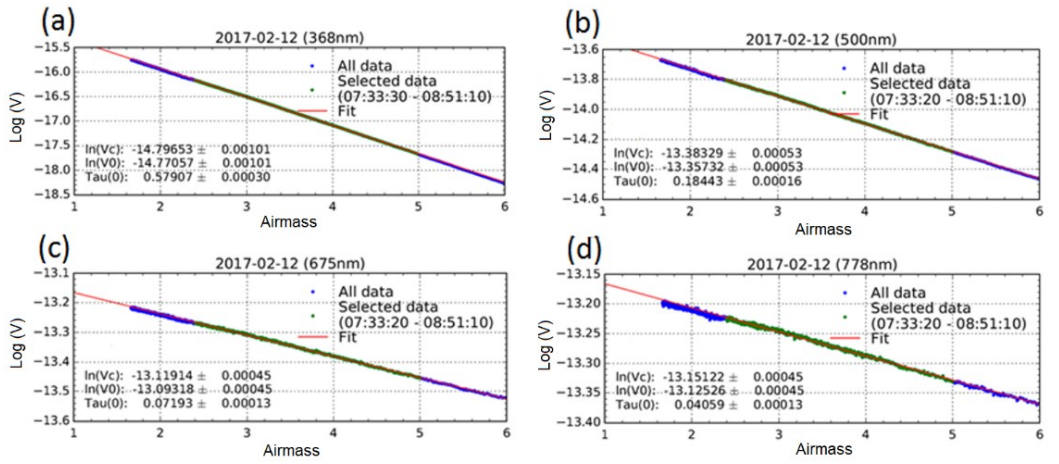

Figure 3.33: Langley plot of the sunphotometer data observed on February 12, 2017. The extrapolation resulted logarithm of solar radiation at the top of atmosphere for every wavelengths (a) ln $I(369)$ = -14.797, (b) ln $I(500)$ = -13.383, (c) ln $I(675)$ = -13.119, and (d) ln $I(778)$ = -14.151.

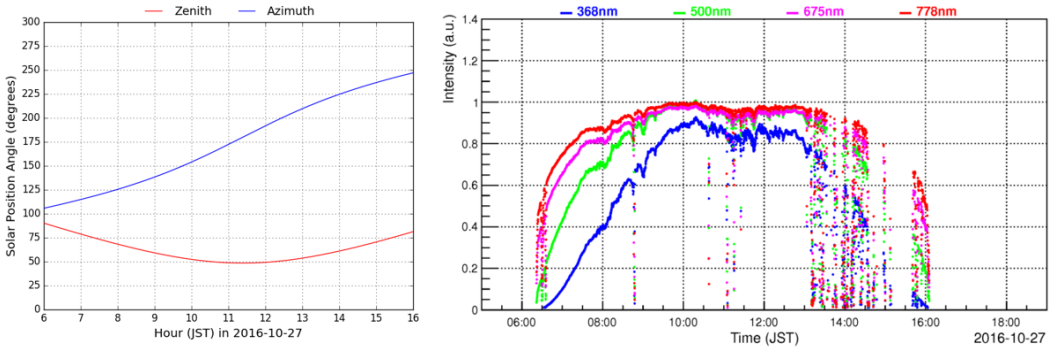

Figure 3.34: (a) solar position and (b) sunphotometer data in 2016-10-27.

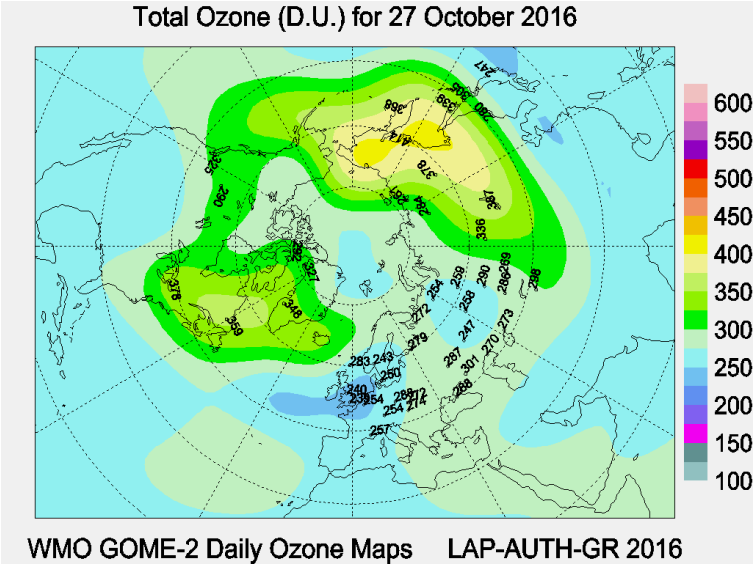

Figure 3.35: Total ozone in 2016-10-27 for Chiba area 247 DU (Dobson Unit).

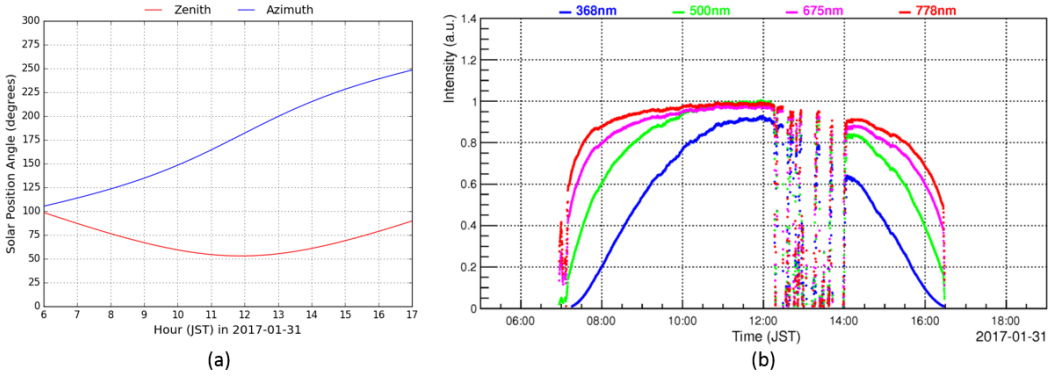

Figure 3.36: (a) solar position and (b) sunphotometer data in 2017-01-31.

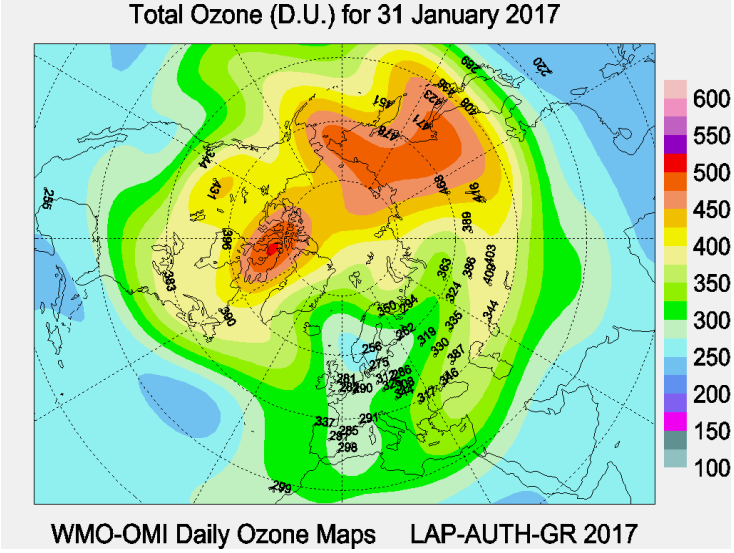

Figure 3.37: Total ozone in 2017-01-31 for Chiba area 314 DU (Dobson Unit).

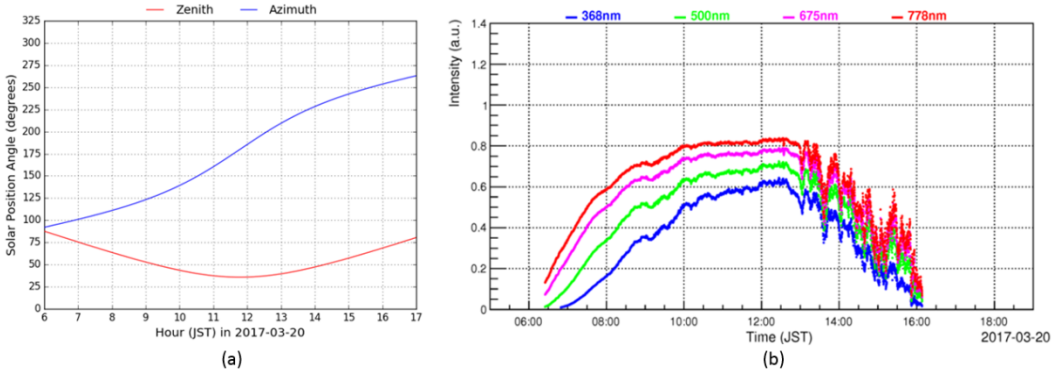

Figure 3.38: (a) solar position and (b) sunphotometer data in 2017-03-20.

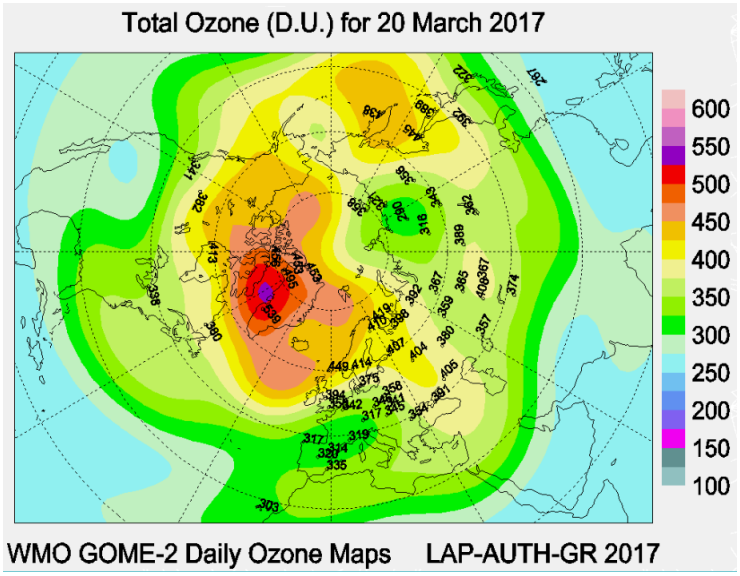

Figure 3.39: Total ozone in 2017-03-20 for Chiba area 303 DU (Dobson Unit).

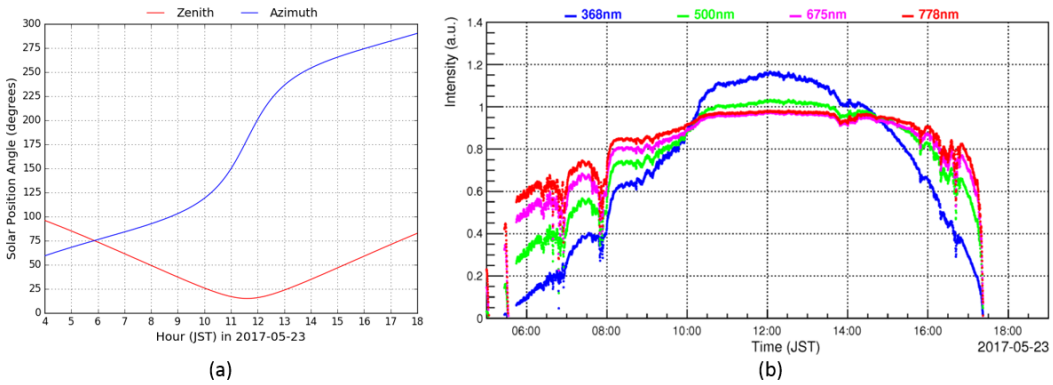

Figure 3.40: (a) solar position and (b) sunphotometer data in 2017-05-23.

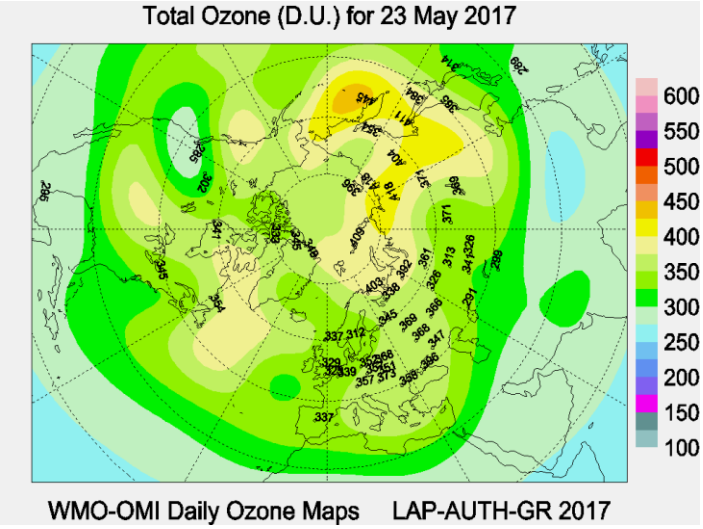

Figure 3.41: Total ozone in 2017-05-23 for Chiba area 289 DU (Dobson Unit).

3.6 Aerosol Optical Thickness of Satellite Data

To calculate AOT of a satellite sensor, we need to employ some related to image data of satellite. A pixel value in digital number (*DN*), radiance (W/m^2 Sr μm), and apparent reflectance (dimensionless) are the significant parameters for obtaining surface reflectance which is used in estimating AOT. By means of the formula in calculating observed radiance (L_{obs}) and apparent reflectance (ρ_{ar}) as a function of wavelength (λ), we established formula in reference [7] to calculate apparent reflectance of Landsat-8 satellite:

$$\boldsymbol{\rho_{ar}(\lambda) = \frac{\pi d^2}{E(\lambda)\cos\theta_s} \times \frac{L_{MAX}-L_{MIN}}{Q_{CALMAX}-Q_{CALMIN}} \times (DN - Q_{CALMIN}) + L_{MIN}.} \quad (3\text{-}9)$$

On the other hand, the apparent reflectance of the Himawari-8 satellite can be calculated using an empirical equation which is developed from references [44], [45]:

$$\rho_{ar}(\lambda) = \frac{0.001559\, D^2}{\cos\theta_s} \times \{0.377358 \times DN(\lambda) - 7.547167\} \quad (3\text{-}10)$$

The surface reflectance (ρ_{ar}) of both Landsat-8 and Himawari-8 satellites is estimated by separating the contribution of reflectance from atmosphere and surface using MODTRAN [47]–[53]. The separation process is carried out by means of solar zenith and azimuth angles, accompined by satellite zenith and azimuth angles. The Himawari-8 satellite zenith and azimuth angles are derived from its metadata while for the Himawari-8, satellite zenith (θ_γ) and azimuth (ϕ_γ) angle, accompanied by the satellite field of view (γ) are estimated using formulas, respectively:

$$\theta_\gamma = \tan^{-1}\left[\frac{(6371+35800)\sin\gamma}{(6371+35800)\cos(\gamma-6371)}\right] \quad (3\text{-}11)$$

$$\phi_\gamma = 180^o - \sin^{-1}\left[\frac{\sin(140.104-35.625)}{\sin\gamma}\right], \quad (3\text{-}12)$$

$$\gamma = \cos^{-1}[\cos(35.63)\cos(140.700-140.104)]. \quad (3\text{-}13)$$

Finally, by means procedure in reference [22], the AOT of both Landsat-8 and Himawari-8 satellite is estimated using:

$$\boldsymbol{\tau_A(\lambda) \cong \frac{1}{\left(1+\frac{1}{\cos\theta_s}\right)} \ln\frac{\rho_{sr}}{\rho_{ar}}}. \quad (3\text{-}14)$$

Where, the center wavelength employed in this study are blue and green bands for confirming the wavelength of PPI (349 nm) and SP (532 nm) lidars. The wavelength of Landsat-8 satellite close to the two wavelength is band-2 with the range 452-512 nm (center wavelength 482 nm) and band-3 with the range 533-590 nm (center wavelength 562 nm). On the other hand, the channel of Himawari-8 employed in this study is band-1 with the range 430-480 nm (center wavelength 455 nm) and band-2 with the range 500-520 nm (center wavelength 510 nm).

Among the several visible bands of Landsat-8 and Himawari-8 satellites, blue and green bands of both satellites are used for the present analysis. The radiance that represent band-*i* can be calculated as

$$L_i = \frac{\int_{-\lambda_1}^{\lambda_2} g_i(\lambda) L_{tot}(\lambda) d\lambda}{\int_{-\lambda_1}^{\lambda_2} g_i(\lambda) d\lambda}. \quad (3\text{-}15)$$

Where $g_i(\lambda)$ is the band response function covering the wavelength range from λ_1 to λ_1. Their values are represented in Figures 3.42 and 3.43.

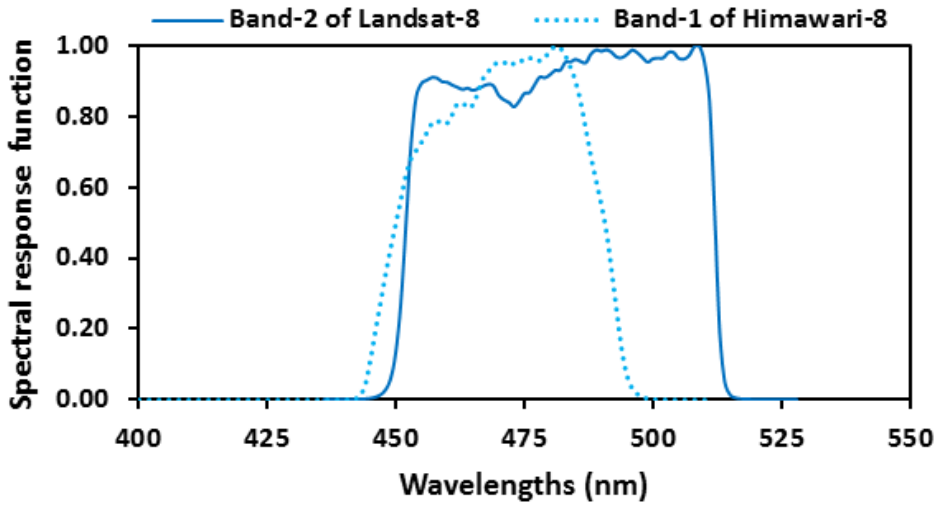

Figure 3.42: Spectral response function of blue bands.

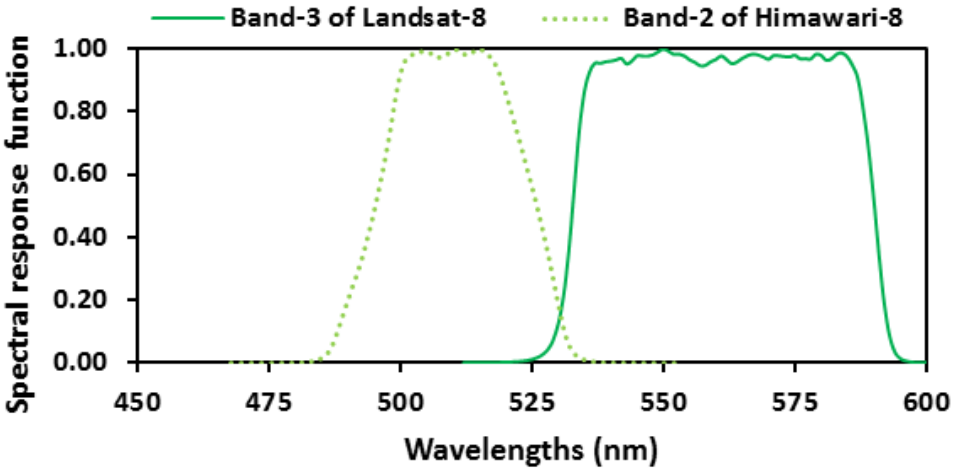

Figure 3.43: Spectral response function of green bands.

4. RESULTS AND DISCUSSION

4.1 Results

The monitoring technique implemented in this study obtained several results. The complete results are divided into 10 sub-sections as a representation of parameters which are observed and estimated in this study. The sub-section 4.1.1 to 4.1.6 consist of ground measurement results. The ground measurements are a combination of sampling, optical, and lidar systems. Finally, the results estimated based on satellite observation are presented in sub-sections 4.1.6 to 4.1.10. The satellites employed in this study are Himawari-8 and Landsat-8.

4.1.1 Atmospheric Condition

The temporal change of atmospheric conditions retrieved from weather is presented in Figure 4.1 to 4.4, where the relative humidity (RH) and temperature are showed in panel (a), while the wind speed and wind direction are presented in panel (b). Both wind speed and wind direction are relatively fluctuative in 2016-10-27, 2017-01-31, and 2017-03-20 but relatively stable in 2017-05-23 with approximately 3-5 m/s of wind speed and average toward East-West of wind direction. The RH and temperature also relatively stable in 2017-05-23 around 50-60 % and 20-25^{o}C, respectively. Therefore, an RH correction for sampling instruments is implemented only for 2017-05-23. The RH in 2016-10-27 fluctuated around 40-70% but the RH in overpass time is under 50%.

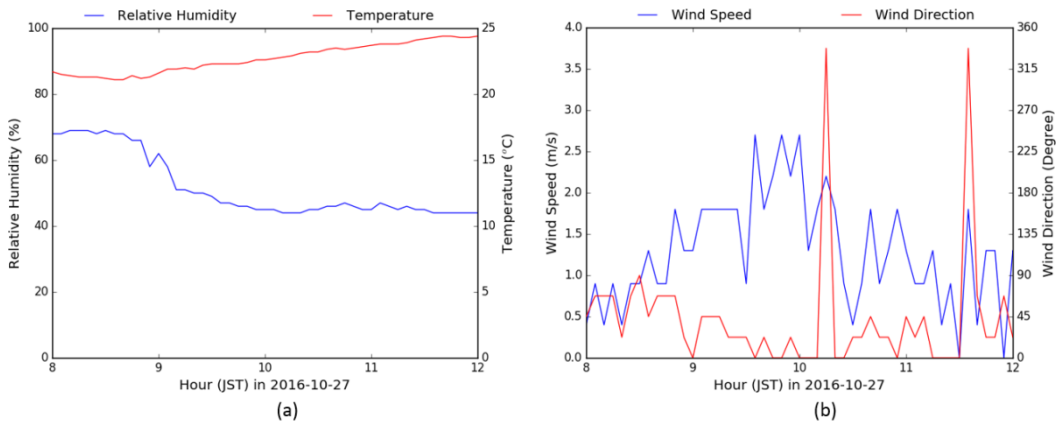

Figure 4.1: The atmospheric condition in 2016-10-27.

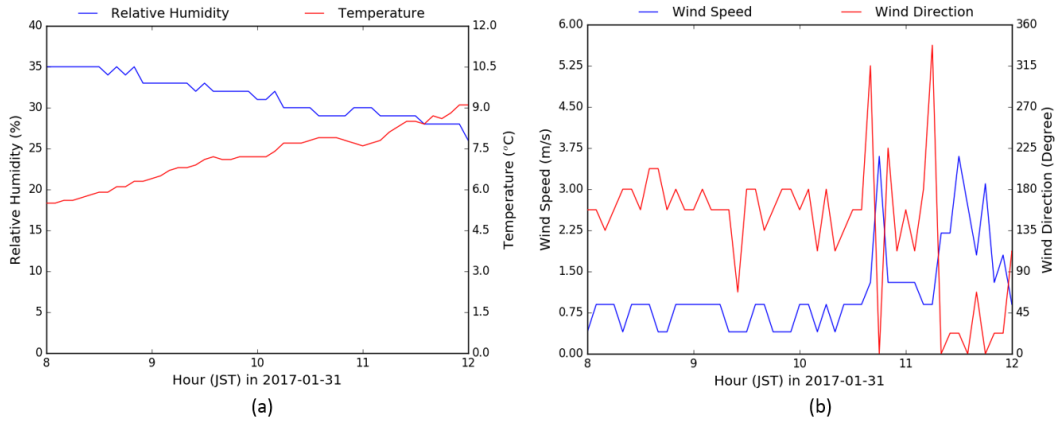

Figure 4.2: The atmospheric condition in 2017-01-31.

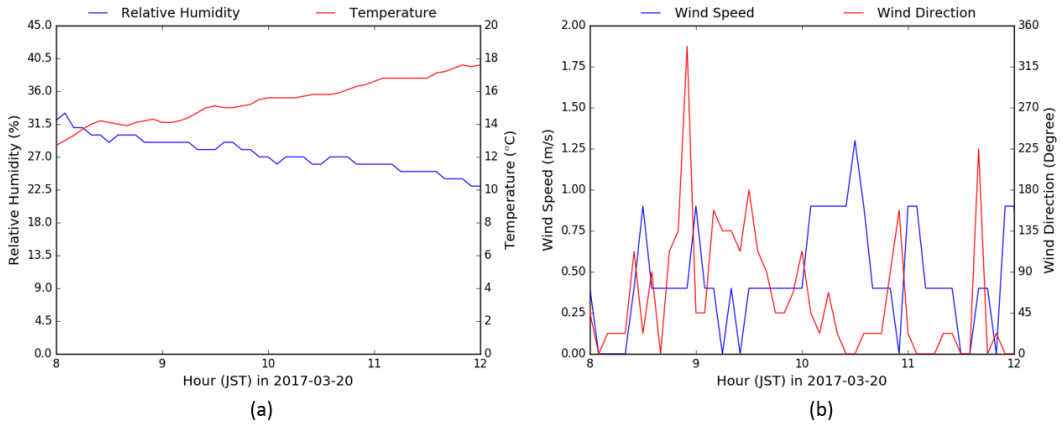

Figure 4.3: The atmospheric condition in 2017-03-20.

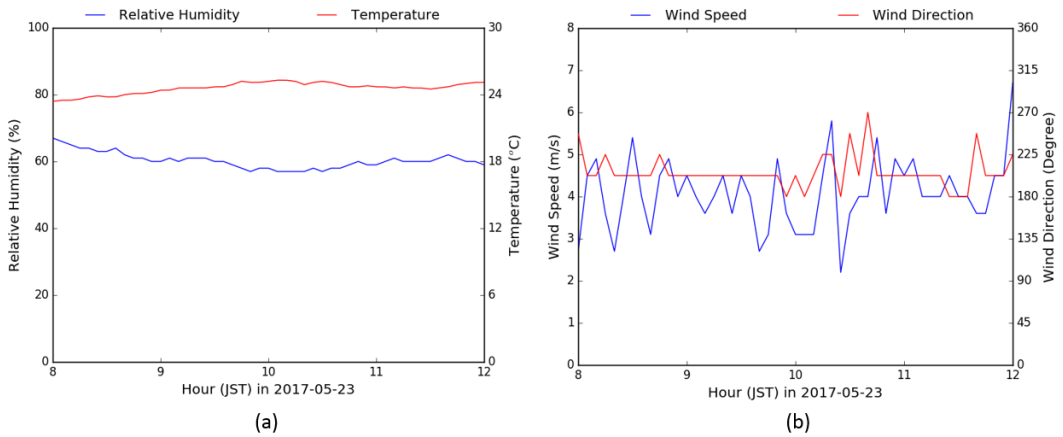

Figure 4.4: The atmospheric condition in 2017-05-23.

4.1.2 Extinction Coefficient of Sampling Instruments

The temporal change of extinction coefficient in the boundary layer is a linear summation of temporal change of both scatterings derived from nephelometer and absorption obtained from aethalometer. We used nephelometer

data directly as the scattering coefficient and calculated absorption coefficient of aethalometer data using equation (3-1). Furthermore, we calculate the extinction coefficient for three wavelengths using equation (3-2). Figures 4.5 to 4.8 plotted the temporal change of sampling measurement and estimation in four panels. Panel (a) is scattering coefficient derived from nephelometer directly and panel (b) absorption coefficient calculated from black carbon concentration of aethalometer data. Panel (c) and (d) are a representation of original and corrected extinction coefficients, respectively. The original extinction coefficient is derived from the linear summation of scattering and absorption coefficient without correction. On the other hand, the corrected extinction coefficient plotted using truncation correction in Figure 3.21 based on reference [23]. In case of higher relative humidity in 2017-05-23, the advance correction is employed, then the result is presented in Figure 4.9 where panel (a) is $f(RH)$ correction and panel (b) is corrected extinction coefficient. In Figure 4.9, the extinction of visibility is fixed to the sampling instruments.

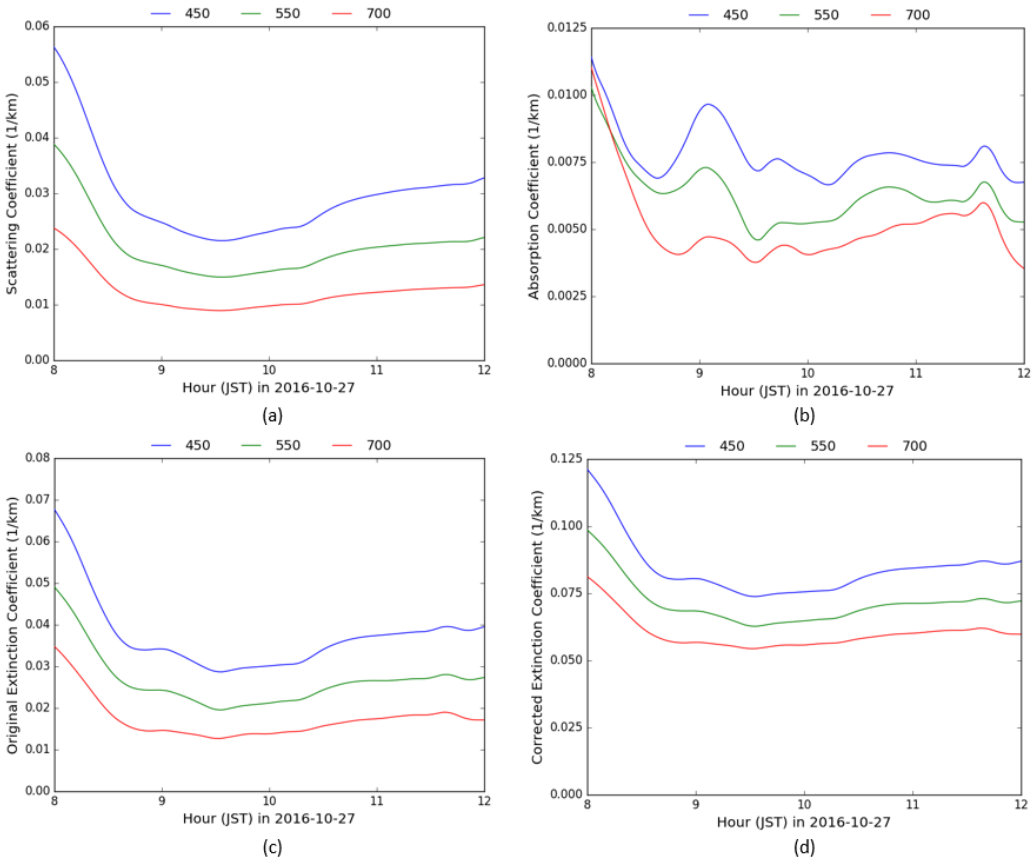

Figure 4.5: Extinction coefficient of sampling instruments in 2016-10-27.

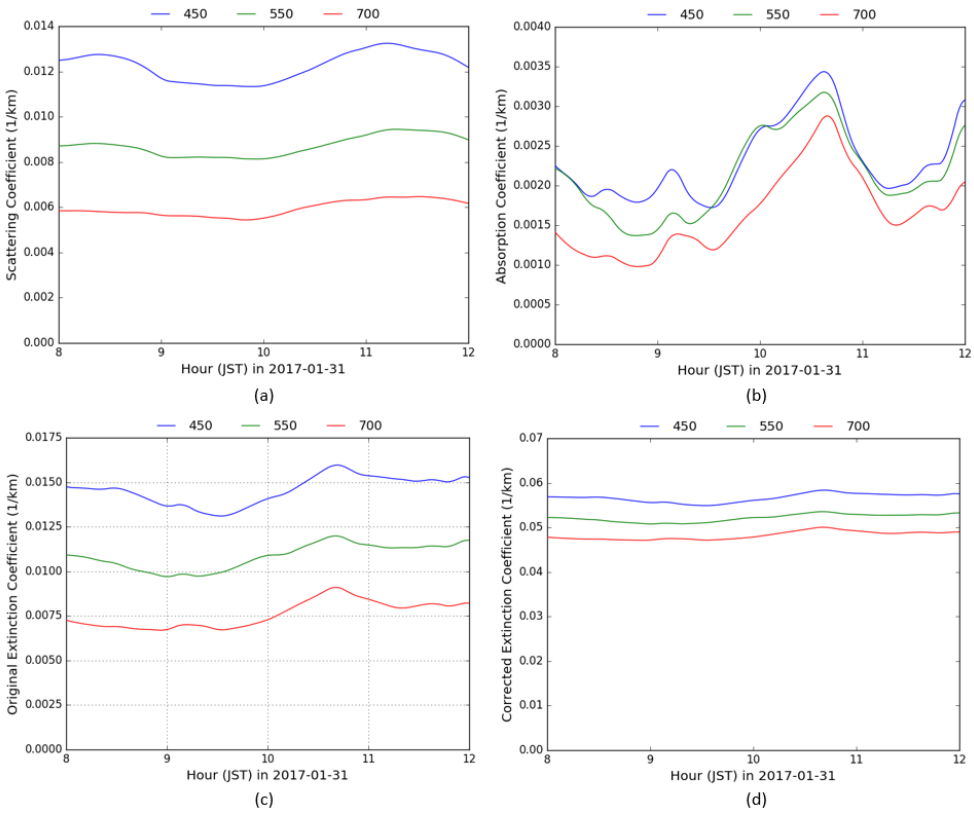

Figure 4.6: Extinction coefficient of sampling instruments in 2017-01-31.

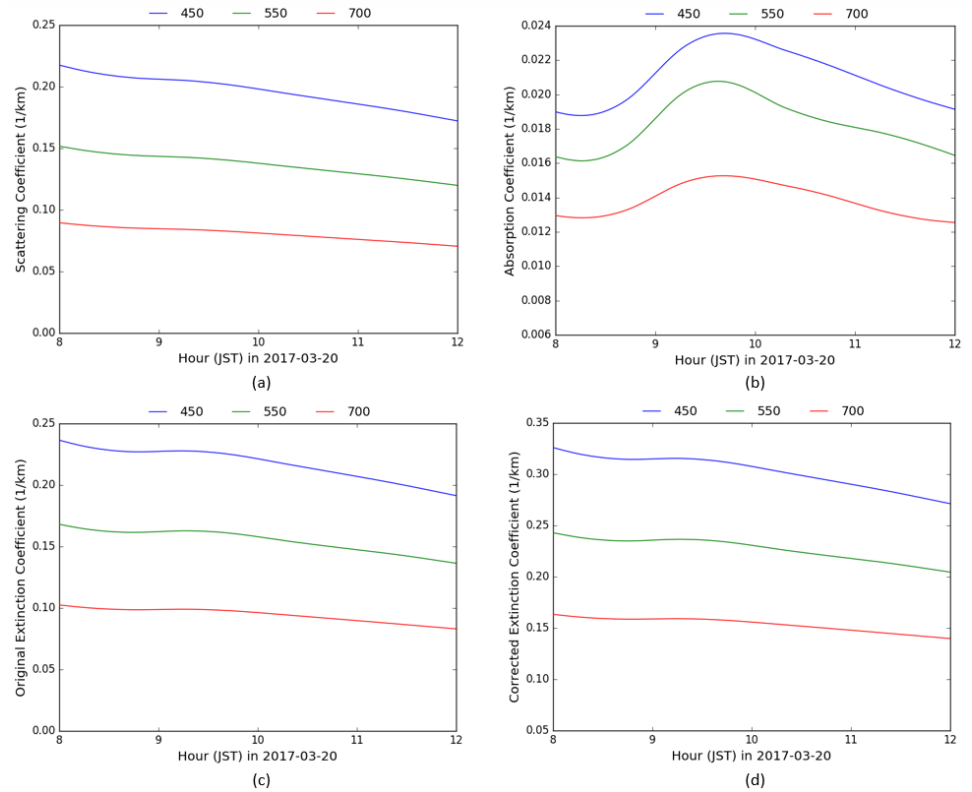

Figure 4.7: Extinction coefficient of sampling instruments in 2017-03-20.

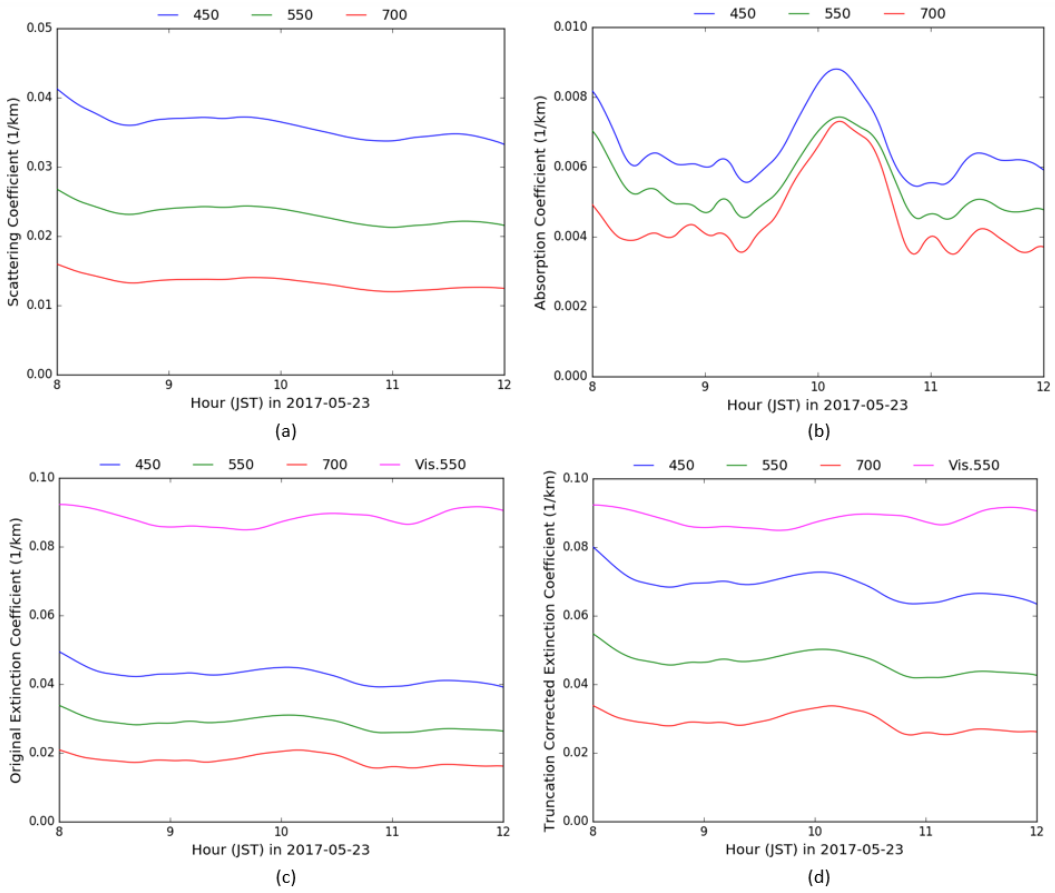

Figure 4.8: Extinction coefficient of sampling instruments in 2017-05-23.

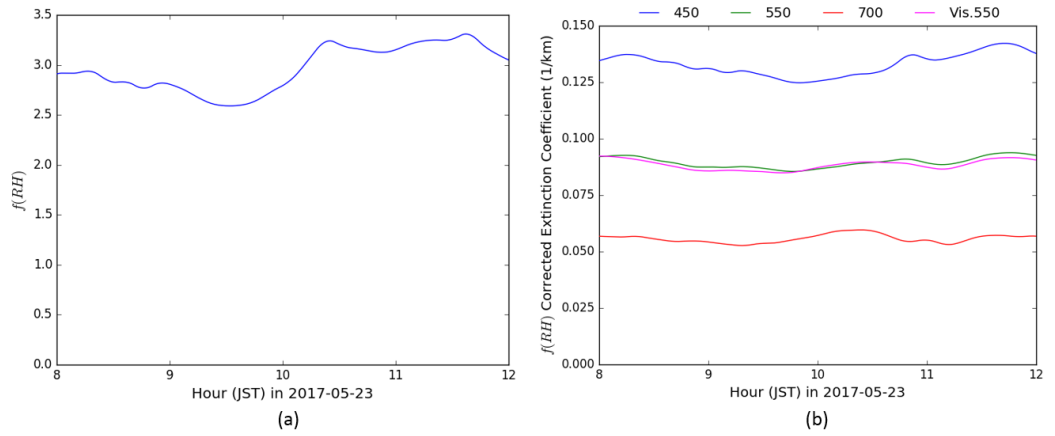

Figure 4.9: The corrected extinction coefficient in 2017-05-23 with *f*(*RH*) correction.

Since the extinction coefficients of sampling instruments are compared to the spatial and temporal distributions of extinction coefficient derived from PPI and SP lidars, respectively, here interpolation procedure is involved. Figures 4.10 to 4.13 present the interpolated extinction coefficient of sampling for fitting the

sampling's wavelengths to the lidar's (349 nm of PPI and 532 nm of SP). The interpolation procedure is implemented to the panel (d) of Figures 4.5 to 4.7 (truncation corrected of extinction coefficient). The corrected extinction coefficient in 2017-05-23 interpolated for comparing to PPI and SP lidars is Figure 4.9 panel (b) with $f(RH)$ correction.

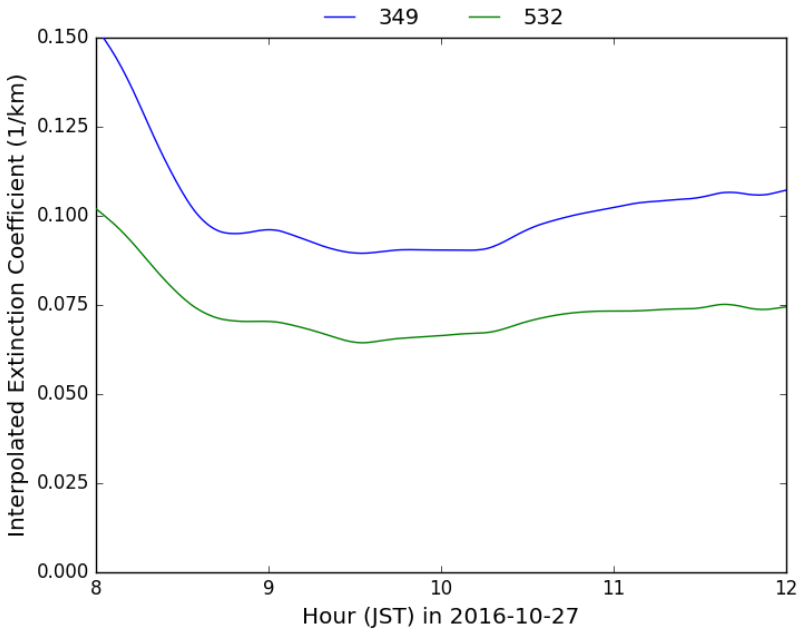

Figure 4.10: Interpolated extinction coefficient in 2016-10-27.

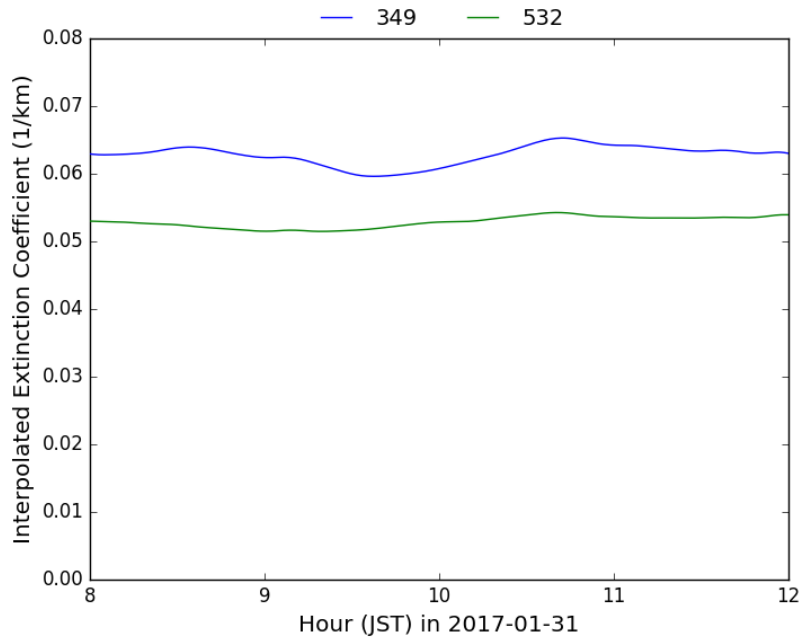

Figure 4.11: Interpolated extinction coefficient in 2017-01-31.

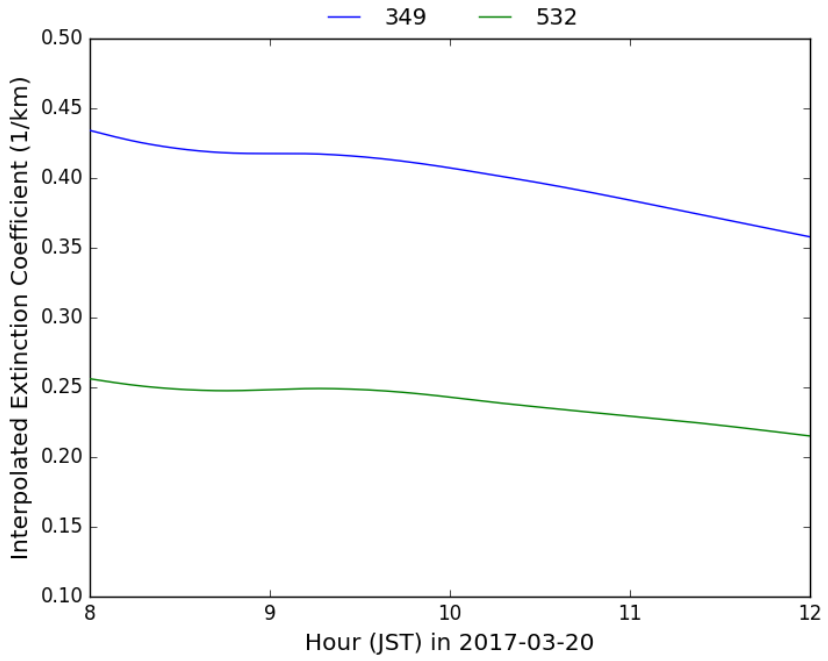

Figure 4.12: Interpolated extinction coefficient in 2017-03-20.

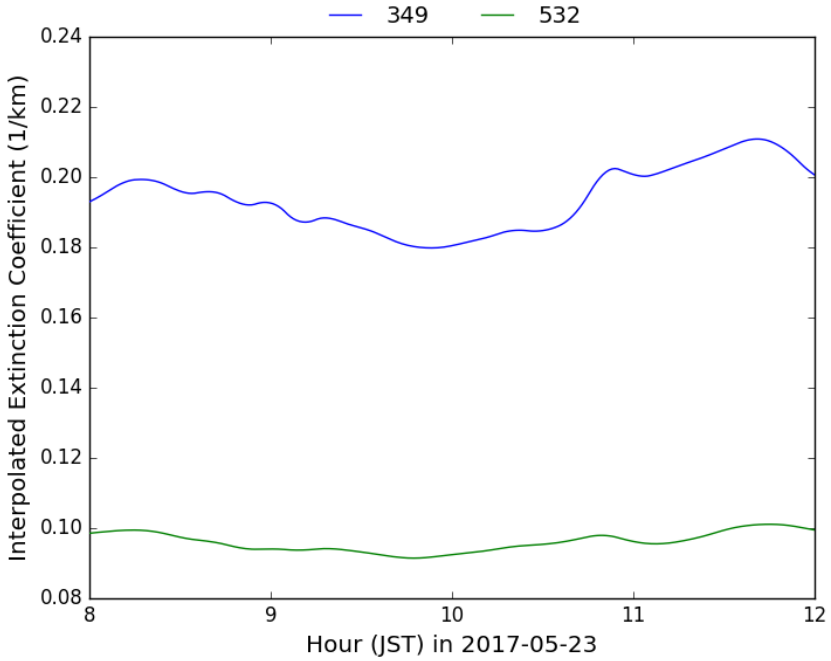

Figure 4.13: Interpolated extinction coefficient in 2017-05-23.

4.1.3 Extinction to Backscattering Ratio

The lidar ratio, the ratio between extinction and backscattering is derived from Mie calculation by employing scattering and backscattering of nephelometer,

absorption of aethalometer, and size distribution of optical particle counter. The Mie scattering calculation and fitting process to the ground sampling instruments are carried out using equations (3-3), (3-4) and (3-5). By means of the calculation and fitting procedure, we obtained the lidar ratio for 349 and 532 nm for calculating extinction coefficient of PPI and SP lidars, respectively. Figure 4.14 to 4.17 show the scheme of Mie scattering calculation for obtaining lidar ratio. Their panels are (a) the size distribution estimated from the OPC data, (b) average of scattering coefficient, (c) mean value of absorption coefficient retrieved from the aethalometer, and (d) single scattering albedo. given as the ratio between the scattering and extinction coefficients. The size distributions in panel (a) are estimated from the OPC data, where mie-1 is the fitting results of modified aerosol and mie-2 is the mono-modal of the lognormal function. The average of scattering and absorption coefficients are obtained from the nephelometer and aethalometer data, respectively. The single scattering albedo is estimated from the ratio between scattering and extinction coefficient of sampling instruments.

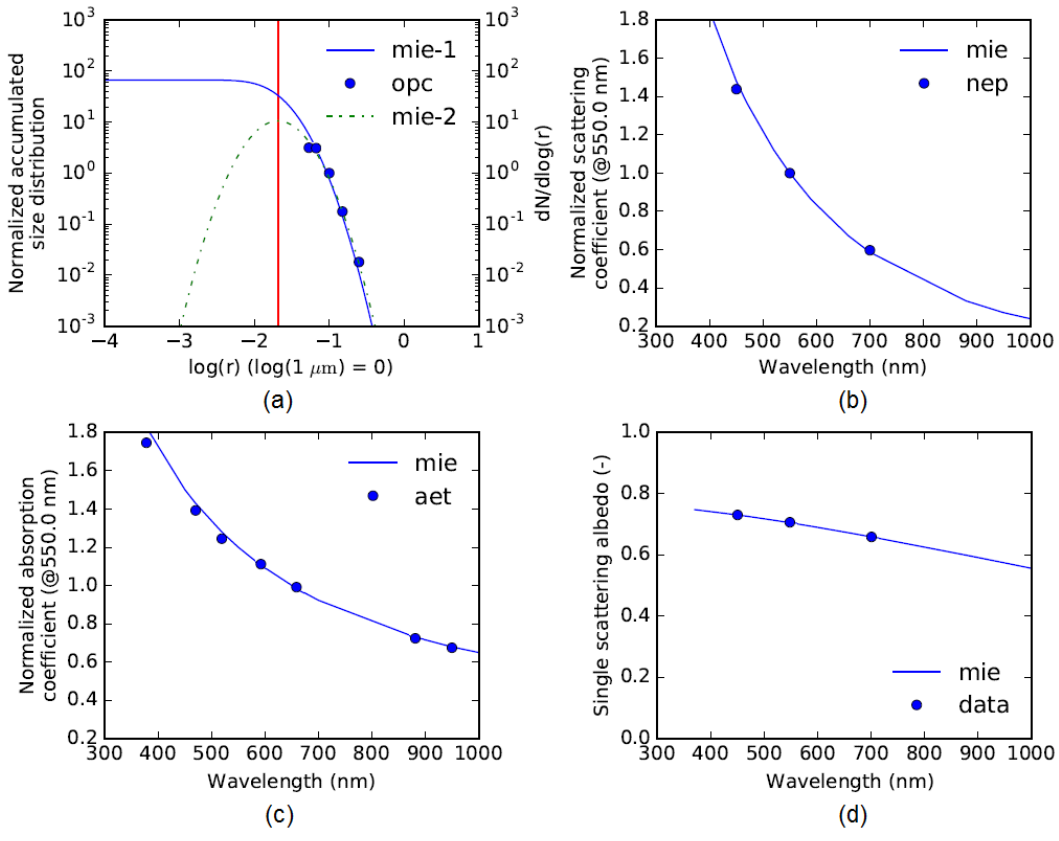

Figure 4.14: Mie scattering calculation in 2016-10-27.

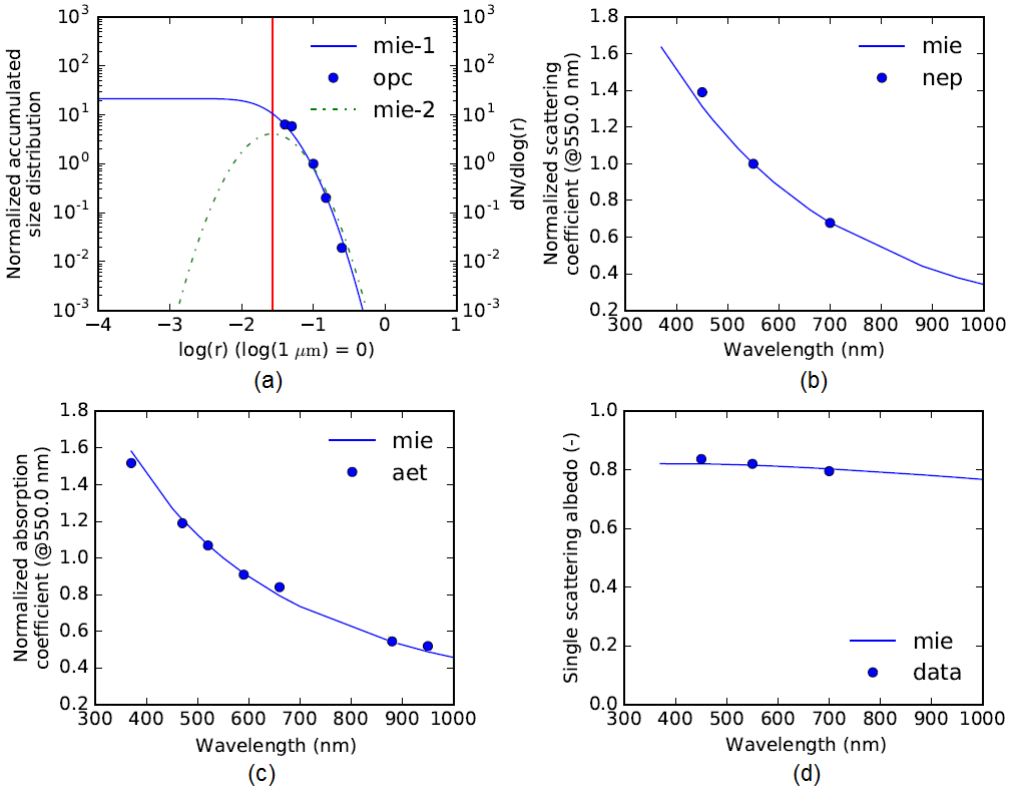

Figure 4.15: Mie scattering calculation in 2017-01-31.

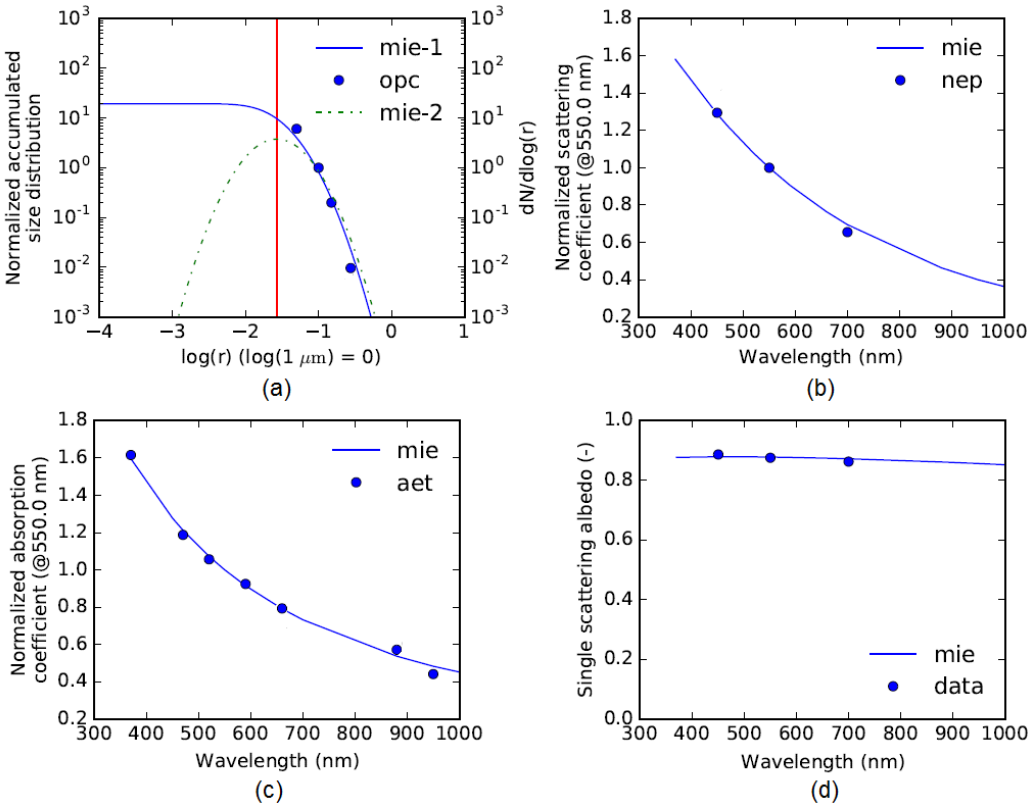

Figure 4.16: Mie scattering calculation in 2017-03-20.

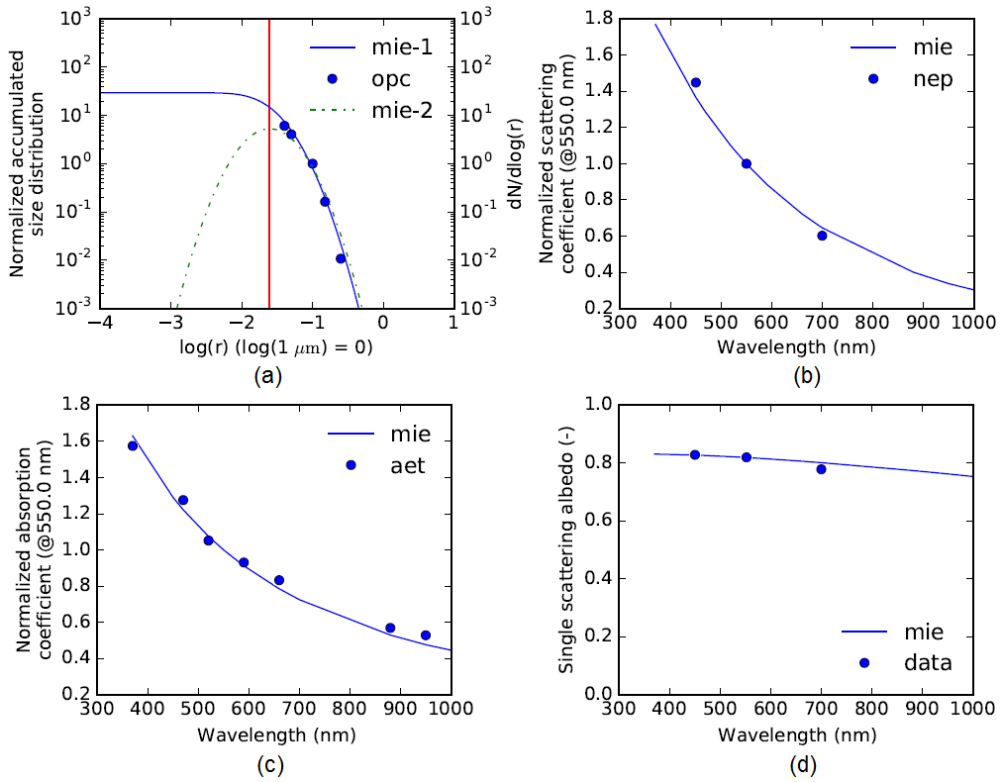

Figure 4.17: Mie scattering calculation in 2017-05-23.

Figures 4.18 to 4.21 are the temporal variation for the two lidar wavelengths of 349 nm (PPI) and 532 nm (SP) which are resulted from the parameters as exemplified in Figure 4.14 to 4.17. The lidar ratios are employed in Fernald analysis for estimating the spatial and temporal distribution of extinction coefficient derived from PPI and SP lidars, respectively.

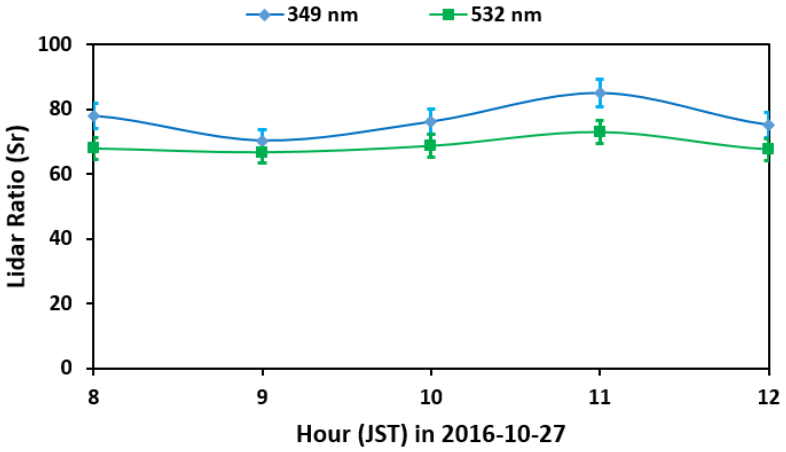

Figure 4.18: Temporal variation of lidar ratio in 2016-10-27.

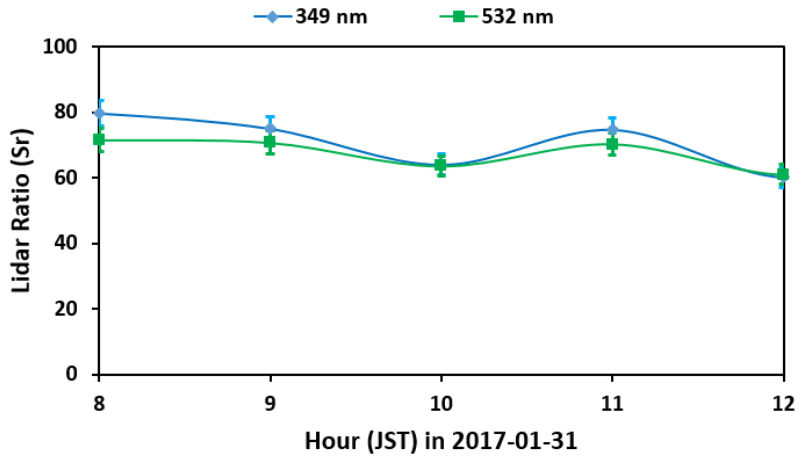

Figure 4.19: Temporal variation of lidar ratio in 2017-01-31.

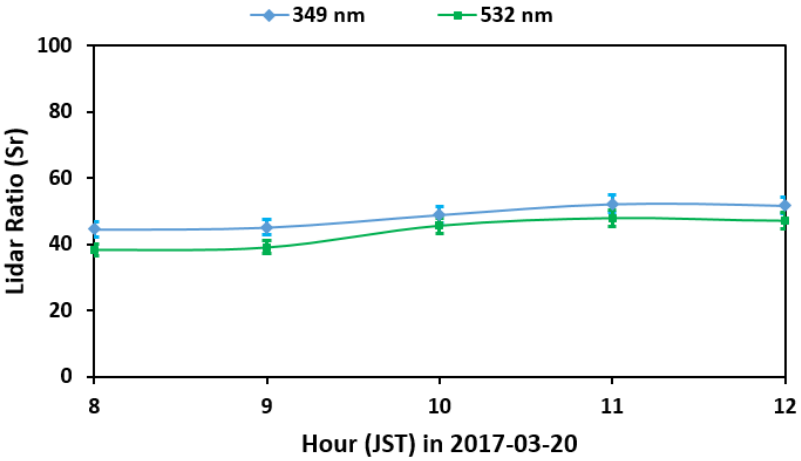

Figure 4.20: Temporal variation of lidar ratio in 2017-03-20.

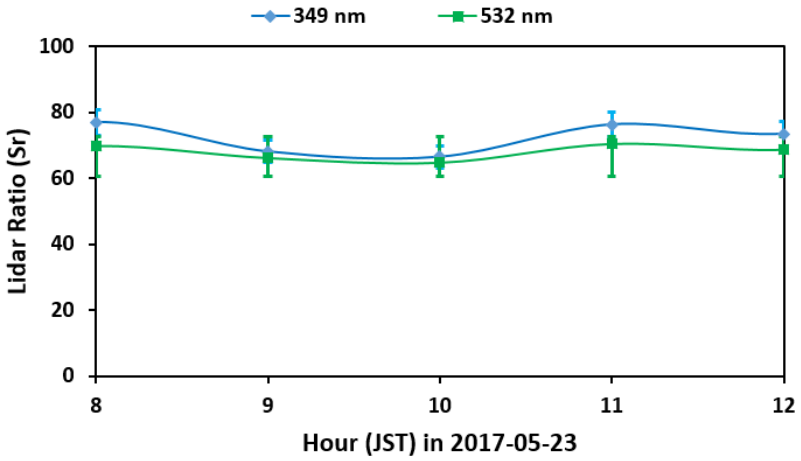

Figure 4.21: Temporal variation of lidar ratio in 2017-05-23.

4.1.4 Extinction Coefficient of Lidars System

Figures 4.22 to 4.25 shows the spatial distribution of aerosol extinction coefficient derived from the PPI lidar measurement which is computed using the Fernald equation (3-6). For the retrieval of extinction coefficient, the hourly values of lidar ratio for 349 nm have been employed. The 360 degrees of aerosol extinction distributions is recorded as long as ~30 minutes from around 10.00 to 10.30 o'clock with elevation from the center of rotation ~4 degrees. Since the spatial distributions of extinction coefficient are observed in the range of blue-band measurement, the results are compared with the AOT of Landsat-8 and Himawari-8 satellites in the same range of wavelength.

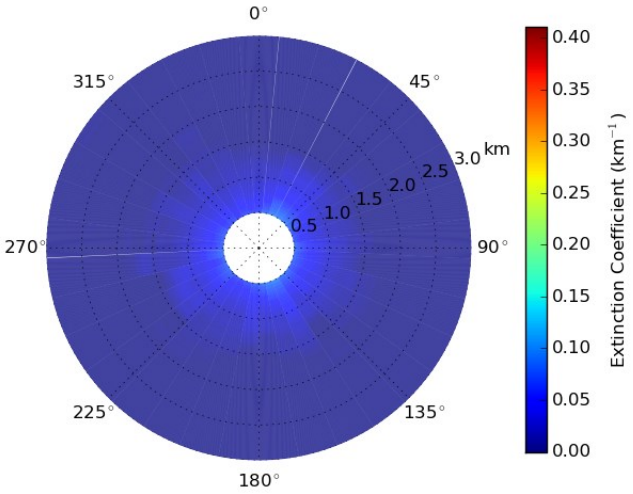

Figure 4.22: Spatial distribution of extinction coefficient in 2016-10-27.

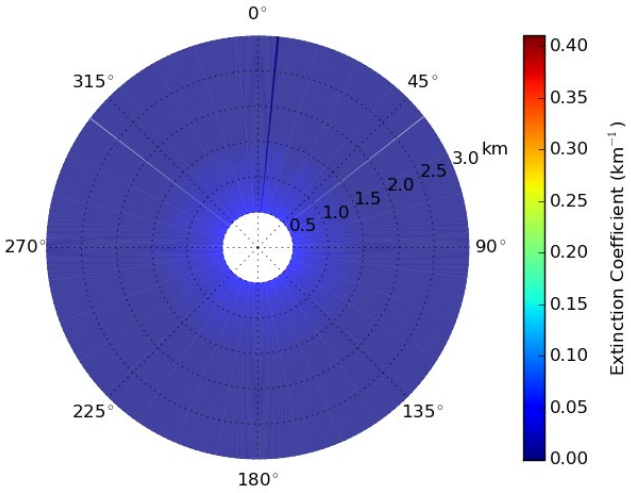

Figure 4.23: Spatial distribution of extinction coefficient in 2017-01-31.

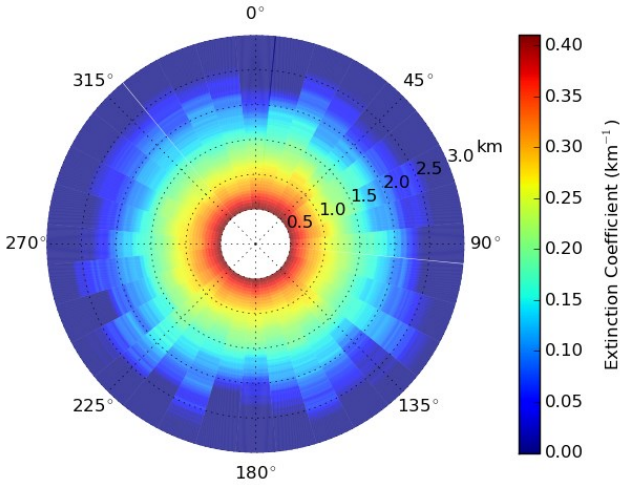

Figure 4.24: Spatial distribution of extinction coefficient in 2017-03-20.

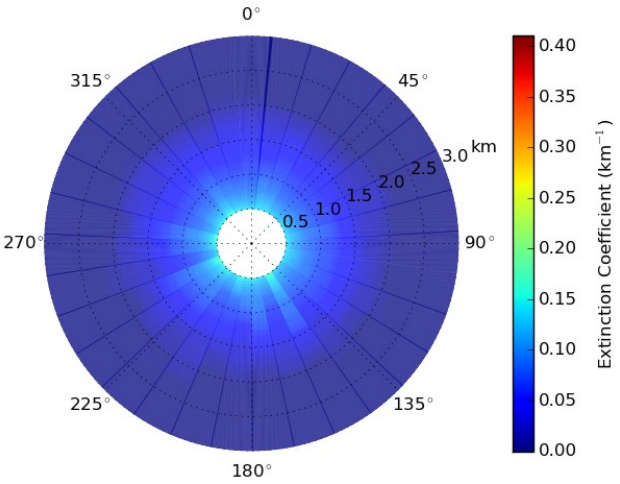

Figure 4.25: Spatial distribution of extinction coefficient in 2017-05-23.

Figures 4.26 to 4.29 show the time-height indicator representations obtained from the (a) SP and (b) NIES lidar observations. For analyzing the NIES lidar data at 532 nm, the pertinent value of lidar ratio has been estimated with the Mie calculation based on sampling data. Although the SP lidar observes the north direction with the elevation angle of 30º, the resulting behavior of aerosol extinction is similar to that observed with the vertically looking NIES lidar, which is located at the surface level around 300 m in the north direction from the SP lidar. By means the same assumption of PPI lidar, the results of both SP and NIES lidars observation are compared to the green band of Landsat-8 and Himawari-8 satellites.

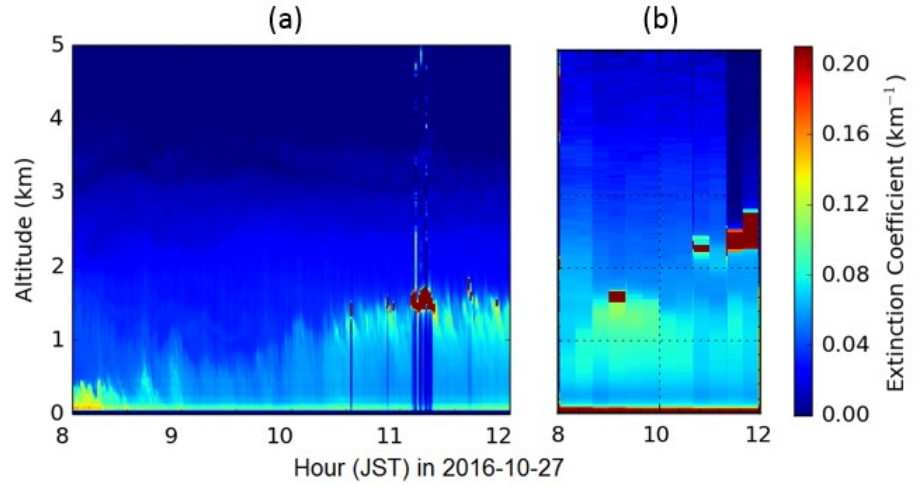

Figure 4.26: Temporal distribution of extinction coefficient in 2016-10-27.

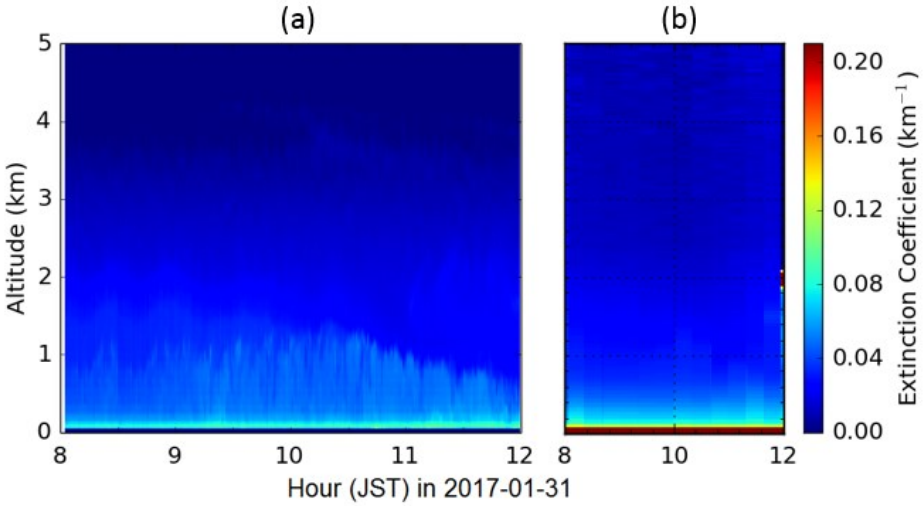

Figure 4.27: Temporal distribution of extinction coefficient in 2017-01-31.

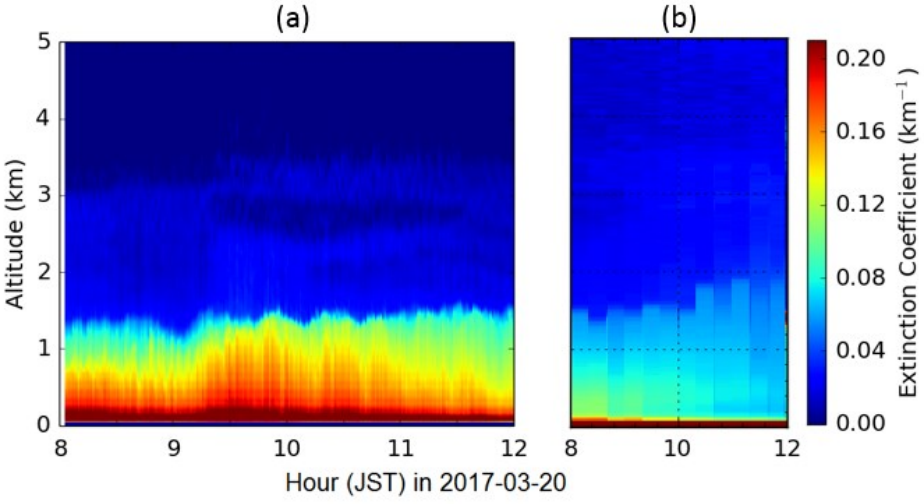

Figure 4.28: Temporal distribution of extinction coefficient in 2017-03-20.

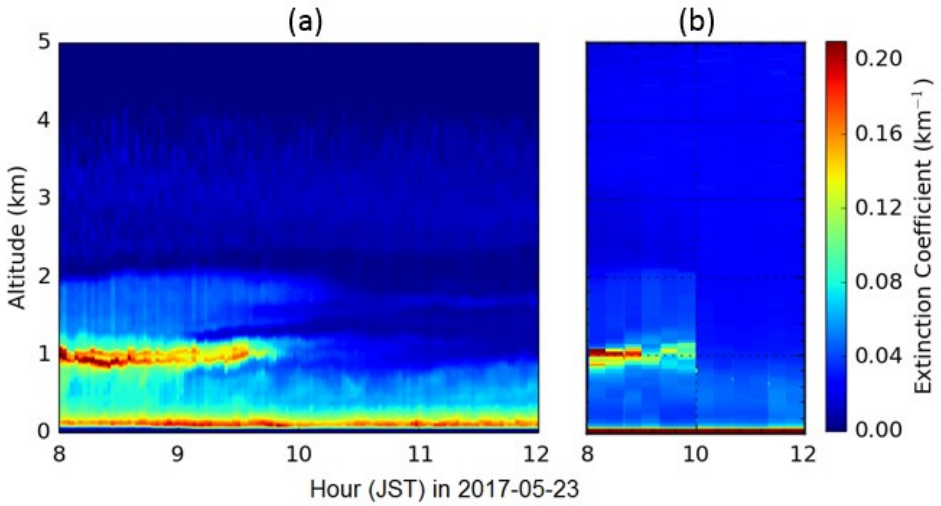

Figure 4.29: Temporal distribution of extinction coefficient in 2017-05-23.

4.1.5 AOT of Sunphotometer and Skyradiometer

The values of AOT represented in Figures 4.30 to 4.33 are retrieved from sunphotometer processing data and independent measurement of skyradiometer which are plotted in panels (a) and (b), respectively. The AOT in all of the panel (a) is estimated using equation (3-7) every ~10 seconds while in panel (b) is plotted directly from skyradiometer data every ~10 minutes. The wavelength employed in this plotting are blue (368 and 380 nm), green (500 nm), and red (675 nm) channels. Here, the different of the three wavelengths between sunphotometer and skyradiometer is only for the green band.

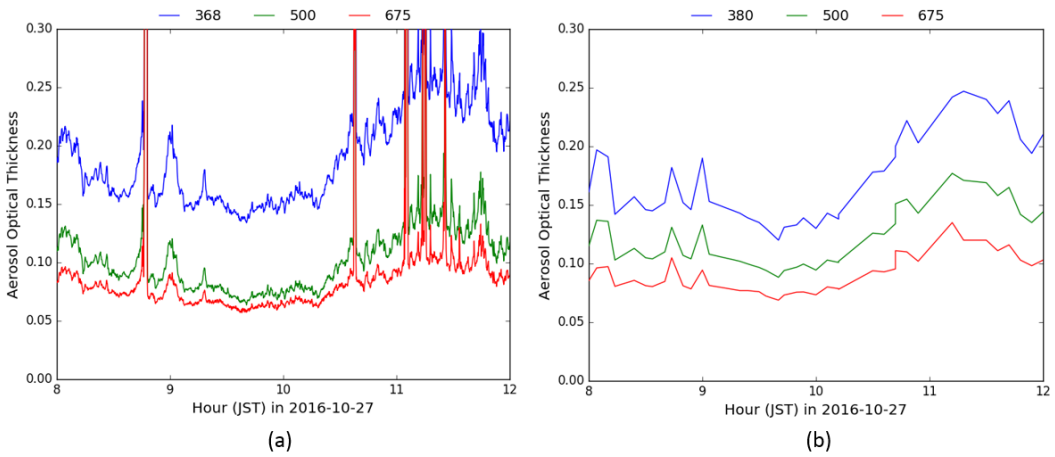

Figure 4.30: The temporal change of AOT in 2016-10-27.

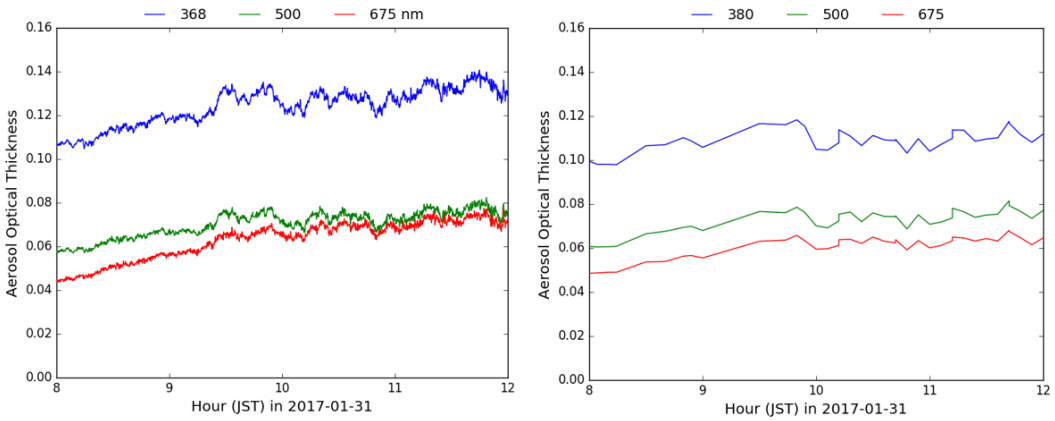

Figure 4.31: The temporal change of AOT in 2017-01-31.

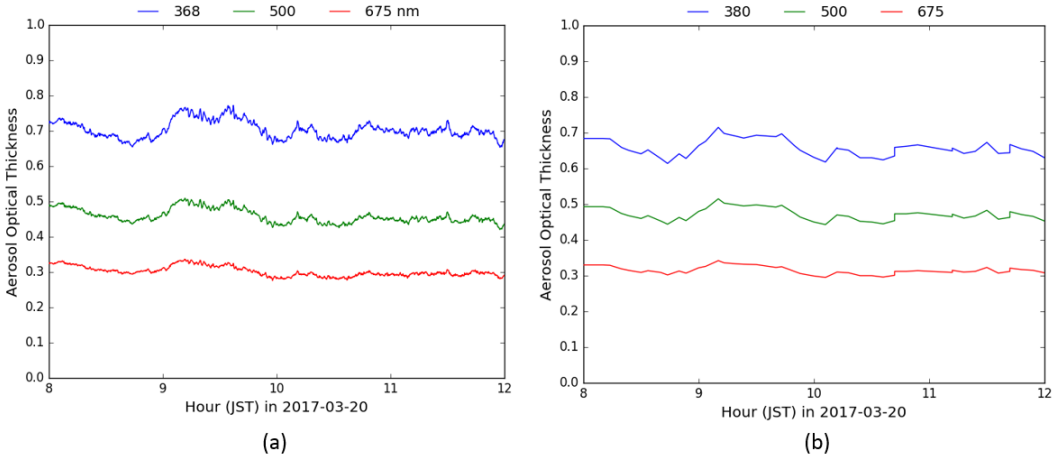

Figure 4.32: The temporal change of AOT in 2017-03-20.

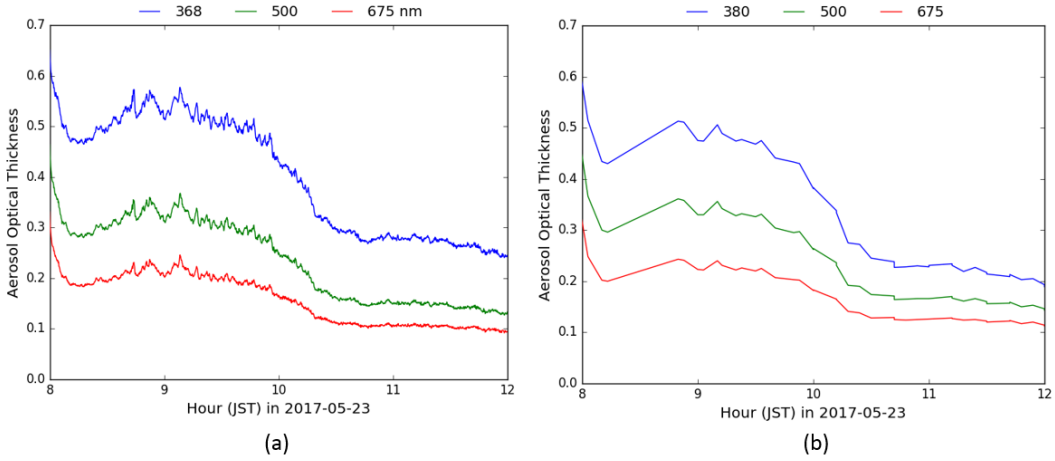

Figure 4.33: The temporal change of AOT in 2017-05-23.

Furthermore, the AOT values derived from both sunphotometer and skyradiometer in Figures 4.30 to 4.33 are interpolated to the wavelength of visible band of Landsat-8 and Himawari-8. Figures 4.34 to 4.37 show the interpolated of AOT of sunphotometer based on a blue and green band of the two satellites. Panels (a) are the result of Landsat-8 estimation, together with interpolation value of Himawari-8 in panel (b). By means, the same interpolation procedure, in Figures 4.38 to 4.41 are figured out AOT of skyradiometer.

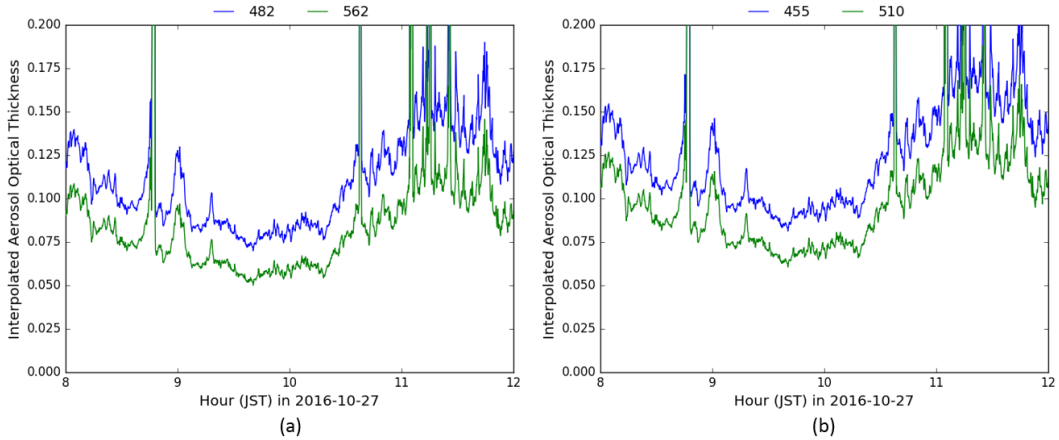

Figure 4.34: Interpolated AOT of sunphotometer in 2016-10-27.

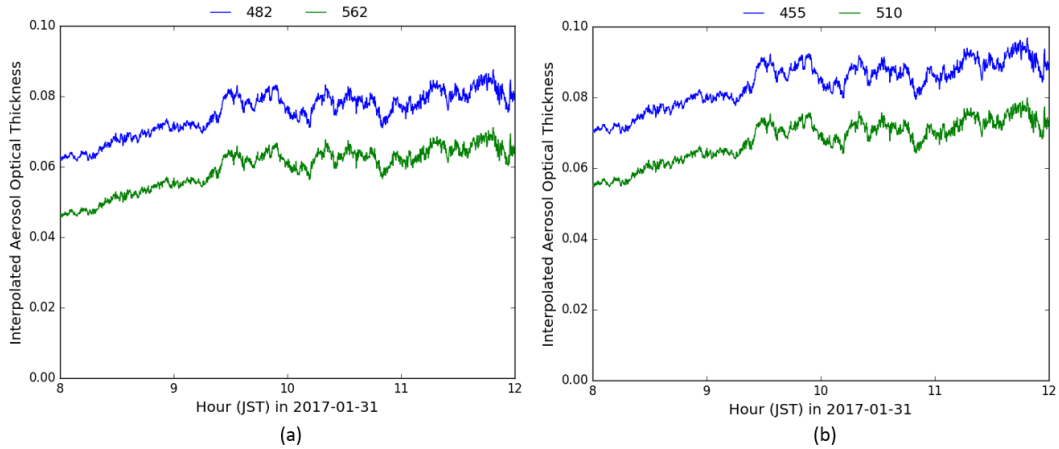

Figure 4.35: Interpolated AOT of sunphotometer in 2017-01-31.

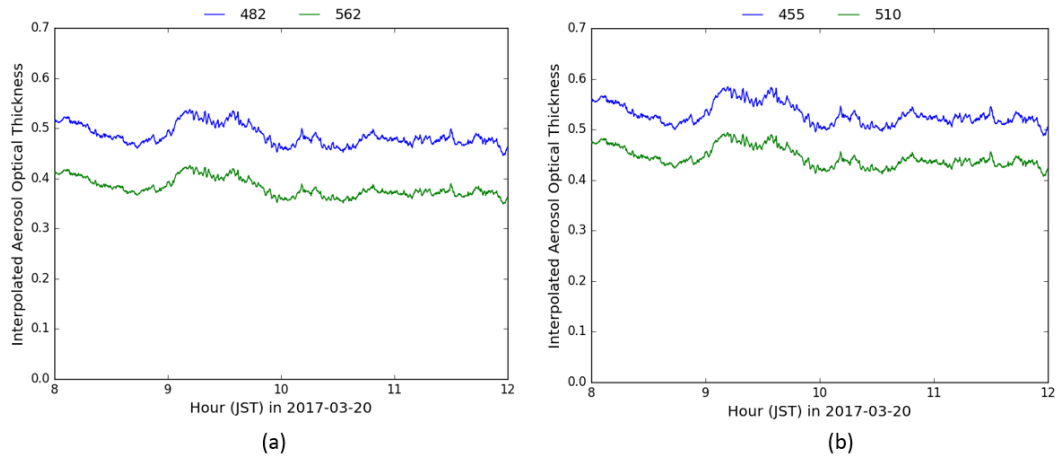

Figure 4.36: Interpolated AOT of sunphotometer in 2017-03-20.

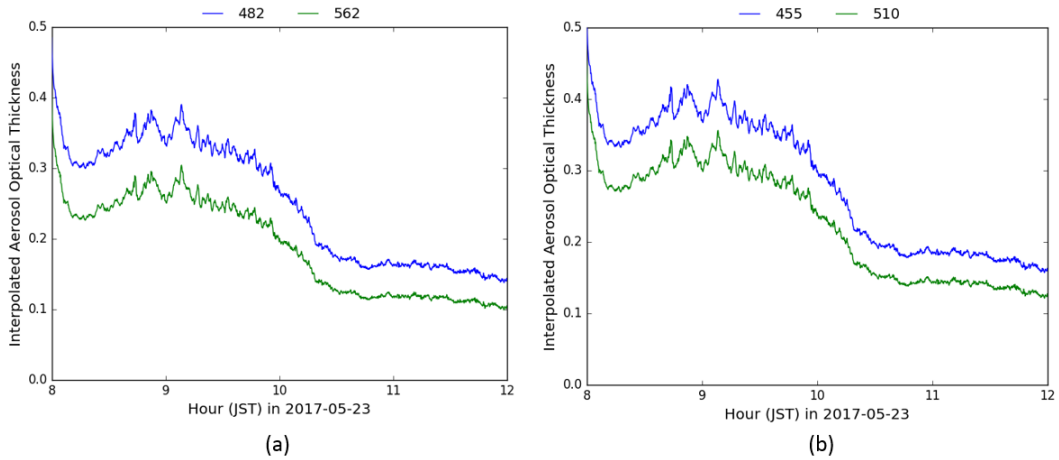

Figure 4.37: Interpolated AOT of sunphotometer in 2017-05-23.

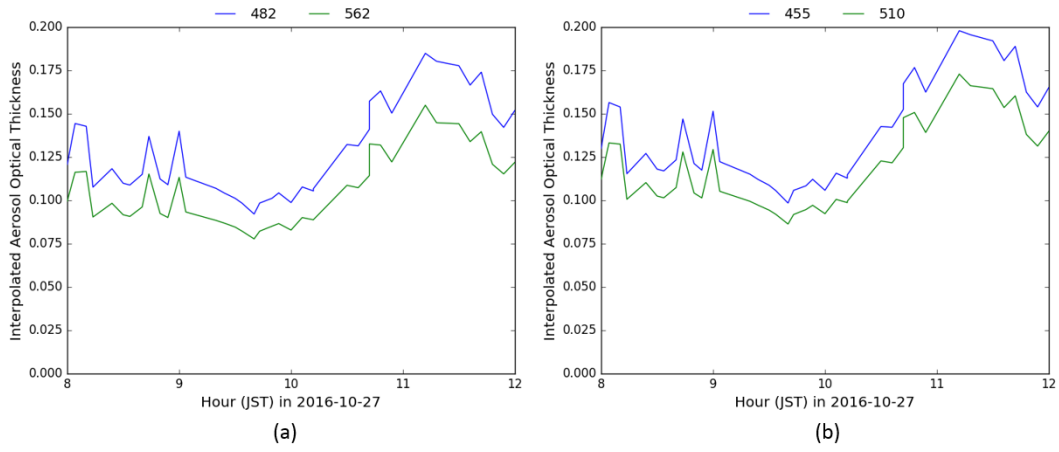

Figure 4.38: Interpolated AOT of skyradiometer in 2016-10-27.

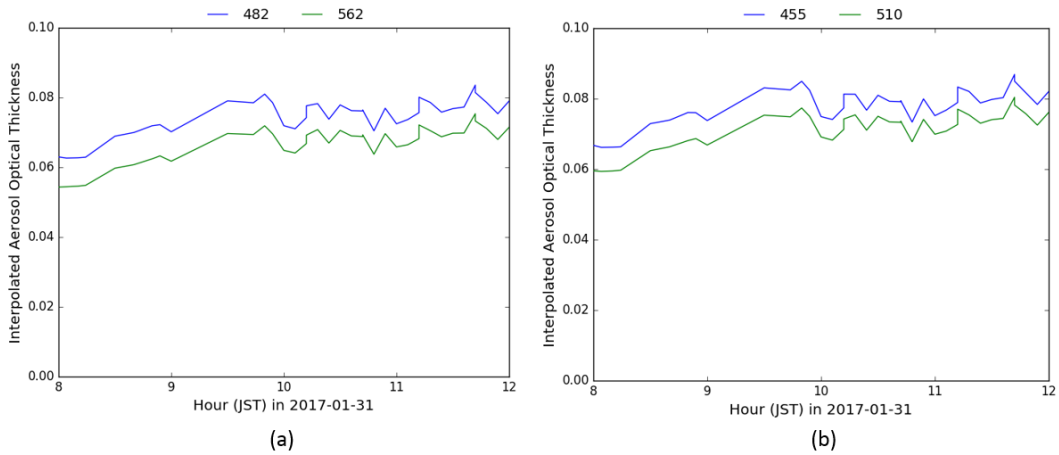

Figure 4.39: Interpolated AOT of skyradiometer in 2017-01-31.

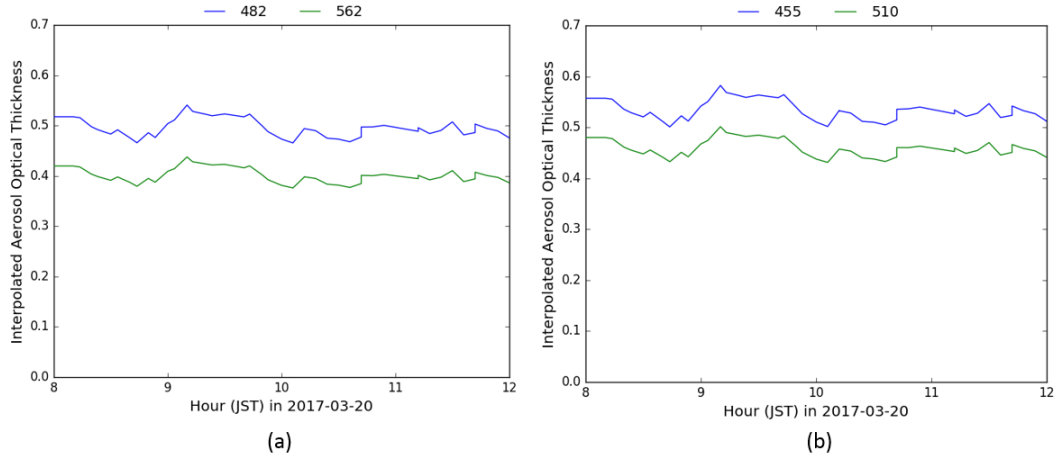

Figure 4.40: Interpolated AOT of skyradiometer in 2017-03-20.

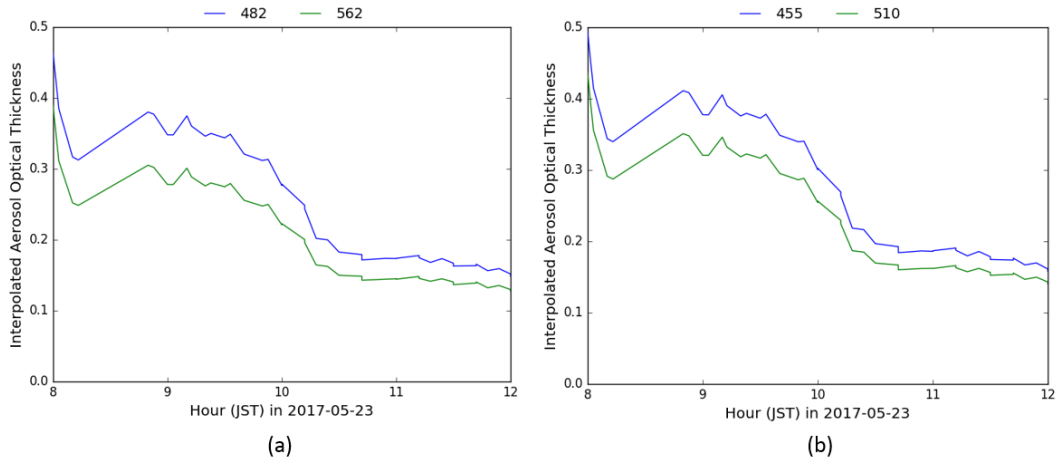

Figure 4.41: Interpolated AOT of skyradiometer in 2017-05-23.

4.1.6 Ångström Exponent

Ångström exponent is the physical parameter of aerosol related to the information of aerosol size distribution. In this study, we determine the Ångström exponent from the wavelength dependence of AOT (aerosol optical thickness) and AEC (aerosol extinction coefficient) that can be estimated using equation (3-8). The value of Ångström exponent is the order of unity. In the case of the dominance of fine-mode aerosol floating in atmosphere, the value of Ångström exponent becomes larger, while it becomes smaller for the dominance of coarse-mode particles.

Figures 4.42 to 4.45 display the Ångström exponent derived from estimation and independent measurements which are plotting in panels (a) and (b), respectively. In panels (a), the values of Angtrom exponent are derived from both AEC of sampling and AOT of sunphotometer; then the corrected AE mean the Ångström exponents which are corrected using truncation correction based in Figure 3.30.

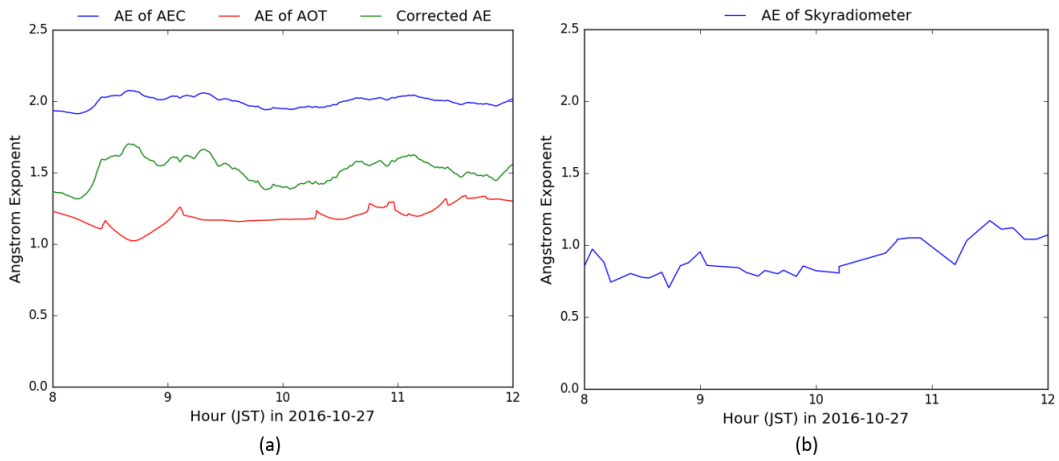

Figure 4.42: The temporal variability of Ångström exponent in 2016-10-27.

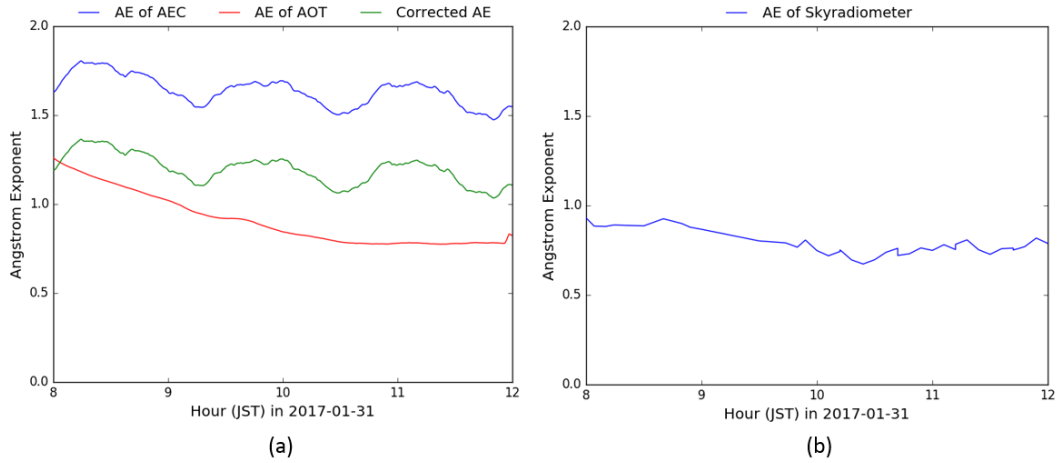

Figure 4.43: The temporal variability of Ångström exponent in 2017-01-31.

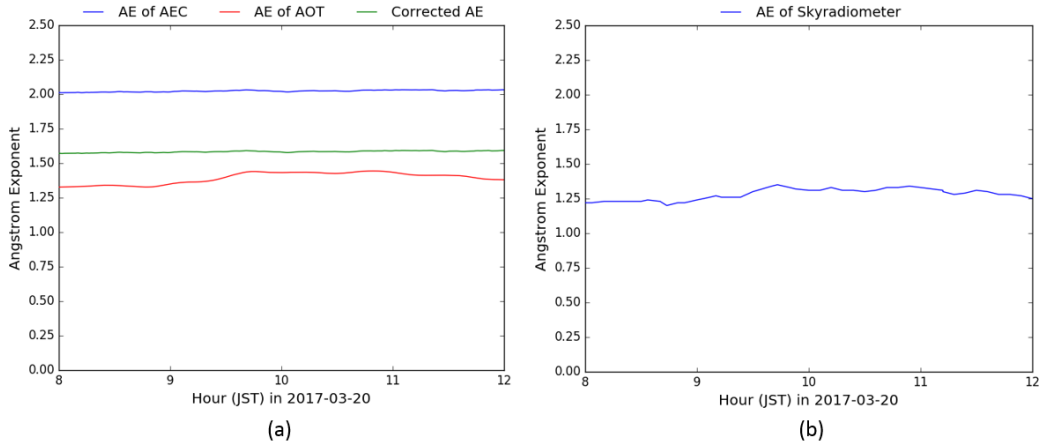

Figure 4.44: The temporal variability of Ångström exponent in 2017-03-20.

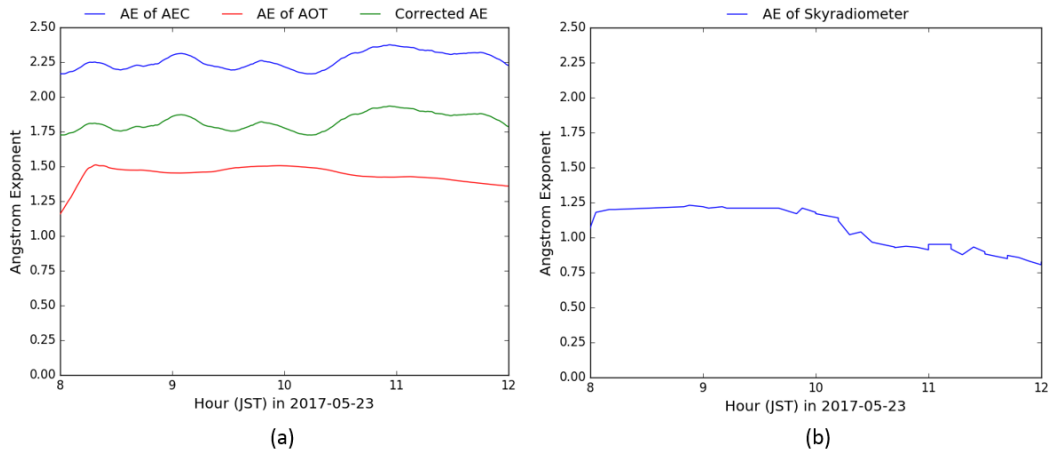

Figure 4.45: The temporal variability of Ångström exponent in 2017-05-23.

4.1.7 Apparent Reflectance

The apparent reflectance showed in this sub-section are derived from the visible band (blue and green) Landsat-8 and Himawari-8 satellites using equations (3-9) and (3-10), respectively. The presentation of apparent reflectance for both satellites in Figures 4.46 to 4.57 is displayed in panel (a) for blue band and panel (b) for the green band. The figures are shown in three packets with the turn Himawari-8 before Landsat-8 overpass (~10.10 am), Landsat-8 overpass (~10.15 am), and Himawari-8 after Landsat-8 overpass (~10.20 am) with Japan Standard Time (JST). The center wavelengths of both satellites employed in this study are close to the wavelength of PPI and SP lidars as blue and green bands, respectively. For the Landsat-8, we involve channels 2 (482 nm) and 3 (562 nm) while the Himawari-8 we used channels 1 (455 nm) and 2 (510 nm).

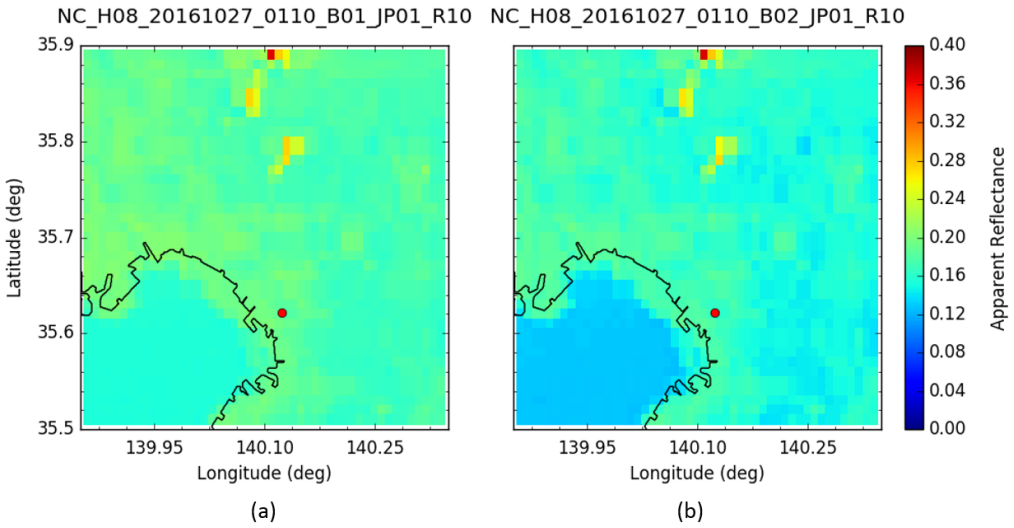

Figure 4.46: Apparent reflectance of Himawari-8 before overpass in 2016-10-27.

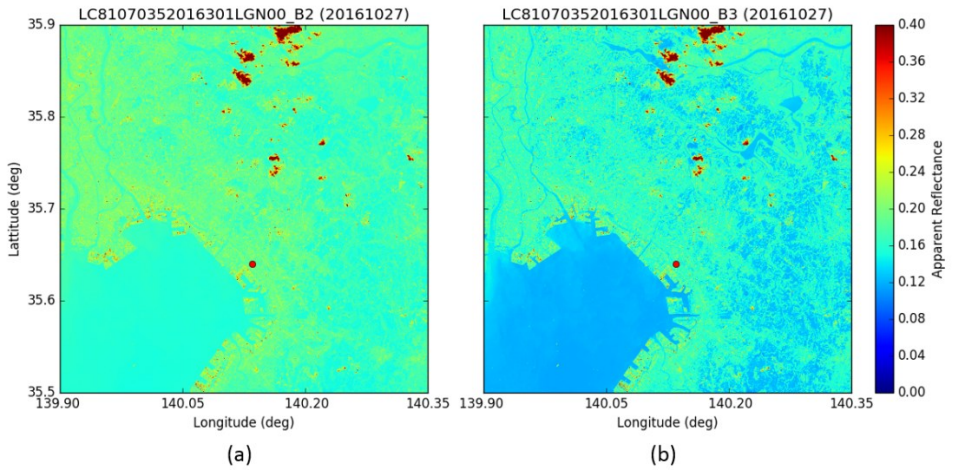

Figure 4.47: Apparent reflectance of Landsat-8 in 2016-10-27.

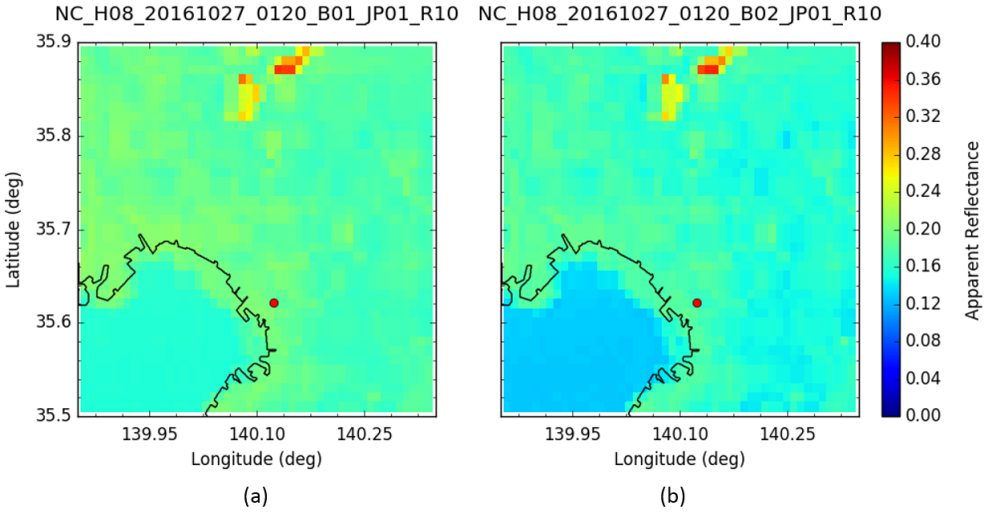

Figure 4.48: Apparent reflectance of Himawari-8 after overpass in 2016-10-27.

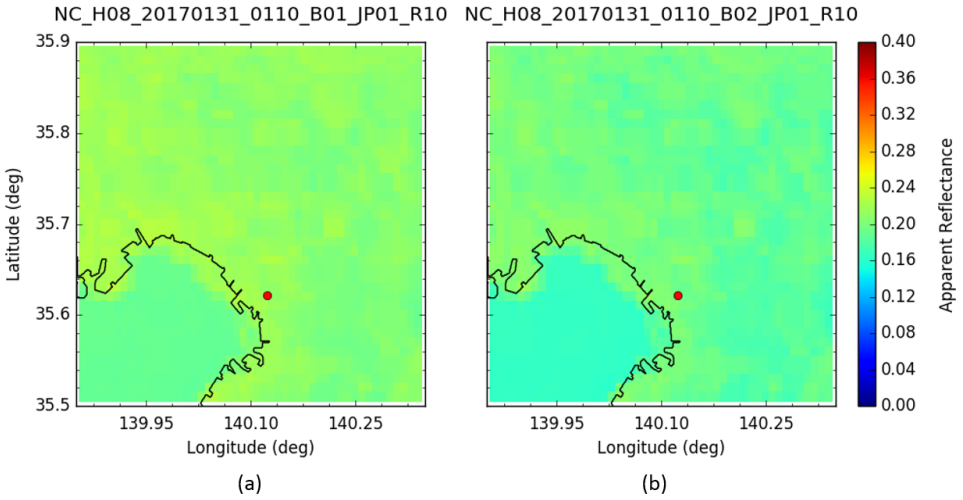

Figure 4.49: Apparent reflectance of Himawari-8 before overpass in 2017-01-31.

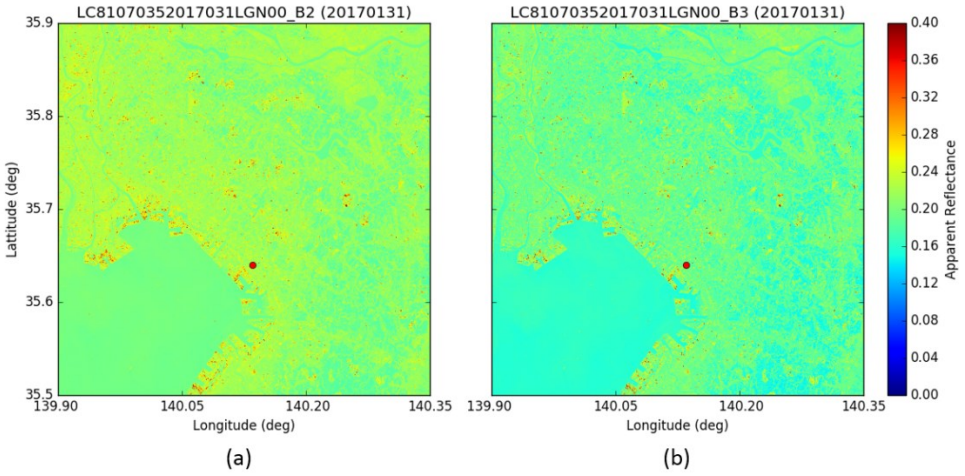

Figure 4.50: Apparent reflectance of Landsat-8 in 2017-01-31.

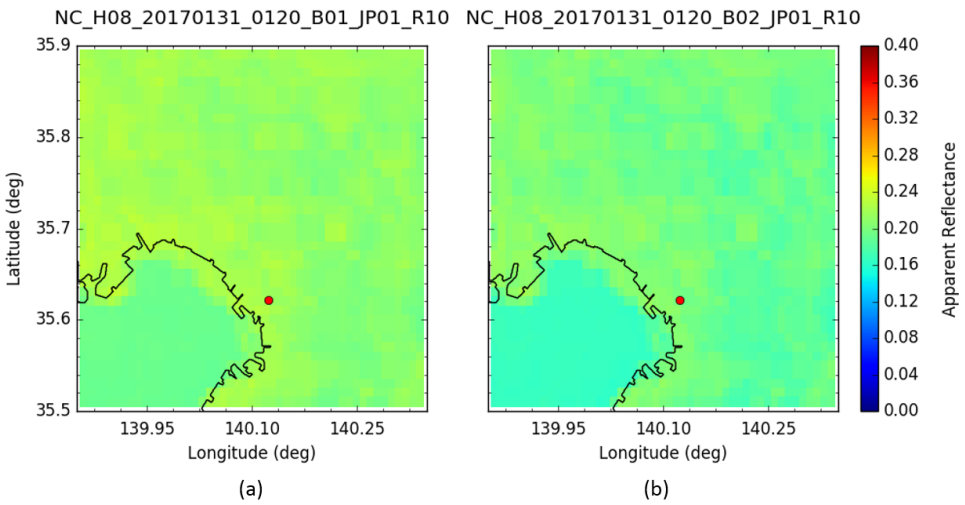

Figure 4.51: Apparent reflectance of Himawari-8 after overpass in 2017-01-31.

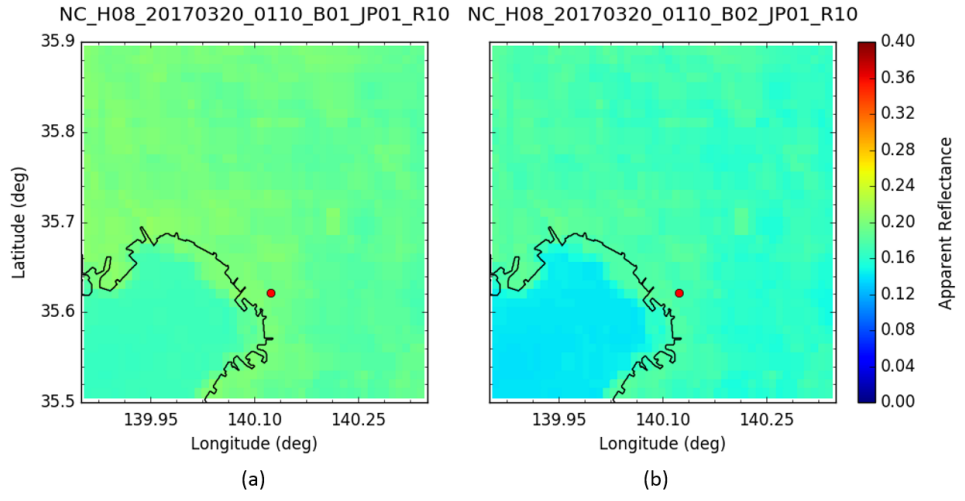

Figure 4.52: Apparent reflectance of Himawari-8 before overpass in 2017-03-20.

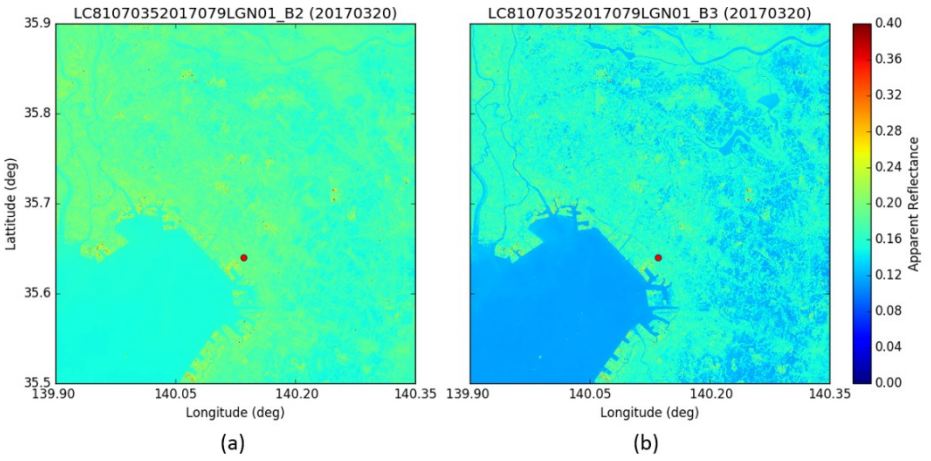

Figure 4.53: Apparent reflectance of Landsat-8 in 2017-03-20.

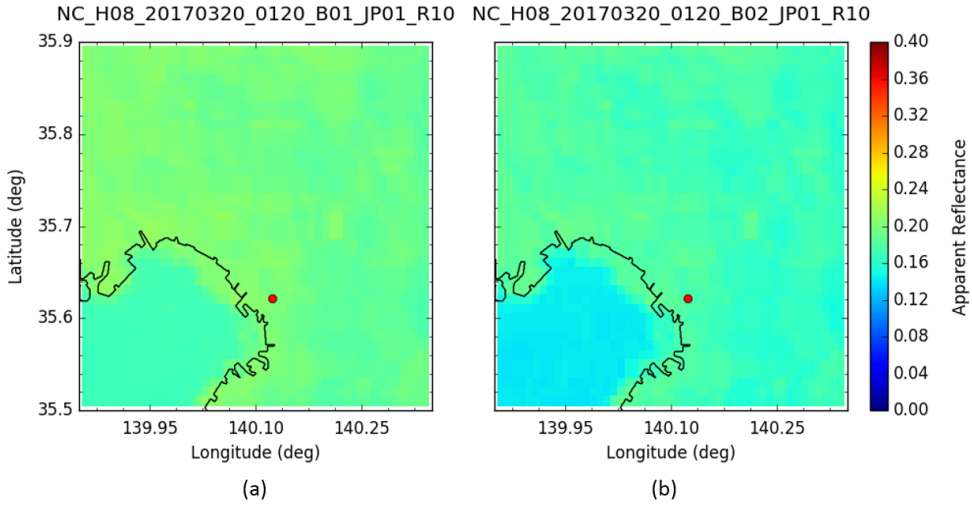

Figure 4.54: Apparent reflectance of Himawari-8 after overpass in 2017-03-20.

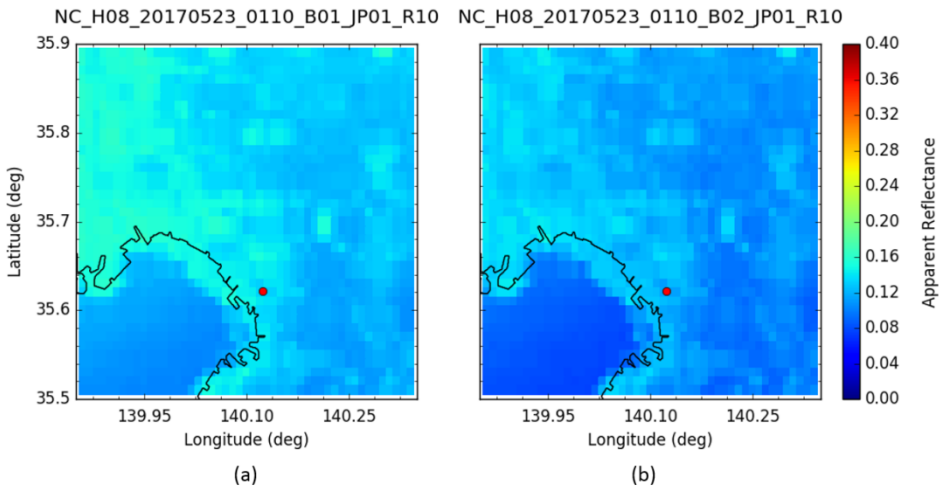

Figure 4.55: Apparent reflectance of Himawari-8 before overpass in 2017-05-23.

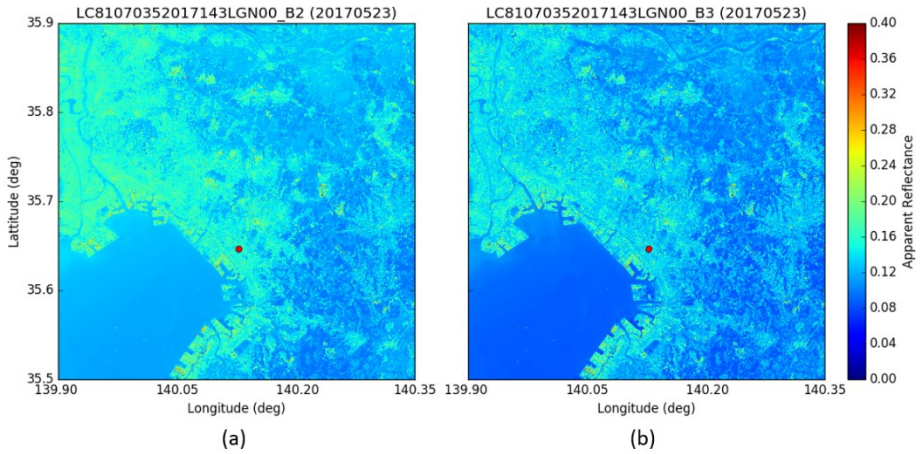

Figure 4.56: Apparent reflectance of Landsat-8 in 2017-05-23.

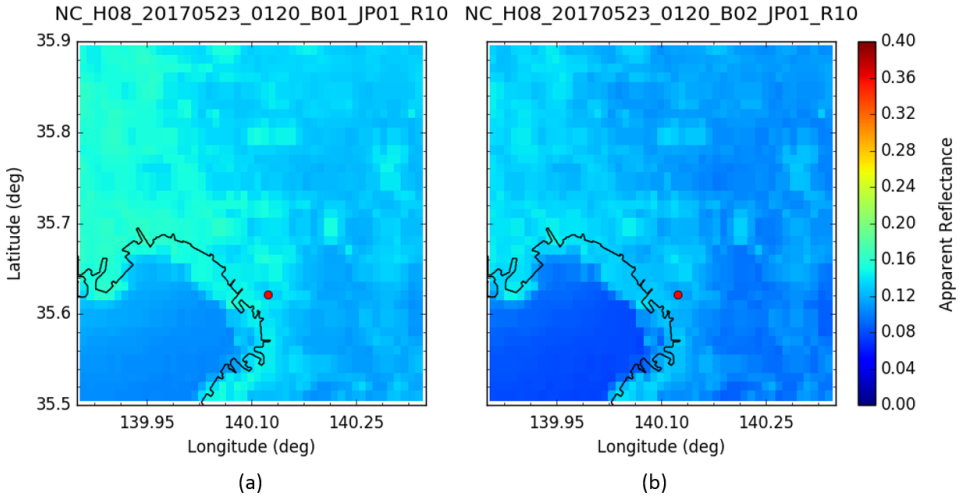

Figure 4.57: Apparent reflectance of Himawari-8 after overpass in 2017-05-23.

4.1.8 Observed Radiance

By means of apparent reflectance, an observed radiance can be estimated in MODTRAN code. The significant of radiance in this study is a parameter to determine surface reflectance based on apparent reflectance and AOT. Besides, together with original aerosol parameters retrieved from Mie scattering calculation which are summarized in Table 4.1, together with Table 4.2 as the resume of interpolated AOT values of ground measurements (sunphotometer and skyradiometer) at the same time of both satellites (Landsat-8 and Himawari-8) record image. Both zenith and azimuth angles of Landsat-8 satellite are 0.001° and

181.29º, respectively which are constant for every overpass time. Beside, the solar zenith angle (SZA) and solar azimuth angle (SAA) dependent to the solar position. The angles data are provided in the metadata of Landsat-8 satellites. On the other hand, the satellite zenith and azimuth angles of Himawari-8 are estimated using equations (3-11), (3-12), and (3-13) with values approximately 35.94º and 178.39º. Furthermore, the atmospheric models choiched for Chiba area are selected based on the season in mid-latitudes. The others important parameters for describing aerosol type are density (N) with the unity (1) value, mode radius (r), width ($\log \sigma$), refractive index (real and imaginary parts as *Re* and *Im*, respectively. All parameter for representing the aerosol type are obtained from the Mie scattering calculation (Figures 4.14 to 4.17). The presentation of observed radiance for both satellites in Figures 4.58 to 4.61 is displayed based on Himawari-8 before Landsat-8 overpass (H8-BOP) time at ~11.10 JST, Landsat overpass (L8-OP) time at ~10.15 JST, and Himawari-8 after Landsat-8 overpass (H8-AOP) time ~11.20 JST.

Table 4.1: Atmospheric model and aerosol type as input parameter for MODTRAN computation for calculating radiative transfer of Landsat-8 and Himawari-8 images over the Kanto area. The τ_{550} refers to the value of AOT at 550 nm interpolated from sunphotometer and skyradiometer.

Date	DOY	τ_{550}	Atm. Model	Aerosol Type			
				r (μm)	$\log\sigma$	*Re*	*Im*
27 Oct. 2016	301	0.067	Mid Lat. Summer	0.0206	0.3017	1.5848	0.0558
31 Jan. 2017	31	0.063	Mid Lat. Winter	0.0266	0.3242	1.6000	0.0373
20 Mar. 2017	79	0.372	Mid Lat. Winter	0.0268	0.3323	1.5926	0.0231
23 May 2017	143	0.193	Mid Lat. Summer	0.0246	0.3165	1.5867	0.0351

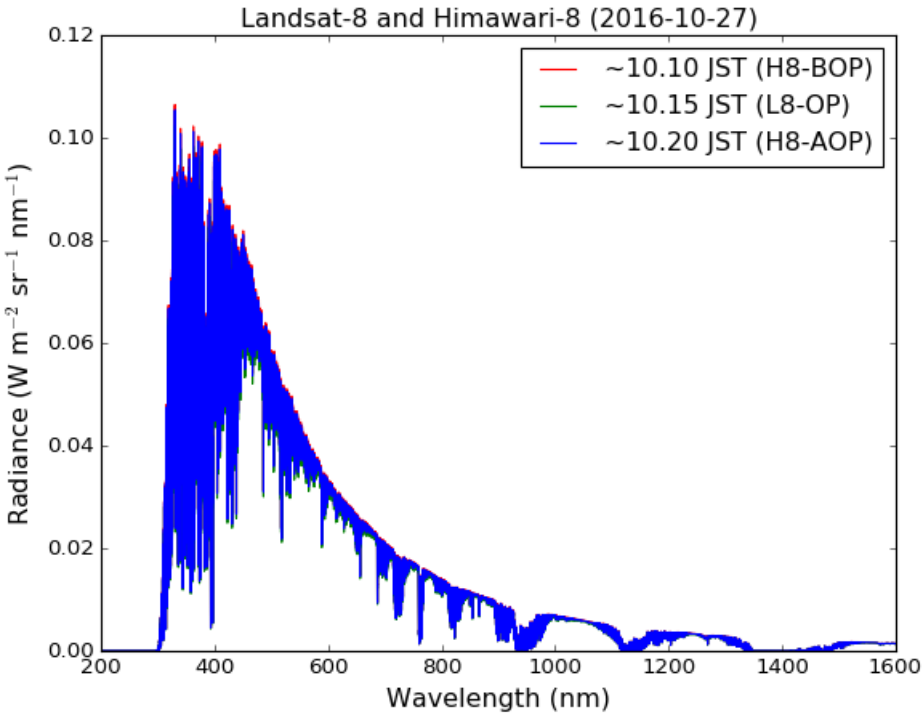

Figure 4.58: Radiance in 2016-10-27 with H8-BOP (SZA=51.49 and SAA=156.90), L8-OP (SZA=51.42 and SAA=158.88), and H8-AOP (SZA=50.74 and SAA=159.88).

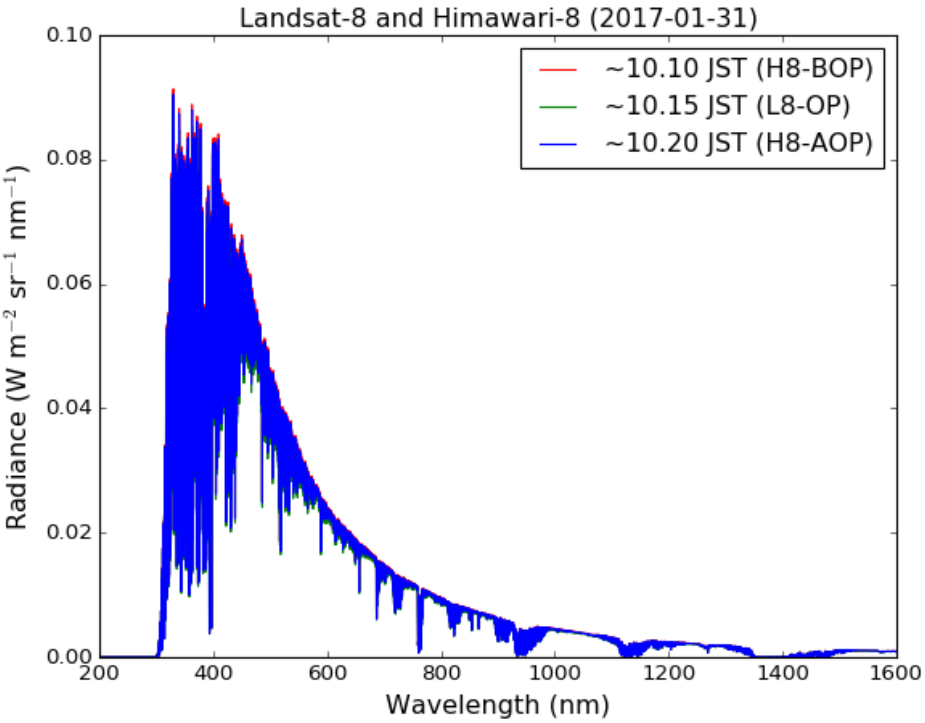

Figure 4.59: Radiance in 2017-01-31 with H8-BOP (SZA=58.34 and SAA=150.86), L8-OP (SZA=58.14 and SAA=152.51), and H8-AOP (SZA=57.39 and SAA=153.44).

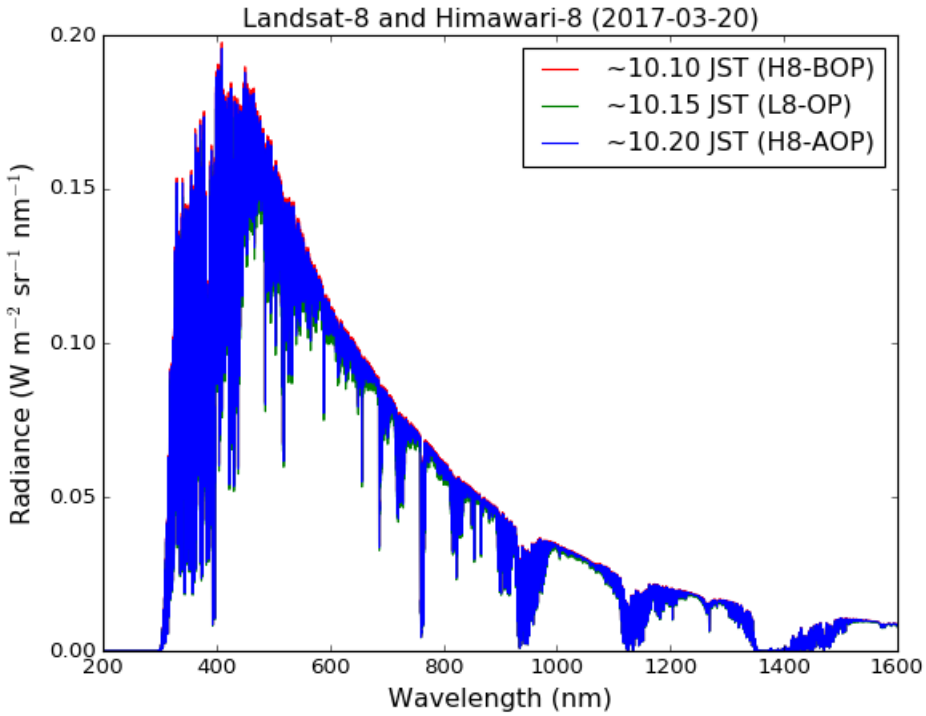

Figure 4.60: Radiance in 2017-03-20 with H8-BOP (SZA=41.17 and SAA=141.76), L8-OP (SZA=40.55 and SAA=143.42), and H8-AOP (SZA=39.96 and SAA=145.12).

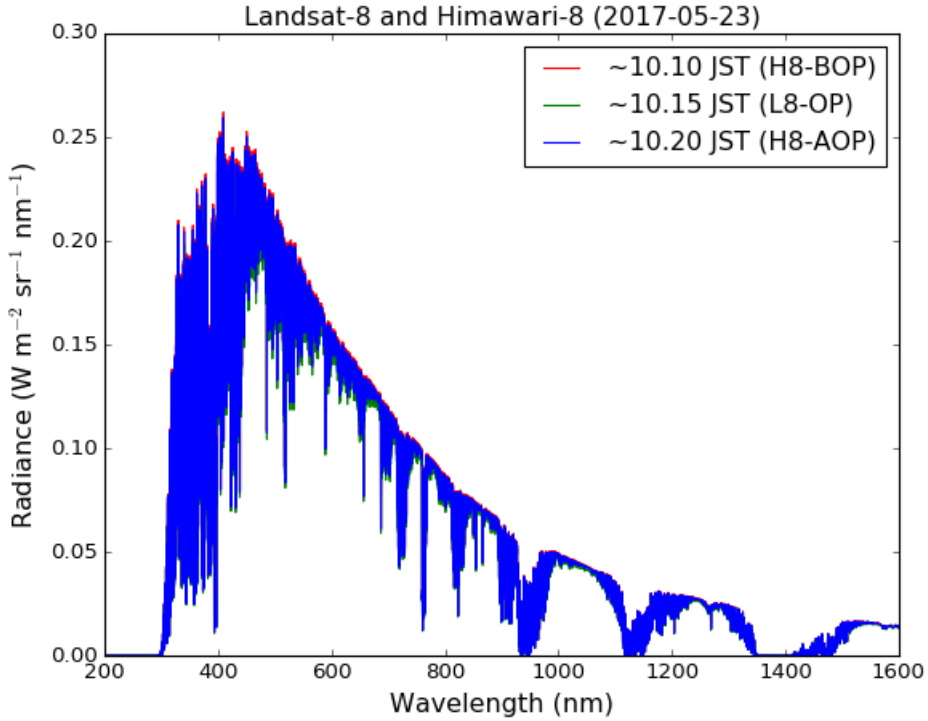

Figure 4.61: Radiance in 2017-05-23 with H8-BOP (SZA=24.16 and SAA=122.73), L8-OP (SZA=23.47 and SAA=125.76), and H8-AOP (SZA=22.49 and SAA=126.88).

4.1.9 Look up Table and Surface Reflectance

The Look-Up Tables (LUT) constructed from MODTRAN code based on radiance parameter are estimation process for separating contribution of atmospheric scattering and surface reflectance of satellite imagery data. Figures 4.62 to 4.65 show the LUT calculated for a visible band of Landsat-8 and Himawari-8 satellites, where the figures are a representation of both blue and green channels, respectively with the turn of presentation following the two previous sub-sections. In this simulation using MODTRAN, the atmospheric condition, aerosol type, and others important parameter are assumed to be those around 10:00 JST on that day Landsat-8 overpass and cover Kanto plan. The upper part indicate the change of apparent reflectance (ρ_{ap}) based on surface reflectance (ρ) for different values of AOT at 550 nm (τ_{550}). The lower part, on the other hand, show variation of relation AOT at 550 nm in the change condition of surface reflectance at the different apparent reflectance.

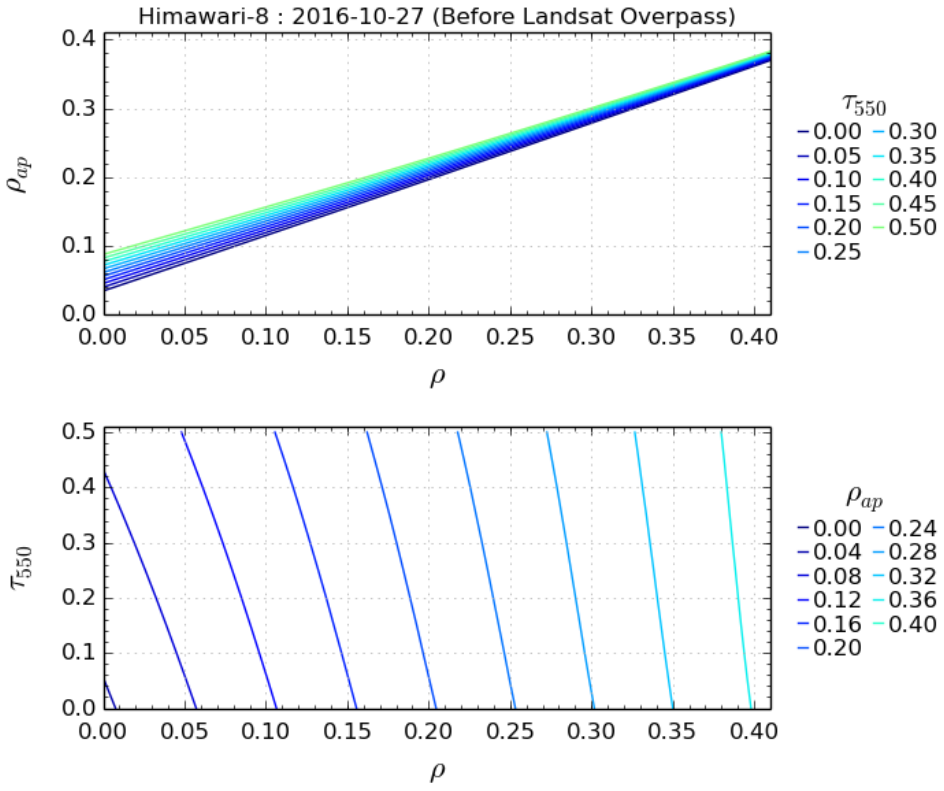

Figure 4.62: LUT of Landsat-8 and Himawari-8 satellites in 2016-10-27.

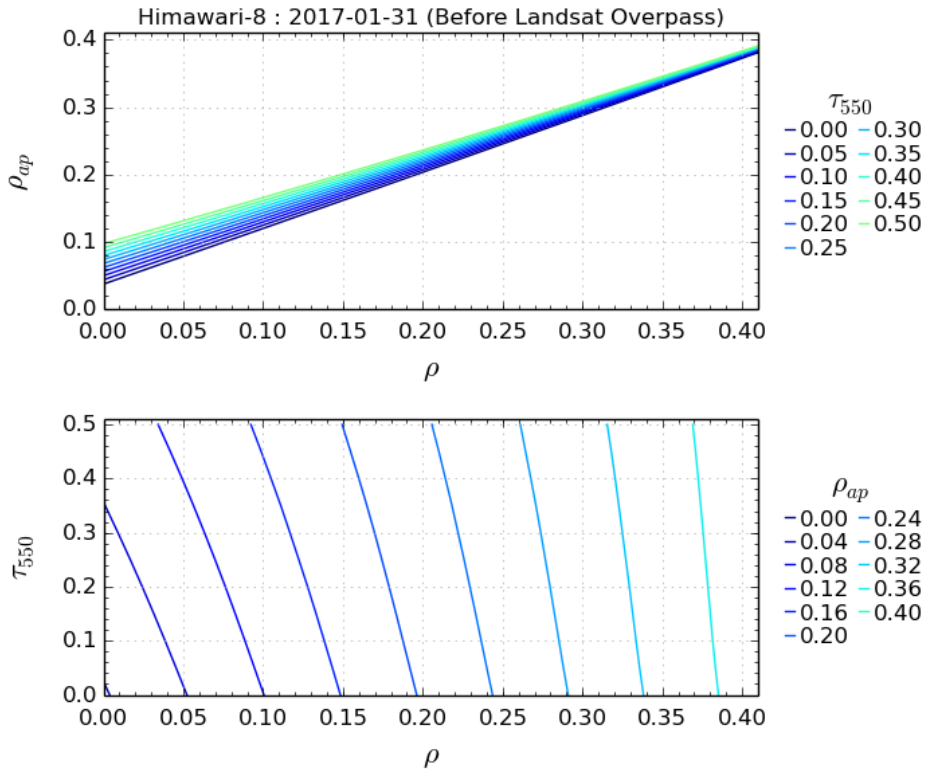

Figure 4.63: LUT of Landsat-8 and Himawari-8 satellites in 2017-01-31.

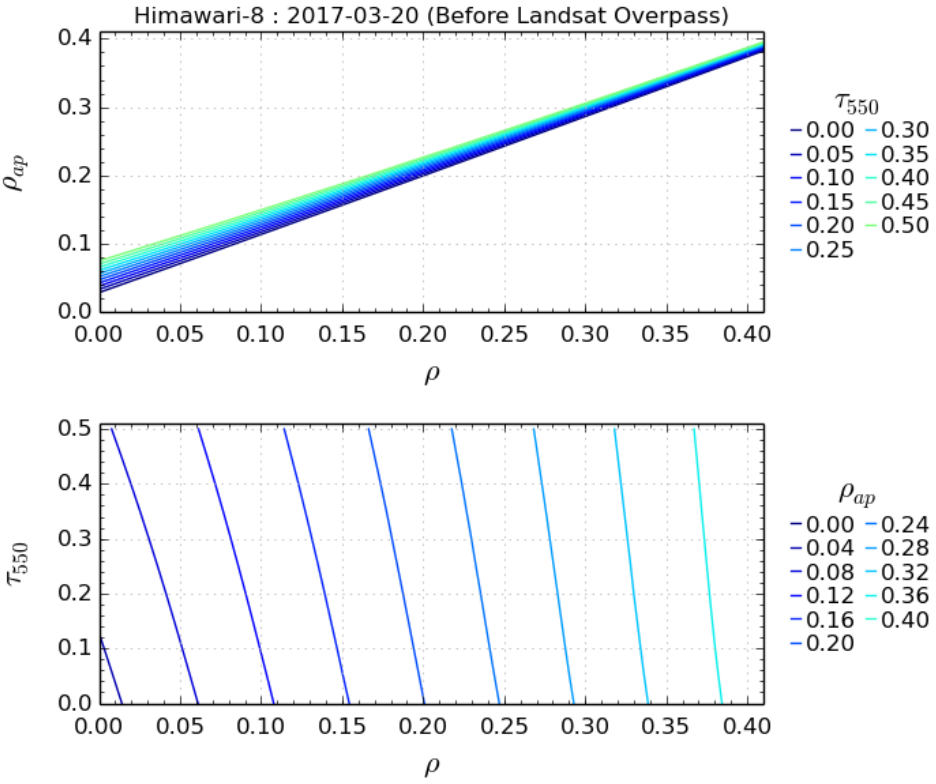

Figure 4.64: LUT of Landsat-8 and Himawari-8 satellites in 2017-03-20.

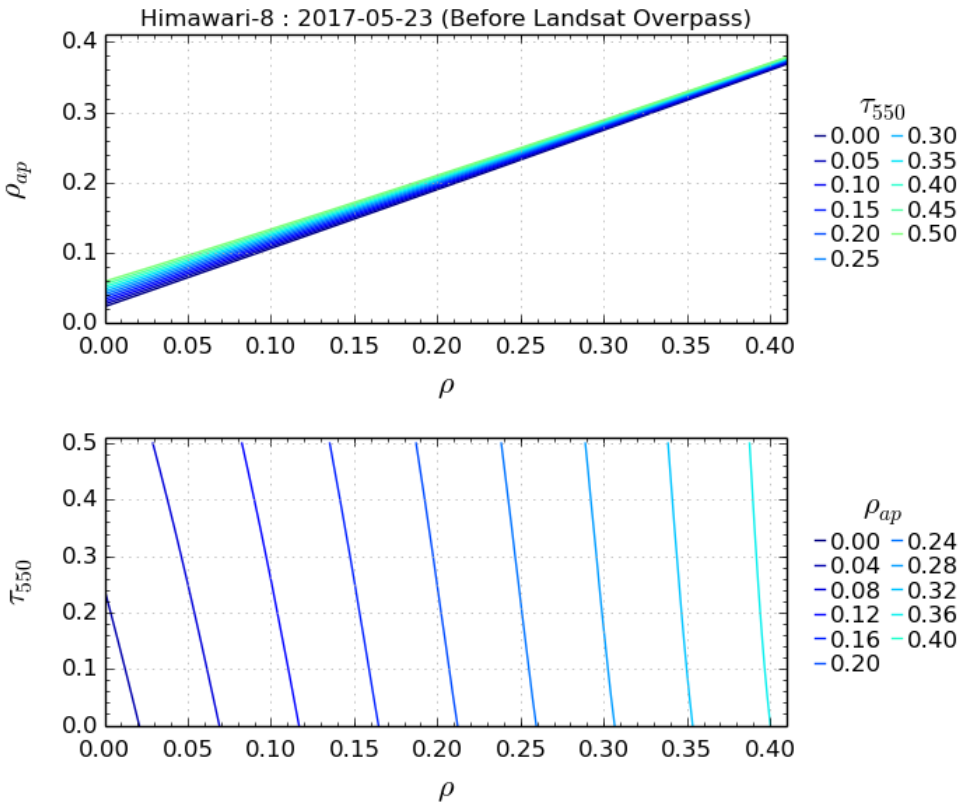

Figure 4.65: LUT of Landsat-8 and Himawari-8 satellites in 2017-05-23.

4.1.10 AOT Derived from Satellite Observation

The final step in analyzing of satellite data observation is a determination of AOT based on apparent and surface reflectance of Landsat-8 and Himawari-8 satellites. Practically, the implementation of this procedure is facilitated by using equation (3-14). The surface and apparent reflectance in sub-section 4.1.8 and 4.1.9, respectively are applying in this step, together with airmass derived from information in the panel (a) of Figures 3.36 to 3.39. The results of this AOT estimation are figured out in the same presentation and turn of the two previous sub-sections, where panels (a) and (b) are a representation of blue and green bands, respectively. The AOT spatial distributions in Figures 4.66 to 4.77 are started from Himawari-8 before the overpass (H8-BOP), Landsat-8 overpass (L8-OP), and Himawari-8 after the overpass (H8-AOP).

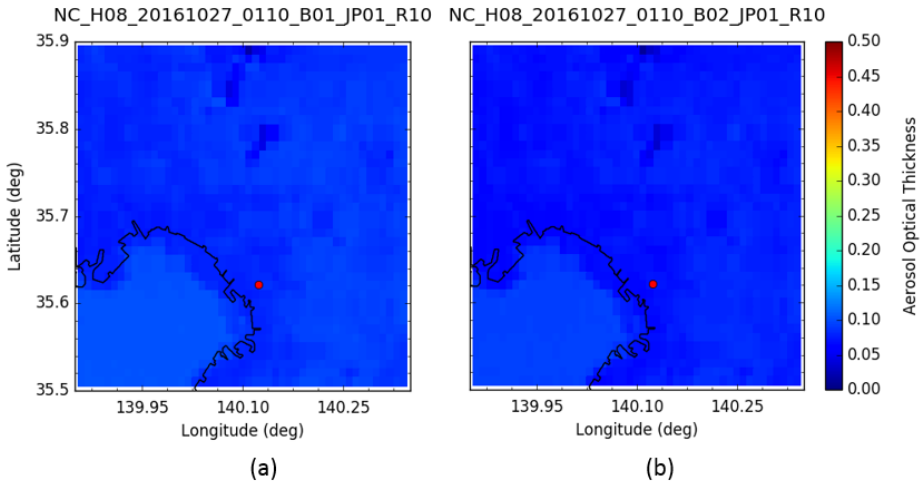

Figure 4.66: AOT of Himawari-8 before Landsat-8 overpass in 2016-10-27.

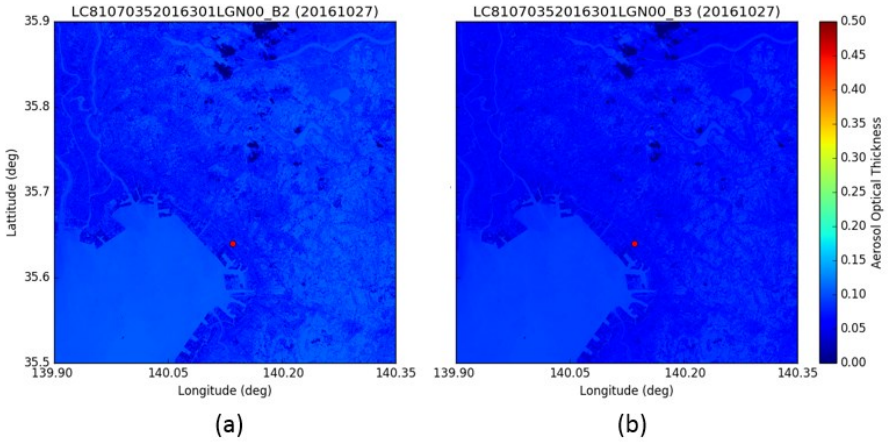

Figure 4.67: AOT of Landsat-8 in 2016-10-27.

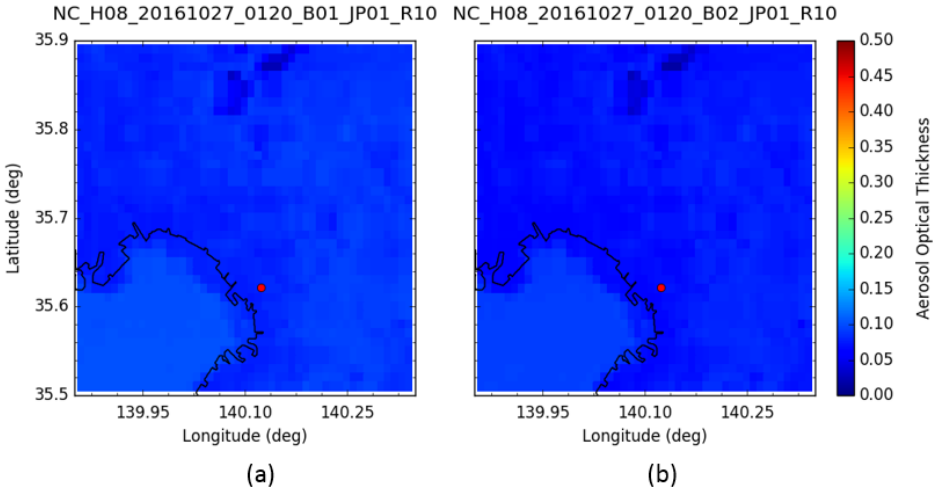

Figure 4.68: AOT of Himawari-8 after Landsat-8 overpass in 2016-10-27.

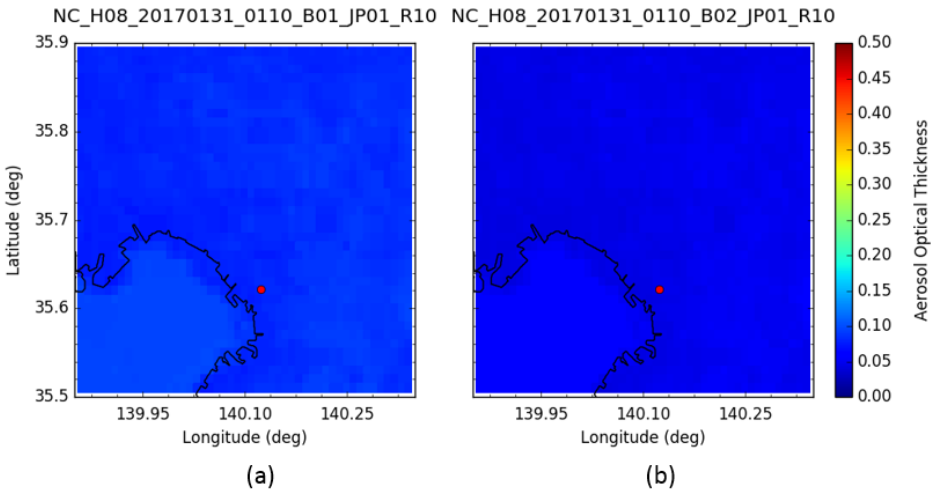

Figure 4.69: AOT of Himawari-8 before Landsat-8 overpass in 2017-01-31.

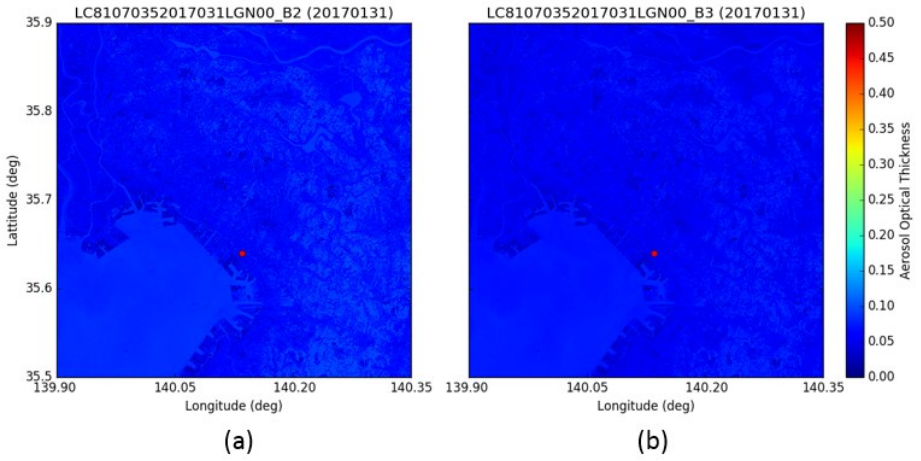

Figure 4.70: AOT of Landsat-8 in 2017-01-31.

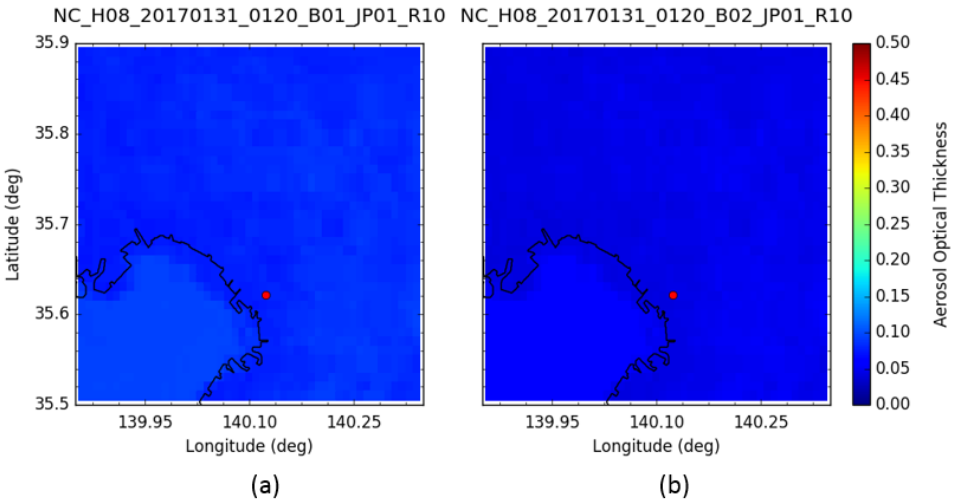

Figure 4.71: AOT of Himawari-8 after Landsat-8 overpass in 2017-01-31.

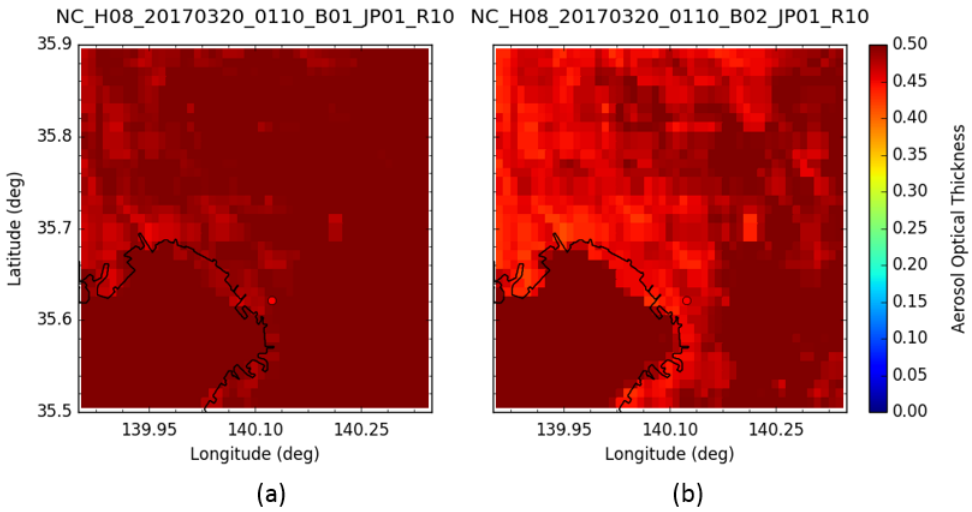

Figure 4.72: AOT of Himawari-8 before Landsat-8 overpass in 2017-03-20.

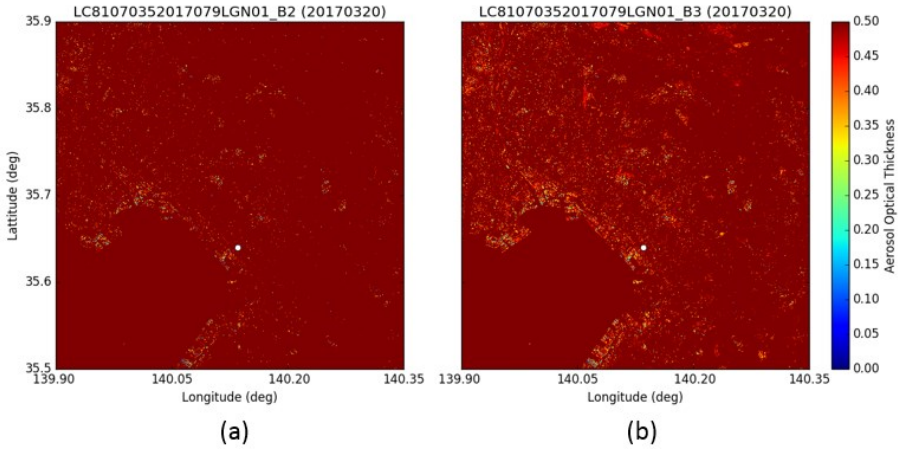

Figure 4.73: AOT of Landsat-8 in 2017-03-20.

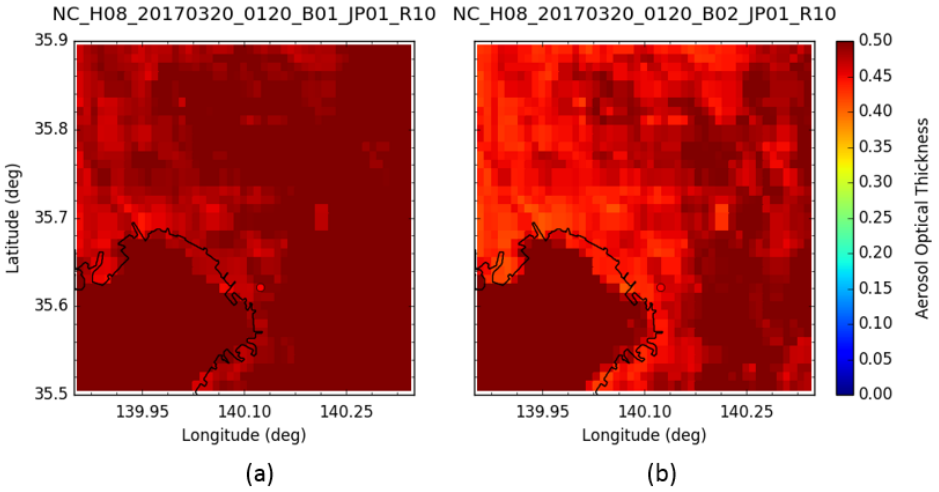

Figure 4.74: AOT of Himawari-8 after Landsat-8 overpass in 2017-03-20.

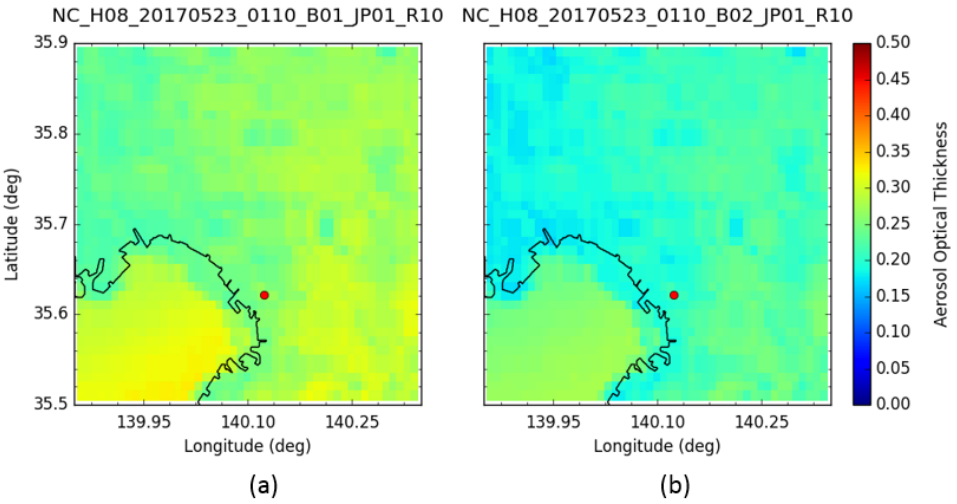

Figure 4.75: AOT of Himawari-8 before Landsat-8 overpass in 2017-05-23.

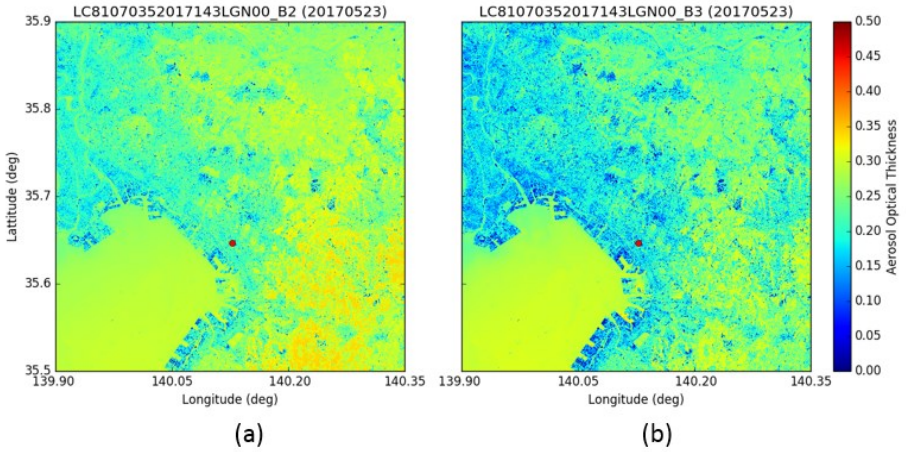

Figure 4.76: AOT of Landsat-8 in 2017-05-23.

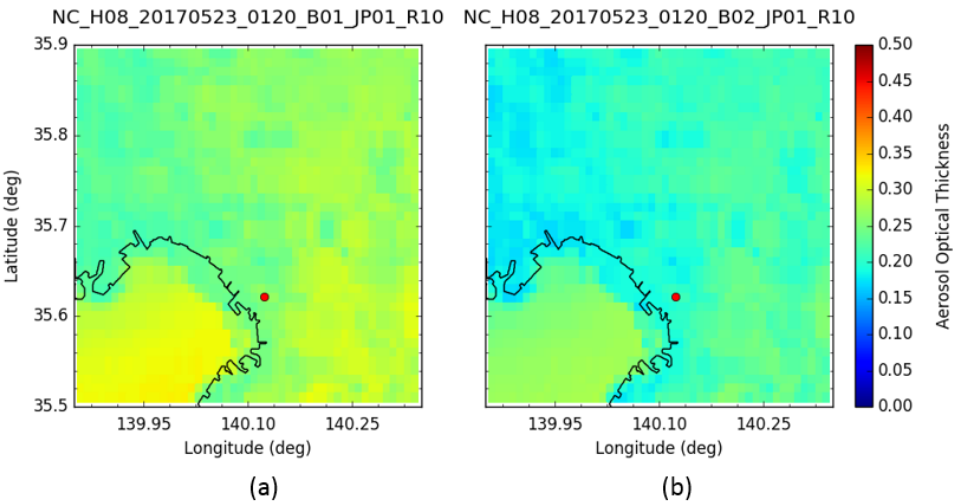

Figure 4.77: AOT of Himawari-8 after Landsat-8 overpass in 2017-05-23.

4.2 Analysis and Discussion

The whole graphics and tables in the results section are the gradual process to compare between aerosol extinction coefficient of lidar system from the surface and aerosol optical thickness of satellite sensor from the surface for both blue and green channels. The first comparison is spatial distribution aerosol extinction coefficient of PPI lidar (349 nm) in blue band range with AOT spatial distribution from both band-2 of Landsat-8 (482 nm) and band-1 of Himawari-8 (455). The temporal variations of SP and NIES lidars (532 nm), on the other hand, are compared to the band-3 of Landsat-8 (562 nm) and band-2 of Himawari-8 (510 nm). The atmosphere condition observed using weather monitor and aerosol characterization measured using ground-based sampling and optical instruments, on the other hand, are involved in supporting the analysis of tropospheric layer.

4.2.1 Atmospheric and Aerosol Characterizations using Ground Instruments

Table 4.2 lists the summary of ambient condition at overpass time of Landsat-8 in near free cloud condition. The indispensable parameter for analyzing and processing data is relative humidity (RH). The higher the RH which necessary hygroscopic correction is on May 23, 2017, with around ~58 %. On October 27, 2016, relatively stable employ truncation correction. The same treatment of sampling data is both on January 31, and March 20, 2017. The table confirms that within 5 minutes before and after Landsat-8 overpass time, there is no a drastic change of atmospheric condition.

Table 4.2: The average of atmospheric condition at the space observation based on Himawari-8 before Landsat overpass (H8-BOP), Landsat overpass time (L8-OP), and Himawari-8 after overpass (H8-AOP).

Date	Temperature (°C)	Rel. Humid. (%)	Air Press. (hPa)	Wi. Speed (m/s)	Wi. Direction	Time
20161027	23.80	45.00	1016.29	1.80	0.00	H8-BOP
	24.00	45.00	1016.36	2.20	337.50	L8-OP
	24.10	45.00	1016.32	1.80	0.00	H8-AOP
20170131	7.20	32.00	1017.71	0.40	112.50	H8-BOP
	7.00	30.00	1017.58	0.90	180.00	L8-OP
	7.00	30.00	1017.51	0.40	112.50	H8-AOP
20170320	15.60	26.00	1019.20	0.90	22.50	H8-BOP
	15.60	26.00	1019.20	0.90	67.50	L8-OP
	15.60	26.00	1019.37	0.90	22.50	H8-AOP
20170523	25.30	59.00	1009.79	3.10	202.50	H8-BOP
	25.20	58.00	1009.85	4.50	225.00	L8-OP
	24.90	58.00	1009.82	5.80	225.00	H8-AOP

Table 4.3 summarizes the aerosol characteristic based on the ground-based instruments. The average of corrected AEC (aerosol extinction coefficient) derived from sampling instruments (nephelometer and aethalometer), accompanied by AOT (aerosol optical thickness) based on sunphotometer and skyradiometer measurements. The AE median (Ångström exponent) is derived from sampling, sunphotometer, and skyradiometer. The time observations are H8-BOP (Himawari-8 before overpass), OP (Landsat-8 overpass), AOP (Himawari-8 after overpass). The smallest of all aerosol parameters are seen on 31 January 2017, followed by a condition on 27 October 2016, while the highest is seen on 20 March 2017. The middle condition is found on 23 May 2017.

Table 4.3: The average of corrected AEC, AOT, and AE with the time observations are H8-BOP (Himawari-8 before overpass), L8-OP (Landsat-8 overpass), H8-AOP (Himawari-8 after overpass). Both blue and green result from interpolation of sampling and optical measurements.

Date	AEC (1/km)		AOT		AE	Time
	blue	green	blue	green		
20161027	0.080	0.065	0.086	0.063	1.422	H8-BOP
	0.075	0.066	0.087	0.063	1.422	L8-OP
	0.080	0.066	0.087	0.063	1.422	H8-AOP
20170131	0.057	0.052	0.076	0.062	1.250	H8-BOP
	0.056	0.052	0.079	0.061	1.250	L8-OP
	0.056	0.052	0.079	0.062	1.251	H8-AOP
20170320	0.340	0.240	0.475	0.362	1.760	H8-BOP
	0.330	0.239	0.476	0.360	1.750	L8-OP
	0.310	0.237	0.476	0.365	1.750	H8-AOP
20170523	0.120	0.090	0.254	0.189	1.578	H8-BOP
	0.120	0.092	0.225	0.185	1.578	L8-OP
	0.123	0.094	0.225	0.188	1.578	H8-AOP

4.2.2 Correlation between space distribution of AEC and AOT of the Blue-band of Satellites

Figure 4.78 shows the spatial distributions of AEC (α_{ext}) at 349 nm obtained from the PPI lidar measurement, where the signal is processing by Fernald method in Equation (3-6). In this calculation, the value of lidar ratio, S_1, plotted in Figures 4.18 to 4.21 have been utilized for of the four days simultaneous measurements. The value of AEC in the near-end boundary are assumed as the sampling result (AEC and Ångström exponent) shown in Table 4.3. From Figure 4.78, the highest values of AEC are distributed on 20 March 2017 (Figure 4.78c) and the lowest

condition are seen on 31 January 2017 (Figure 4.78b). Overall of Figure 4.78 show the decreasing trend of AEC with radial distance from the center to the higher radius (around 2 km) is due to the slight (~4º) elevation angle of the PPI observation. The distributions of AEC more than 2 km are found to be more or less homogeneous.

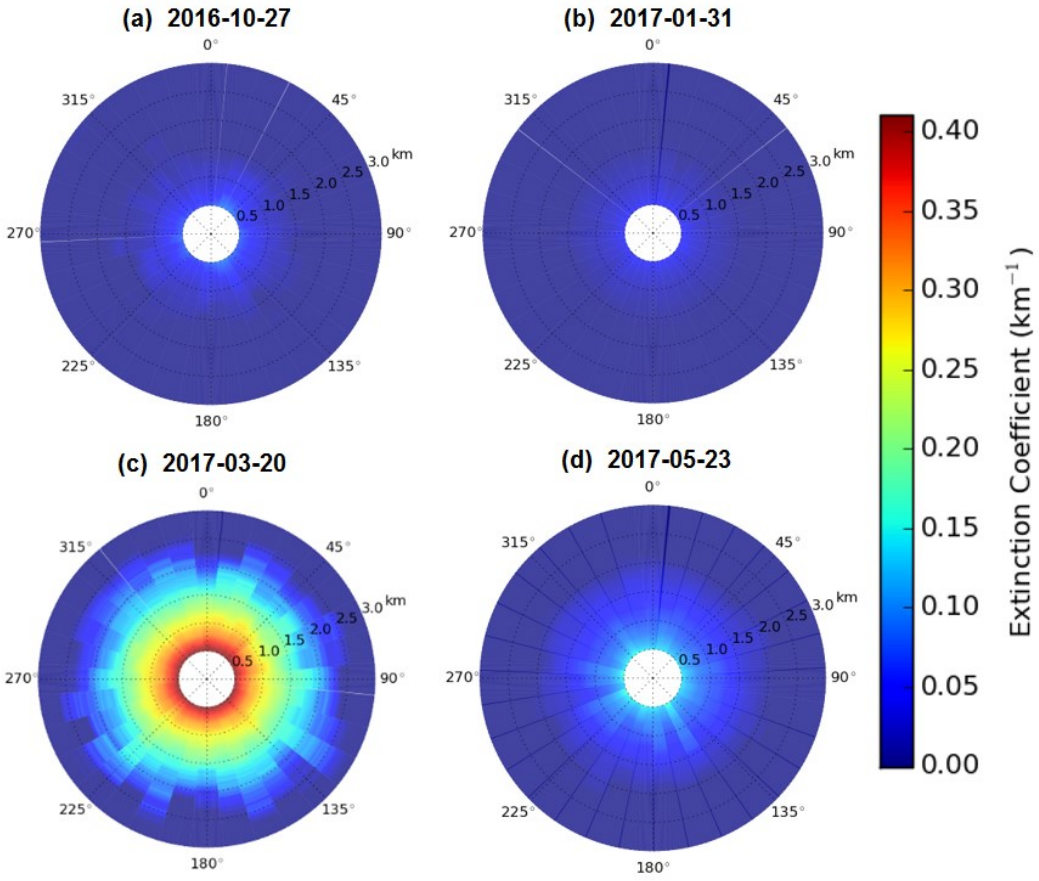

Figure 4.78: The near horizontal AEC distribution at 349 nm for 30 minute rotation at the time of Landsat-8 satellite overpass and Himawari-8 satellite cover Kanto area.

Figures 4.79 and 4.80 show the spatial distribution of AOT at 482 nm estimated using band-2 of Landsat-8 satellite and at 455 nm computed using band-1 of Himawari-8 satellite. Both AOTs almost show the same values but different resolution, where Landsat-8's higher than Himawari-8's. The nearly homogeneous values of AOT distribution (τ_{482}=0.06 – 0.08) in panel (a) is found on 27 October 2016, except for the north part of the areo of interest. The smallest condition AOT distribution (τ_{482}=0.05 - 0.07) is seen on panel (b) 31 January 2017 of both spatial

distribution. The highest AOTs (τ_{482}=0.45 – 0.50) are seen on segments (c) 20 March 2017. In panels (d) of both Figures (23 May 2017) the AOT distribution (τ_{482}=0.20 - 0.30) are found more inhomogen compare the other cases. The four day of spatial distribution of AOT derived from satellites observation in Figures 4.79 and 4.80 are corresponding to the ground measurement in Table 4.3. The AOT values in Table 4.3 show the highest AOT on 20 March 2017 (τ_{482}=0.476) while the smallest on 31 January 2017 (τ_{482}=0.079). Furthermore, the AOT characteristic observed using band-1 of Himawari-8 displayed in Figure 4.96 has a similar distribution with band-2 of Landsat-8 with uncertainty approximately 1-5%.

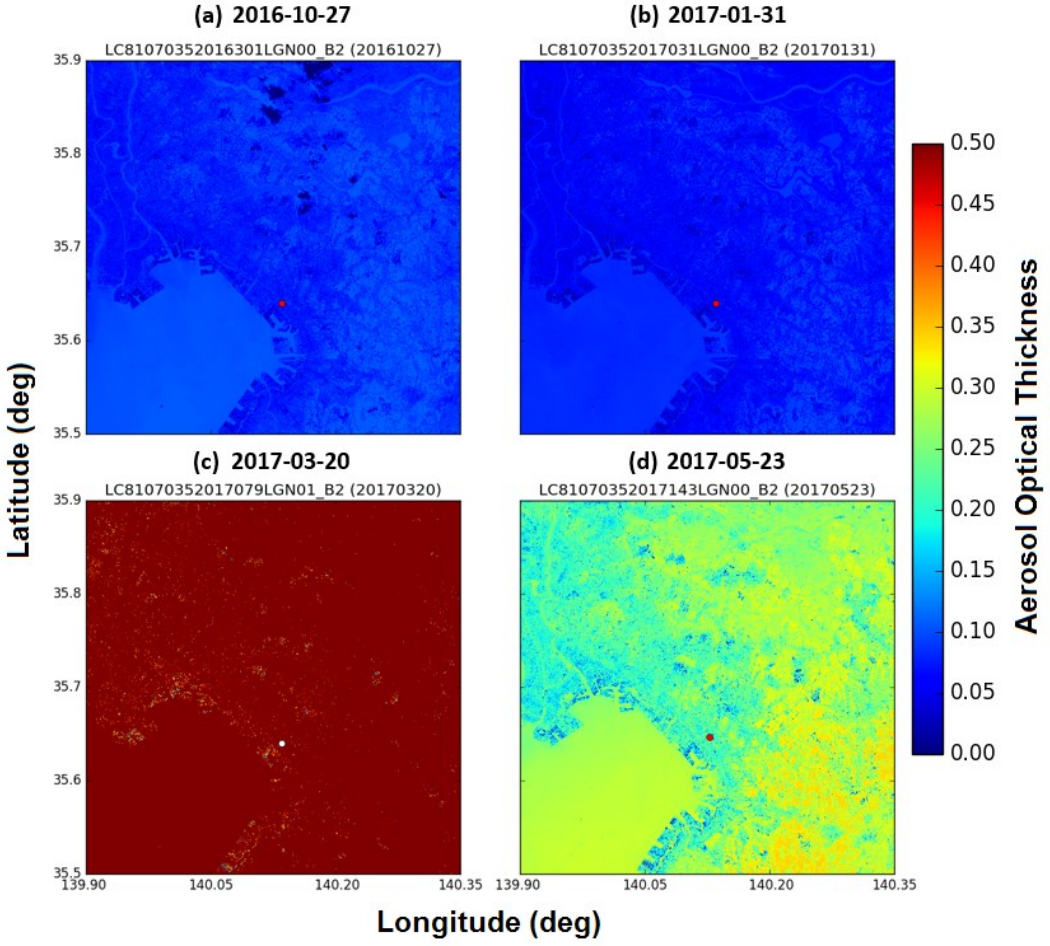

Figure 4.79: The spatial distribution of AOT at 482 nm derived from the analysis of band-2 images of Landsat-8 OLI, at the time of satellite overpass around 10:15 JST on (a) 27 October 2016, (b) 31 January 2017, (c) 20 March 2017, and (d) 23 May 2017.

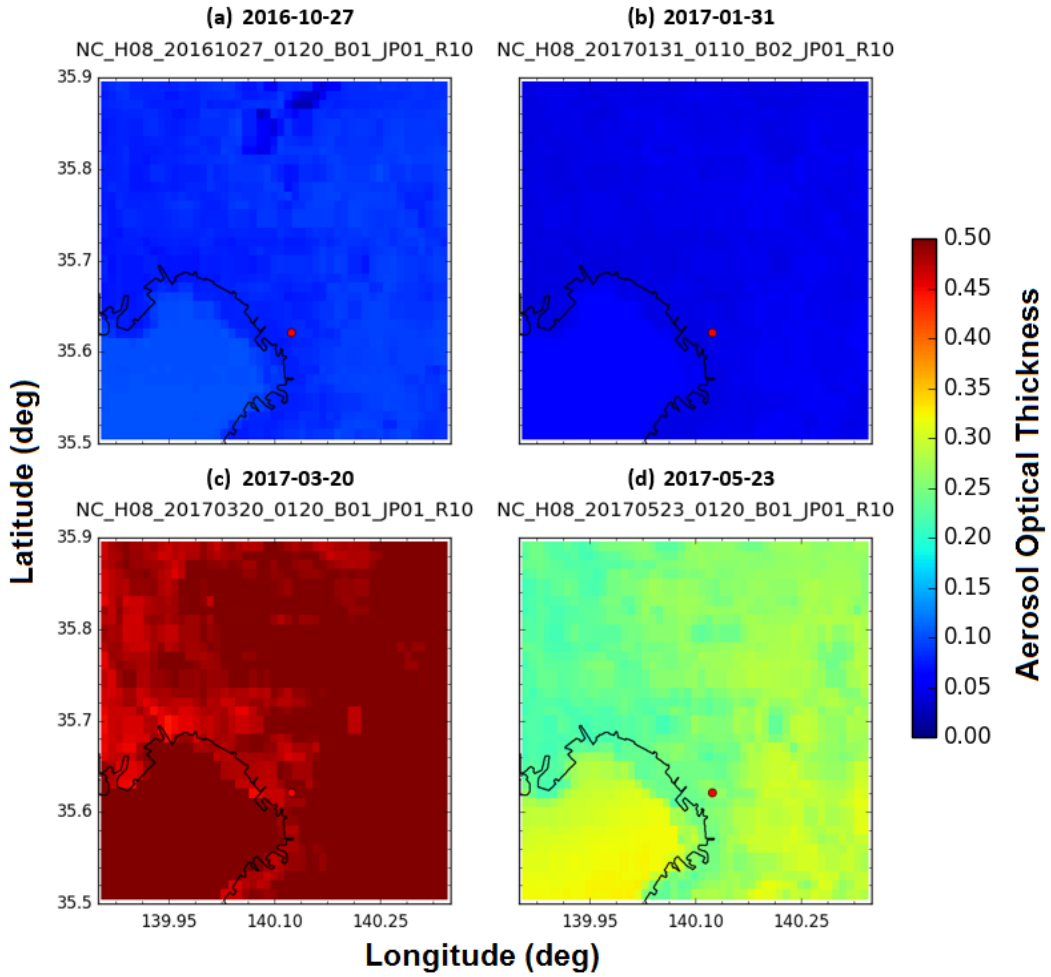

Figure 4.80: The spatial distribution of AOT at 455 nm derived from the analysis of band-1 images of Himawari-8, at the time of after overpass of Landsat-8 satellite around 10:20 JST on (a) 27 October 2016, (b) 31 January 2017, (c) 20 March 2017, and (d) 23 May 2017. The AOT distributions are seen similar to the band-2 of Landsat-8 observation with uncertainty around 1-5%.

4.2.3 Correlation between the Temporal change of AEC and AOT of the Green-band of Satellites

Figure 4.81 shows the temporal change of AEC (α_{ext}) in time heigh indicator derived SP lidar signal processing using Fernald analysis with the same method as PPI lidar. The value of lidar ratio with 532 nm plotted in Figures 4.18 to 4.21 has been involved in this computation for every data in this concurrent observation. By means the same estimation to 349 nm, the near-end boundary values of AEC is retrieved from sampling result (AEC and Ångström exponent) which are shown in

Table 4.3 (green part of AEC). In comparison to the spatial distribution of AOT derived from satellite sensors, the temporal variation of this AEC considered are from 10.00 to 10.30 JST (the same time of one rotation of PPI lidar). The patterns of the AEC's temporal distribution are almost same with PPI lidar observation, where the highest and lowest values of AEC are distributed on 20 March 2017 (panel c) and 31 January 2017 (panel b) of Figure 4.97, respectively. The decreasing trend of AEC with vertical distance is due to the slight (~30º) elevation angle of the SP measurement.

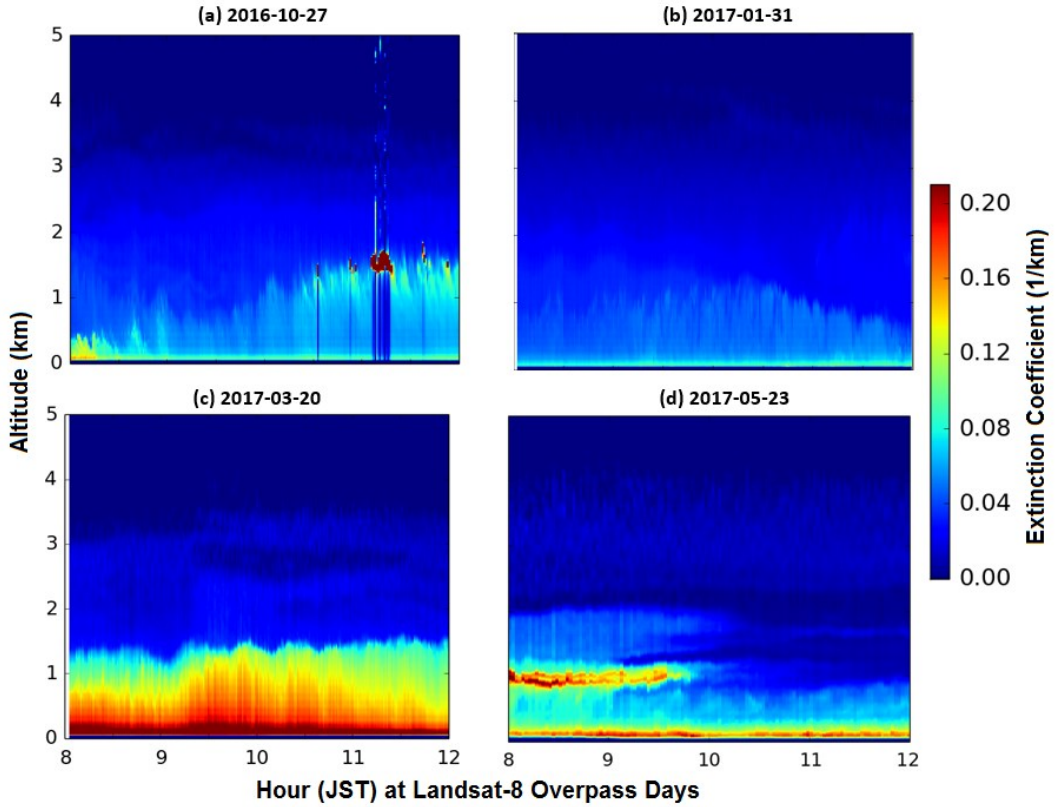

Figure 4.81: The temporal and column AEC distributions at 532 nm for 4 hours at the time of Landsat-8 satellite overpass and Himawari-8 satellite cover Kanto area.

Figures 4.82 and 4.83 show the spatial distribution of AOT observed using band-2 of Landsat-8 (562 nm) and band-1 (510 nm) of Himawari-8 satellites. Panel (a) of Figure 4.98 shows the nearly homogeneous AOT distribution (τ_{562} = 0.05–0.07) on 27 October 2016, except in the north part of the Kanto area. The smallest condition is seen on segment (b) 31 January 2017, with a homogeneous AOT

distribution approximately (τ_{562} =0.04 - 0.06). The highest AOT (τ_{562} =0.20 – 0.35) is seen on part (c) 20 March 2017. The most conspicuous of inhomogeneity of AOT (τ_{562} =0.09 - 0.10) compared to other conditions in Figure 4.98 are found on 23 May 2017. The whole AOTs characterization in Figure 4.98 is confirmed to the highest AOT is seen on the panel (c) 20 March 2017 (τ_{562} =0.239) while the smallest on segment (b) 31 January 2017 (τ_{562} =0.052). Finally, almost similar to the blue band, the band-2 of Himawari-8 observation show the same pattern of AOT distribution of the band-3 of Landsat-8 with a tourable deviation around 1-5%.

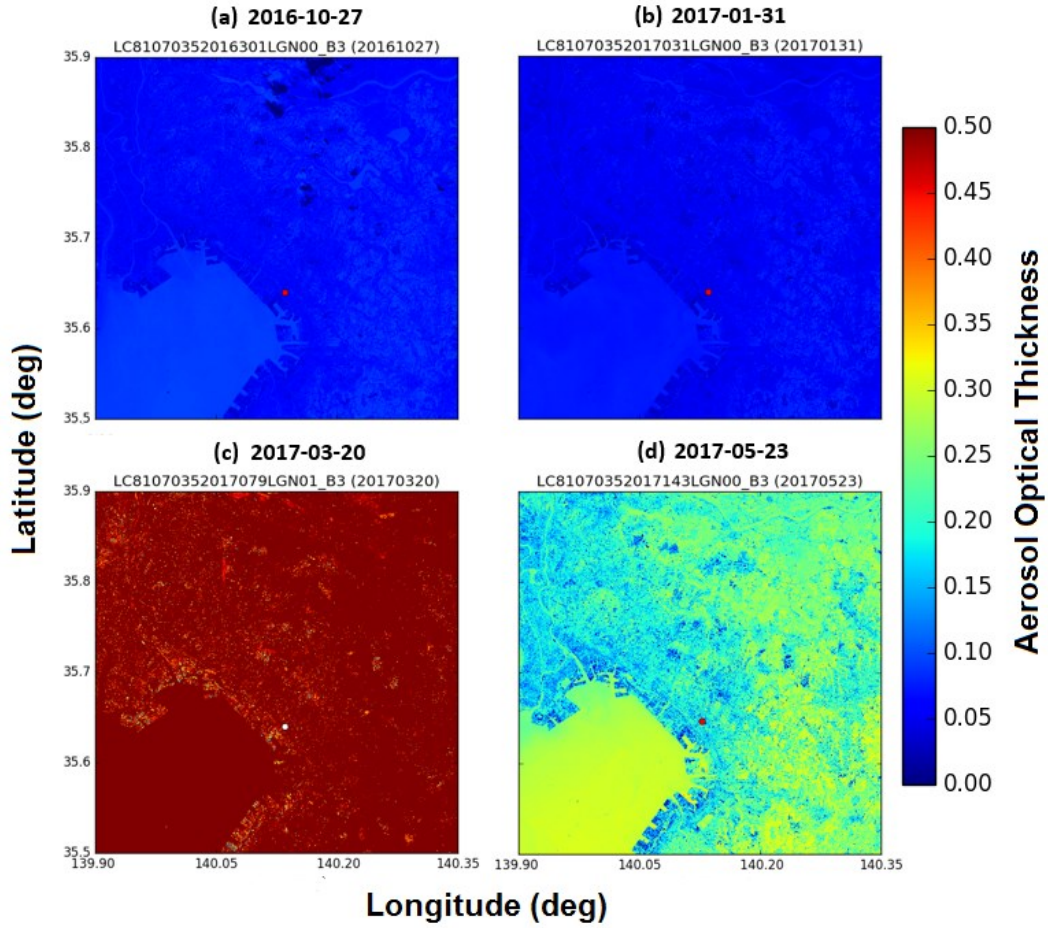

Figure 4.82: The spatial distribution of AOT at 562 nm derived from the analysis of band-3 images of Landsat-8 OLI, at the time of satellite overpass around 10:00 JST on (a) 27 October 2016, (b) 31 January 2017, (c) 20 March 2017, and (d) 23 May 2017. The highest AOT distribution is seen in (c) (τ_{482}= 0.45-0.50) while the smallest in (b) (τ_{482}=0.05 – 0.07).

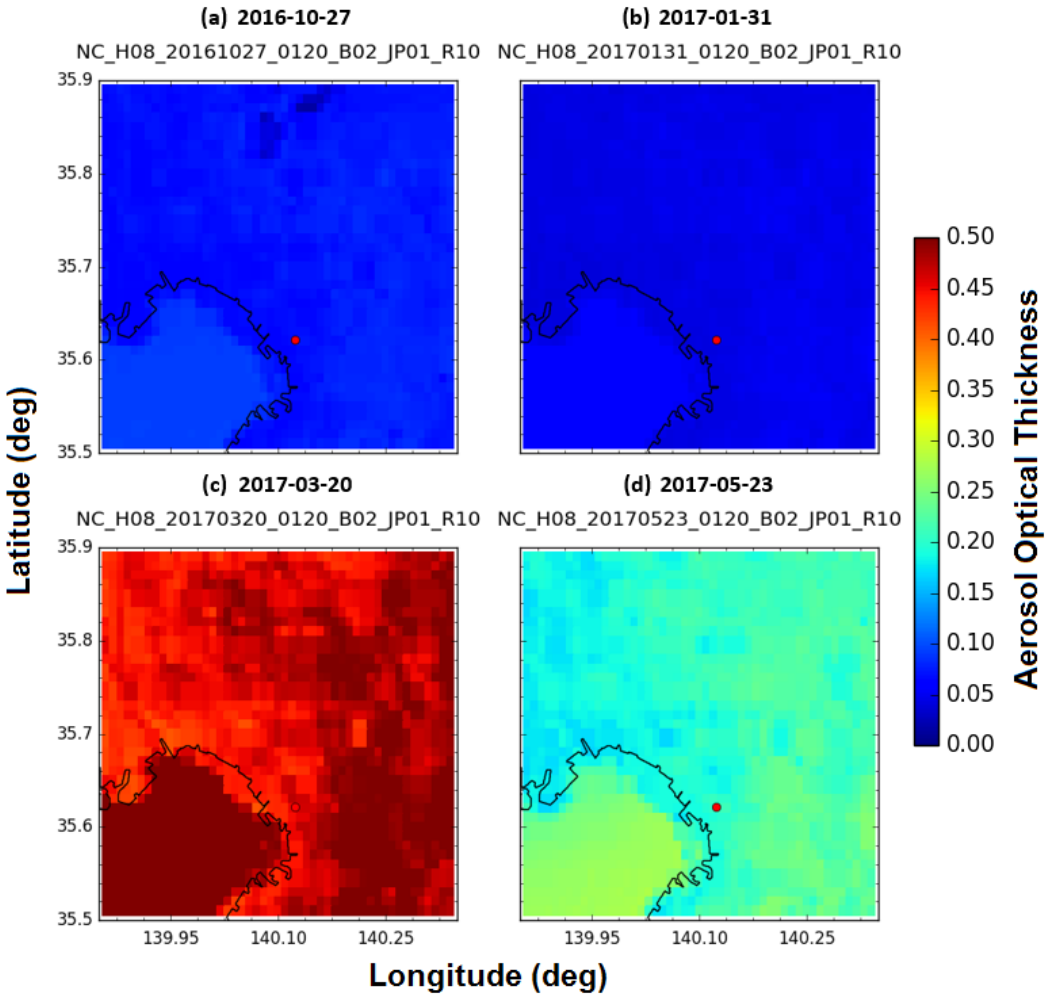

Figure 4.83: The spatial distribution of AOT at 510 nm derived from the analysis of band-2 images of Himawari-8, at the time of satellite overpass around 10:00 JST on (a) 27 October 2016, (b) 31 January 2017, (c) 20 March 2017, and (d) 23 May 2017. The AOT distributions are seen similar to the band-3 of Landsat-8 observation with uncertainty around 1-5%.

The main purpose of this study is developing a new monitoring technique for comparing the AEC distribution measured using lidar system from surface and AOT distribution observed using visible band of Landsat-8 and Himawari-8 satellites. During the four days of observation when Landsat-8 satellite overpass in the clear sky condition, we seek that the lowest AOT values of both Landsat-8 and Himawari-8 satellites are on 31 January 2017. The clearest condition mean the small aerosol loding where the lowest AEC from the lidar measurement is found in

the same condition of satellite observation. The results confim the theroretical concept that the AOT value has a linear corresponding with AEC.

The other fact of this present study is a consequence that the value of extinction correspond to the vertical aerosol distribution, in other word, the extinction coefficient is a function of elevation, $a_{ext}(z)$. It can bee seen in the spatial distribution of AEC based on PPI measurement, where in the center of circle distribution show the highest value rather than in the higher radius. On the circle graphic, we present distribution of AEC near horizontal with the elevation increase based on the radius of the circle. From the general concept about AEC variation dependent to the aerosol scale high (h_a) with the elevation approximately ~1-2 km, we know that the AEC as a function of elevation (z) is $a_{ext}(z) = a_{ext}(0) \exp(-z/h_a)$. Here, $a_{ext}(0)$ is the AEC directly measured with the PPI lidar.

Furthermore, the value of AOT, in the theoretical point of view, is a result of extinction coefficient integration as long as light propagation range. In this study we develop the concept in elevation measurement direction where the AOT is retrieved from the integration of $a_{ext}(z)$ over the whole troposphere. The integration result can be expressed in approximation as $\tau_A \sim h_a \, a_{ext}(0)$. The mathematics representation indicate that the AOT is correspond to the AEC in the change of elevation, h_a.

5. CONCLUSIONS AND RECOMMENDATION

5.1 Conclusions

A new monitoring technique has been proposed and implemented for retrieving atmospheric aerosol properties in the lower troposphere by means of ground-based from surface and satellite sensors observation from space. The benchmark measurements have been carried out at the time of Landsat-8 overpass over the Kanto area at around ~10.15 JST (Japan Standard Time). The Himawari-8 satellite, the world's first third-generation geostationary meteorological satellite with high temporal resolution (2.5 minutes for Japan area), is also employed in this observation. The ground-based instruments involved in this study are lidar systems, sampling instruments, a sunphotometer, a skyradiometer, and a visibility-meter. The sampling instruments employ in this study are an integrating nephelometer, an aethalometer, and optical particle counters. Besides, ambient meteorological conditions have been monitored using a weather monitor. Mostly concurrent datasets have been generated and analyzed from all of these sensors and instruments.

The ground sampling instruments are employed to observe the near-end boundary values of the aerosol extinction coefficient. In the case of lower relative humidity (RH), we apply only the truncation correction to the extinction coefficient obtained from the sampling measurement by comparing the data with those from visibility measurement. The truncation correction is indispensable to estimate the loss of signal intensity in the sampling process due to relatively particle coarse. For the higher relative humidity (RH > ~50%), on the other hand, an additional correction of the $f(RH)$ effect is considered. Here, $f(RH)$ means the correction of aerosol scattering cross-section due to the growth/evaporation process of hygroscopic components with the change of RH. The evaporation of hygroscopic aerosols occurs when the particles are introduced into the scattering volume of the instrument (where the RH is controlled to be relatively low) from ambient conditions with relative humidity higher than around ~50%.

Processing the PPI and SP lidar signals using the Fernald method provides the spatial and temporal distributions of AEC in the atmospheric boundary layer. The extinction to backscattering ratio (lidar ratio) is a key parameter for carrying out the Fernald analysis. The most plausible value of the lidar ratio is estimated by means of the Mie scattering calculation so as to reproduce the wavelength dependence of the sampling data while the size distribution is fiexed to the profile observed with the optical particle counters. Besides, this procedure provides the parameters that define the aerosol type as the significant input for the MODTRAN computation. The vertical aerosol profile data from the NIES lidar operated on the campus of Chiba University is also employed for checking the temporal variation of extinction coefficient.

The values of aerosol optical thickness (AOT) are calculated using the sunphotometer data. For the purpose of calibration, the signal level corresponding to the zero airmass (that corresponds to the solar radiation at the top of the atmosphere) is determined using the Langley extrapolation method by linearizing the equation of Lambert-Beer's law. This Langley plot analysis is implemented for the data taken under the most clear sky condition with stable (low) aerosol loading. The main correction factor employed in computing AOT are ozone (O_3) contribution derived from the GOME-2 satellite data. Furthermore, independent AOT data from the SKYNET skyradiometer are also used in this simultaneous observation for confirming the sunphotometer AOT. The original AOTs derived from both sunphotometer and skyradiometer are interpolated for the atmospheric correction analysis of the blue and green bands of both Landsat-8 and Himawari-8 satellites.

For the purpose of considering the wavelength dependence of the aerosol extinction coefficient in the lower troposphere, an additional parameter of Ångström exponent (AE) is also calculated using the sampling and optical data. The truncation correction is applied also to AE by comparing the wavelength dependence between the AEC of sampling and AOT optical measurement. Due to the values of AE resulted in this calculation are relatively stable regardless of the

atmospheric conditions including RH, the truncation correction is computed by combining the best data in the both low and high RH.

To determine the AOT from satellites images, we have applied the atmospheric correction to the image data of Landsat-8 and Himawari-8 satellites. From the apparent reflectance imagery derived from a visible band of both satellites, the contributions from the surface reflectance and atmospheric scattering are separated using a look-up table (LUT) based on the MODTRAN computation. The LUTs show how to determine the surface reflectance based on the change of apparent reflectance for various values of AOT at 550 nm. In the MODTRAN computation of the satellite-observed radiance, we exploite the AOT data from the sunphotometer and skyradiometer for estimating the reflectance distribution from a satellite image. Furthermore, the MODTRAN simulation result is involved in retrieving the spatial distribution of of AOT for the blue and green bands of Landsat-8 (bands 2 and 3) and Himawari-8 (bands 1 and 2) satellites.

As a whole, the methodology proposed in this work has demonstrated the usefulness of such a comprehensive approach for studying aerosol behavior in the lower troposphere, where most of the sources of particles are located. Most parameters employed in this computation are retrieved directly or indirectly, with applying some corrections, if necessary. Such parameters are also useful for giving constraints on the aerosol model that are applicable to the atmospheric correction of satellite remote sensing data. Through this analysis, a good correlation has been found between the AEC distribution from the lidar measurement (PPI, SP, and NIES) and that of the AOT from satellite observation (Landsat-8 and Himawari-8). This indicates the stability and homogeneity of the atmospheric boundary height, since a large part of AOT comes from the vertical integral of AEC inside this boundary layer.

5.2 Recommendation

A future possible extension to improve the accuracy of this current method is the adjustment of PPI lidar with variation wavelengths. The possible improvement

is the range of PPI's wavelength for scanning near-surface aerosol. A governing of red, green, and blue channels of PPI lidar appropriate to the wavelength of the satellite sensor will improve the usefulness of this present method. The same recommendation also for the temporal change comparison. Unfortunately, for the eyesafety precausion, it is not recommended to use visible lasers to the PPI measurement in the area with a lot of citizen. Instead, the mult-wavelength measurement will soon be carried out the LED DOAS system, and we hope that the comparison between the visibility-meter and LED DOAS will give us a chance for better understanding of the aerosol extinction near the surface level. Figure 5.1 show the scheme of LED DOAS which is developing in atmospheric remote sensing group at CEReS Chiba University.

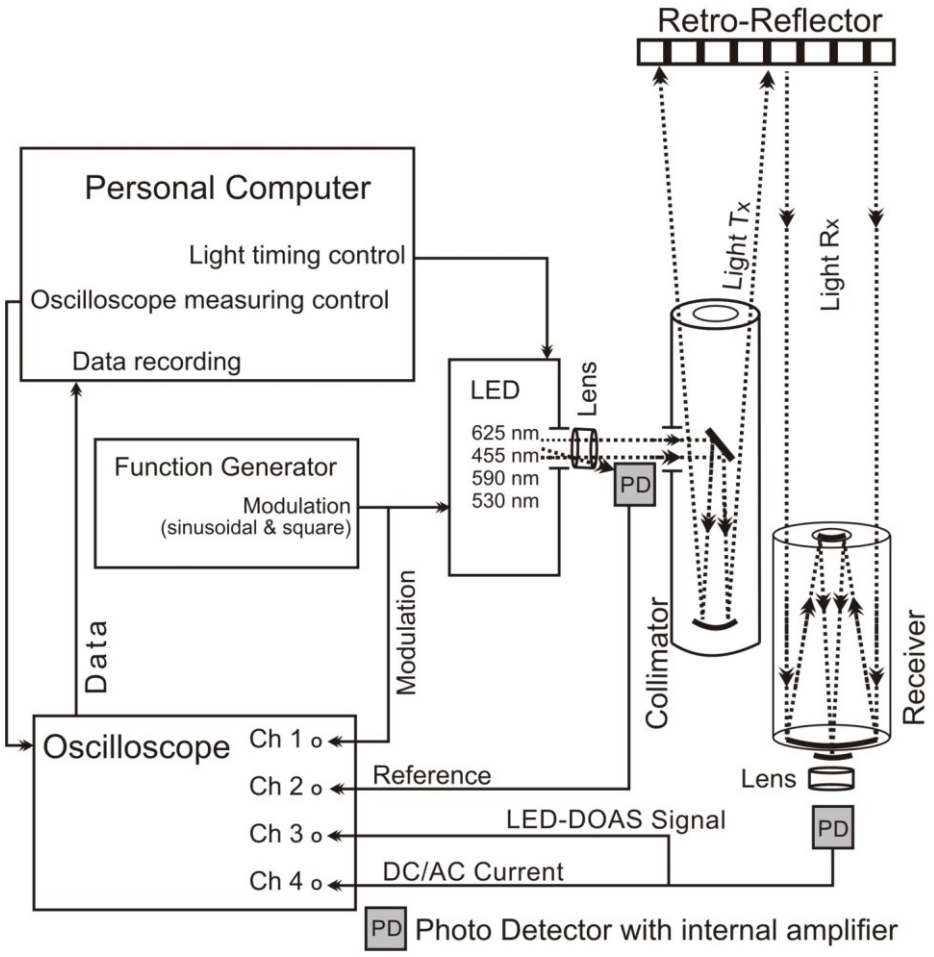

Figure 5.1: The scheme of LED-DOAS which is developing at CEReS-Chiba University

REFERENCES

[1] IPPC, "Climate Change 2007 : The Physical Science Basis," Geneva-Switzerland, 2007.

[2] H. Seinfeld and S. . Pandis, *Atmospheric Chemistry and Physics, from Air Pollution to Climate Change*. New York, USA: John Wiley & Sons, 1998.

[3] C. E. Chung, "Aerosol Direct Radiative Forcing : A Review," in *Atmospheric Aerosols – Regional Characteristics – Chemistry and Physics models*, In Tech Publication, 2012, pp. 379–394.

[4] H. Kuze, "Multi-Wavelength and Multi-Direction Remote Sensing of Atmospheric Aerosols and Clouds, Remote Sensing - Applications," in *InTech, Available from:*, D. B. Escalante, Ed. In Tech, 2012, pp. 279–294.

[5] H. Kuze, "Characterization of tropospheric aerosols by ground-based optical measurements," *SPIE Newsroom*, pp. 2–4, 2012.

[6] S. Tiwari and A. K. Singh, "Variability of Aerosol parameters derived from ground and satellite measurements over Varanasi located in the Indo-Gangetic Basin," *Aerosol Air Qual. Res.*, vol. 13, no. 2, pp. 627–638, 2013.

[7] L. Sun, J. Wei, M. Bilal, X. Tian, C. Jia, Y. Guo, and X. Mi, "Aerosol optical depth retrieval over bright areas using Landsat 8 OLI images," *Remote Sens.*, vol. 8, no. 1, pp. 1–14, 2016.

[8] D. Uesawa, "Aerosol Optical Depth product derived from Himawari-8 data for Asian dust monitoring," *Meteorol. Satell. Cent. Tech. Note*, no. 61, pp. 59–63, 2016.

[9] F. G. Fernald, "Analysis of atmospheric lidar observations: some comments.," *Appl. Opt.*, vol. 23, no. 5, p. 652, 1984.

[10] H. Kinjo, H. Kuze, T. Takamura, M. Yabuki, and N. Takeuchi, "Determination of aerosol extinction-to-backscattering ratio from multiwavelength lidar observation," *Jpn. J. Appl. Phys.*, vol. 40, no. 1, pp. 434–440, 2001.

[11] M. Yabuki, H. Kuze, H. Kinjo, and N. Takeuchi, "Determination of Vertical Distributions of Aerosol Optical Parameters by Use of Multi- Wavelength Lidar Data," *Jpn. J. Appl. Phys.*, vol. 42, no. 2A, pp. 686–694, 2003.

[12] N. Lagrosas, Y. Yoshii, H. Kuze, N. Takeuchi, S. Naito, A. Sone, and H. Kan, "Observation of boundary layer aerosols using a continuously operated, portable lidar system," *Atmos. Environ.*, vol. 38, no. 23, pp. 3885–3892, 2004.

[13] Y. Mabuchi, N. Manago, G. Bagtasa, H. Saitoh, N. Takeuchi, M. Yabuki, T. Shiina, and H. Kuze, "Multi-wavelength lidar system for the characterization

of tropospheric aerosols and clouds," in *International Geoscience and Remote Sensing Symposium (IGARSS)*, 2012, pp. 2505–2508.

[14] R. Jaenicke, *Tropospheric Aerosols in Aerosol-Cloud-Climate Interaction*. Academic Press, 1993.

[15] B. Gerry, N. Takeuchi, S. Fukagawa, H. Kuze, and S. Naito, "Correction in aerosol mass concentration measurements with humidity difference between ambient and instrumental conditions," *Atmos. Environ.*, vol. 41, pp. 1616–1626, 2007.

[16] H. Kuze, N. Lagrosas, J. Aminuddin, and N. Manago, "Study on the Relation of Aerosol Sampling Data and Aerosol Optical Characteristic," in *ISRS 2016 (Jeju, Korea)*, 2016.

[17] J. D. Klett, "Lidar inversion with variable backscatter/extinction ratios," *Appl. Opt.*, vol. 24, pp. 1638–1643, 1985.

[18] N. Lagrosas, H. Saito, T. Tsuneyoshi, N. Manago, and H. Kuze, "Effects of dust on aerosol scattering enhancement factor as measured with a ground-based slant path lidar in Chiba, Japan," in *Remote Sensing Conference*, 2015, vol. 30, no. May, pp. 20–21.

[19] A. M. Valdebenito B, S. Pal, A. Behrendt, V. Wulfmeyer, and G. Lammel, "A novel approach for the characterisation of transport and optical properties of aerosol particles near sources - Part II: Microphysics-chemistry-transport model development and application," *Atmos. Environ.*, vol. 45, no. 17, pp. 2981–2990, 2011.

[20] B. Rosati, E. Herrmann, S. Bucci, F. Fierli, F. Cairo, M. Gysel, R. Tillmann, J. Größ, G. Paolo Gobbi, L. Di Liberto, G. Di Donfrancesco, A. Wiedensohler, E. Weingartner, A. Virtanen, T. F Mentel, and U. Baltensperger, "Studying the vertical aerosol extinction coefficient by comparing in situ airborne data and elastic backscatter lidar," *Atmos. Chem. Phys.*, vol. 16, no. 7, pp. 4539–4554, 2016.

[21] L. Mei, P. Guan, Y. Yang, and Z. Kong, "Atmospheric extinction coefficient retrieval and validation for the single-band Mie-scattering Scheimpflug lidar technique," *Opt. Express*, vol. 25, no. 16, p. A628, 2017.

[22] J. Aminuddin, B. Purbantoro, N. Lagrosas, N. Manago, and H. Kuze, "Landsat-8 Satellite and Plan Position Indicator Lidar Observations for Retrieving Aerosol Optical Properties in the Lower Troposphere," *Adv. Remote Sens.*, vol. 07, no. 03, pp. 183–202, 2018.

[23] J. Aminuddin, S. Okude, N. Lagrosas, N. Manago, and H. Kuze, "Real Time Derivation of Atmospheric Aerosol Optical Properties by Concurrent Measurements of Optical and Sampling Instruments," *Open J. Air Pollut.*, vol. 07, no. 02, pp. 140–155, 2018.

[24] N. Y. Chubarova, A. A. Poliukhov, and I. D. Gorlova, “Long-term variability of aerosol optical thickness in Eastern Europe over 2001-2014 according to the measurements at the Moscow MSU MO AERONET site with additional cloud and NO2 correction,” *Atmos. Meas. Tech.*, vol. 9, no. 2, pp. 313–334, 2016.

[25] P. Zieger, R. Fierz-Schmidhauser, E. Weingartner, and U. Baltensperger, “Effects of relative humidity on aerosol light scattering: Results from different European sites,” *Atmos. Chem. Phys.*, vol. 13, no. 21, pp. 10609–10631, 2013.

[26] G. Titos, H. Lyamani, A. Cazorla, M. Sorribas, I. Foyo-Moreno, A. Wiedensohler, and L. Alados-Arboledas, “Study of the relative humidity dependence of aerosol light-scattering in southern Spain,” *Tellus, Ser. B Chem. Phys. Meteorol.*, vol. 66, no. 1, pp. 1–15, 2014.

[27] J. Chen, C. S. Zhao, N. Ma, and P. Yan, “Aerosol hygroscopicity parameter derived from the light scattering enhancement factor measurements in the North China Plain,” *Atmos. Chem. Phys.*, vol. 14, no. 15, pp. 8105–8118, 2014.

[28] J. Ackermann, “The extinction-to-backscatter ratio of tropospheric aerosol: A numerical study,” *J. Atmos. Ocean. Technol.*, vol. 15, no. 4, pp. 1043–1050, 1998.

[29] J. Qiu, “A Method to Determine Atmospheric Aerosol Optical Depth Using Total Direct Solar Radiation,” *J. Atmos. Sci.*, vol. 55, no. Kasten 1980, pp. 744–757, 1998.

[30] B. A. Bodhaine, N. B. Wood, E. G. Dutton, and J. R. Slusser, “On Rayleigh optical depth calculations,” *J. Atmos. Ocean. Technol.*, vol. 16, no. 11 PART 2, pp. 1854–1861, 1999.

[31] J. G. Cerqueira, J. H. Fernandez, J. J. Hoelzemann, N. M. P. Leme, and C. T. Sousa, “Langley method applied in study of aerosol optical depth in the Brazilian semiarid region using 500, 670 and 870 nm bands for sun photometer calibration,” *Adv. Sp. Res.*, vol. 54, no. 8, pp. 1530–1543, 2014.

[32] C. H. Jung, J. Um, J. Y. Lee, and Y. P. Kim, “Sensitivity analysis of the Angstrom exponent for multimodal aerosol size distributions,” *Asia-Pacific J. Atmos. Sci.*, vol. 49, no. 5, pp. 625–634, 2013.

[33] W. P. Arnott, K. Hamasha, H. Moosmüller, P. J. Sheridan, and J. A. Ogren, “Towards aerosol light-absorption measurements with a 7-wavelength aethalometer: Evaluation with a photoacoustic instrument and 3-wavelength nephelometer,” *Aerosol Sci. Technol.*, vol. 39, no. 1, pp. 17–29, 2005.

[34] T. Müller, J. S. Henzing, G. De Leeuw, A. Wiedensohler, A. Alastuey, H. Angelov, M. Bizjak, M. Collaud Coen, J. E. Engström, C. Gruening, R. Hillamo, A. Hoffer, K. Imre, P. Ivanow, G. Jennings, J. Y. Sun, N. Kalivitis,

H. Karlsson, M. Komppula, P. Laj, S. M. Li, C. Lunder, A. Marinoni, S. Martins Dos Santos, M. Moerman, A. Nowak, J. A. Ogren, A. Petzold, J. M. Pichon, S. Rodriquez, S. Sharma, P. J. Sheridan, K. Teinilä, T. Tuch, M. Viana, A. Virkkula, E. Weingartner, R. Wilhelm, and Y. Q. Wang, "Characterization and intercomparison of aerosol absorption photometers: Result of two intercomparison workshops," *Atmos. Meas. Tech.*, vol. 4, no. 2, pp. 245–268, 2011.

[35] I. N. Tang, "Chemical and size effects of hygroscopic aerosols on light scattering coefficients," *J. Geophys. Res. Atmos.*, vol. 101, no. D14, pp. 19245–19250, 1996.

[36] O. Dubovik, B. Holben, T. F. Eck, A. Smirnov, Y. J. Kaufman, M. D. King, D. Tanré, and I. Slutsker, "Variability of Absorption and Optical Properties of Key Aerosol Types Observed in Worldwide Locations," *J. Atmos. Sci.*, vol. 59, no. 3, pp. 590–608, 2002.

[37] T. F. Eck, B. N. Holben, J. S. Reid, O. Dubovik, A. Smirnov, N. T. O'Neill, I. Slutsker, and S. Kinne, "Wavelength dependence of the optical depth of biomass burning, urban, and desert dust aerosols," *Journal of Geophysical Research*, vol. 104, no. 1. p. 31333, 1999.

[38] Y. J. Kaufman, "Aerosol Optical Thickness and Atmospheric Path Radiance," *J. Geophys. Res.*, vol. 98, pp. 2677–2692, 1993.

[39] N. Manago, S. Miyazawa, Bannu, and H. Kuze, "Seasonal variation of tropospheric aerosol properties by direct and scattered solar radiation spectroscopy," *J. Quant. Spectrosc. Radiat. Transf.*, vol. 112, no. 2, pp. 285–291, 2011.

[40] G. E. Shaw, "Sun Photometry," *Bulletin of the American Meteorological Society*, vol. 64, no. 1. pp. 4–10, 1983.

[41] A. Ångström, "The parameters of atmospheric turbidity," *Tellus*, vol. 16, no. 1, pp. 64–75, 1964.

[42] E. Marino, P. Ranz, J. L. Tome, M. A. Noriega, J. Esteban, J. Madrigal, J. Luis, M. Ángel, J. Esteban, and J. Madrigal, "Generation of high-resolution fuel model maps from discrete airborne laser scanner and Landsat-8 OLI : A low-cost and highly updated methodology for large areas," *Remote Sens. Environ.*, vol. 187, pp. 267–280, 2016.

[43] W. Schroeder, P. Olivia, L. Giglio, B. Quayle, E. Lorenz, and F. Morelli, "Active fire detection using Landsat-8/OLI data," *Remote Sens. Environ.*, vol. 185, pp. 210–220, 2016.

[44] K. Bessho, K. Date, M. Hayashi, A. Ikeda, T. Imai, H. Inoue, Y. Kumagai, T. Miyakawa, H. Murata, T. Ohno, A. Okuyama, R. Oyama, Y. Sasaki, Y. Shimazu, K. Shimoji, Y. Sumida, M. Suzuki, H. Taniguchi, H. Tsuchiyama, D. Uesawa, H. Yokota, and R. Yoshida, "An Introduction to Himawari-8/9 -

Japan's New-Generation Geostationary Meteorological Satellites," *J. Meteorol. Soc. Japan*, 2015.

[45] JMA, *Himawari Standard Data User ' s Guide*, Version 1. Tokyo-Japan: Japan Meteorological Agency, 2015.

[46] M. Hidehiko, T. Masaya, and K. Yuki, "VIS and IR bands of Himawari- - 8 / AHI compatible with those of MTSAT- - 2 / Imager," *Meteorol. Satell. Cent. Tech. Note*, no. 60, pp. 1–18, 2015.

[47] S. Chandrasekhar, *Radiative Transfer*. New York, USA: Dover Publications, Inc, 1960.

[48] W. G. Rees, *Physical Principles of Remote Sensing*, Third Edit. Cambridge: Cambridge University Press, 2010.

[49] F. X. Kneizys, G. P. Anderson, E. P. Shettle, W. O. Gallery, L. W. Abreu, J. E. A. Selby, J. H. Chetwynd, and S. A. Clough, "Users Guide to LOWTRAN 7," AFGL-TR-88-0177 ENVIRONMENTAL RESEARCH PAPERS, NO.1010, 1988.

[50] A. Berk, G. P. Anderson, P. K. Acharya, J. H. Chetwynd, L. S. Bernstein, E. P. Shettle, M. W. Matthew, S. Sciences, A. Force, S. V. Directorate, M. Command, and R. S. Division, "MODTRAN4 USER ' S MANUAL," 1999.

[51] E. Vermote, M. Herman, J. J. Morcrette, and S. Y. Kotchenova, "Second Simulation of a Satellite Signal in the Solar Spectrum - Vector (6SV)," 2006.

[52] E. F. Vermote and J. L. Deuzc, "Second Simulation of the Satellite Signal in the Solar Spectrum , 6s : An Overview," *IEEE Trans. Geosci. Remote Sens.*, vol. 35, no. 3, pp. 675–686, 1997.

[53] P. K. Acharya, A. Berk, G. P. Anderson, N. F. Larsen, S.-C. Tsay, and K. H. Stamnes, "MODTRAN4: Multiple Scattering and Bi-Directional Reflectance Distribution Function (BRDF) Upgrades to MODTRAN," *Proc. SPIE*, vol. 3756, no. July, pp. 354–362, 1999.

[54] M. Minomoura, H. Kuze, and N. Takeuchi, "Atmospheric Correction of Visible and Near-infrared Satellite Data using Radiance Components : an Improved Treatment of Adjacency Effect," *J. Remote Sens. Soc. Japan*, vol. 21, no. 3, pp. 260–271, 2001.

[55] M. Minomura, H. Kuze, and N. Takeuchi, "Adjacency Effect in the Atmospheric Correction of Satellite Remote Sensing Data: Evaluation of the Influence of Aerosol EXtinction Profiles," *Opt. Rev.*, vol. 8, no. 2, pp. 133–141, 2001.

[56] S. Y. Kotchenova and E. F. Vermote, "Validation of a vector version of the 6S radiative transfer code for atmospheric correction of satellite data. Part II. Homogeneous Lambertian and anisotropic surfaces.," *Appl. Opt.*, vol. 46, no.

20, pp. 4455–4464, 2007.

[57] S. Y. Kotchenova, E. F. Vermote, R. Levy, and A. Lyapustin, "Radiative transfer codes for atmospheric correction and aerosol retrieval : intercomparison study," *Appl. Opt.*, vol. 47, no. 13, pp. 2215–2226, 2008.

[58] P. Susmitha and G. Sowmyabala, "Design and Implementation of Weather Monitoring and Controlling System," *Int. J. Comput. Appl.*, vol. 97, no. 3, pp. 975–8887, 2014.

[59] R. Penndorf, "Tables of the refractive index for standard air and the Rayleigh scattering coefficient for the spectral region between 0.2 and 20.0 and their application to atmospheric optics," *J. Opt. Soc. Amer*, vol. 47, no. 2, pp. 176–186, 1957.

[60] E. . Dutton, P. Reddy, S. Ryan, and J. J. DeLuisi, "Features and Effects of Aerosol Optical Depth Observed at Mauna Loa, Hawaii: 1982-1992," *J. Geophys. Res*, vol. 99, no. D4, pp. 8295–8306, 1994.

[61] H. Saito, N. Manago, K. Kuriyama, and H. Kuze, "Near-infrared open-path measurement of CO2 concentration in the urban atmosphere.," *Opt. Lett.*, vol. 40, no. 11, pp. 2568–2571, 2015.

[62] T. L. Anderson and J. A. Ogren, "Determining Aerosol Radiative Properties Using the TSI 3563 Integrating Nephelometer," *Aerosol Sci. Technol.*, vol. 29, no. 1, pp. 57–69, 1998.

[63] J. V. Winstanley and M. J. Adams, "Point Visibility Meter: a forward scatter instrument for the measurement of aerosol extinction coefficient," *Appl. Opt.*, vol. 14, no. 9, pp. 2151–2157, 1975.

[64] R. Al-Jarrah, "On the Lagrange interpolation polynomials of entire functions," *J. Approx. Theory*, vol. 41, no. 2, pp. 170–178, 1984.

[65] G. Criscuolo, "Lagrange interpolation with constraints," *J. Comput. Appl. Math.*, vol. 50, no. 1–3, pp. 185–196, 1994.

[66] J. Aminuddin, *Fundamentals of Computational Physics using MATLAB*, 1st ed. Yogyakarta-Indonesia: Gavamedia, 2008.

[67] Y. Men, G. Zhang, C. Men, X. Li, and N. Ma, "A sub-pixel disparity refinement algorithm based on lagrange interpolation," *Chinese J. Electron.*, vol. 26, no. 4, pp. 784–789, 2017.

[68] Davis Instruments Corp., "Davis Vantage Pro2 Console Manual," p. 56, 2015.

[69] V. . Cachorro, A. . De Frutos, and M. . Gonzalez, "Analysis of the relationships between Junge size distribution and Ångström α turbidity parameters from spectral measurements of atmospheric aerosol extinction," *Atmos. Environ. Part A. Gen. Top.*, vol. 27, no. 10, pp. 1585–1591, 1993.

[70] J. Aminuddin, Y. Suenaga, T. Tsuneyoshi, S. Okude, N. Lagrosas, N. Manago, and H. Kuze, "Plan Position Indicator (PPI) Lidar Measurement of Horizontal Distribution of Aerosol Extinction Coefficient," in *34th Japanese Laser Sensing Symposium*, 2016, pp. 148–149.

[71] K. Soni, S. Singh, T. Bano, R. S. Tanwar, and S. Nath, "Wavelength dependence of the aerosol Angstrom exponent and its implications over Delhi, India," *Aerosol Sci. Technol.*, vol. 45, no. 12, pp. 1488–1498, 2011.

[72] B. I. Tijjani and S. Uba, "Dependence of the Angstrom Exponents on Wavelength and Relative Humidities for Four Types of Aerosols," *Int. J. Res. Rev. Pharm. Appl. Sci.*, vol. 2, no. 6, pp. 1085–1102, 2012.

[73] Y. J. Kaufman, R. S. Fraser, and R. L. Mahoney, "Fossil fuel and biomass burning effect on climate - Heating or cooling?," *Journal of Climate*, vol. 4, no. 6. pp. 578–588, 1991.

APPENDIX A : SCATTERING THEORY

The most popular scattering theory is classified into two types, the first is Rayleigh scattering, and the second is Mie scattering. Rayleigh scattering represented the interaction between light and molecule in the atmosphere, where the wavelength of scattered light is higher than an interacted particle. On the other hand, Mie scattering is an interaction between the wavelengths of light scattered with the higher diameter of aerosol. The main purposes of this formulation are to determine the lidar ratio due to molecule and aerosol.

Mie scattering

The lidar ratio formulation due to aerosol is started from the basic principle where lidar ratio (S_1) is the ratio between extinction (α_1) and backscattering (β_1).

$$\boldsymbol{S_1} = \frac{\boldsymbol{\alpha_1}}{\boldsymbol{\beta_1}} \tag{A-1}$$

The extinction coefficient is defined as:

$$\boldsymbol{\alpha_1 = n\sigma_{ext} = n(\sigma_{sca} + \sigma_{abs}) = n\,\frac{\sigma_{sca}}{\omega_0}} \tag{A-2}$$

Here, notation n, σ, and ω_0 represent the aerosol density, cross-section (of extinction, scattering, and absorption), and single-scattering albedo respectively. To determine the cross-section of the scattering particle is defined as a dielectric sphere. Consequently, the differential cross-section is written in:

$$\frac{\boldsymbol{d\sigma_{sca}}}{\boldsymbol{d\Omega}} = \frac{\boldsymbol{i_{1+i_2}}}{\boldsymbol{2k^2}} \tag{A-3}$$

Parameters i_1 and i_2 are the electric field vector of light intensity in perpendicular and parallel directions respectively. Both are expressed in term of amplitude function (S) as:

$$\boldsymbol{i_1 = \left|\vec{S}_1(\theta)\right|^2} \tag{A-4}$$

$$\boldsymbol{i_2 = \left|\vec{S}_2(\theta)\right|^2} \tag{A-5}$$

Where both $S_1(\theta)$ and $S_2(\theta)$ represent in:

$$\boldsymbol{\vec{S}_1(\theta) = \sum_{l=1}^{\infty} \frac{2l+1}{l(l+1)} \{a_l \phi_l \cos\theta + b_l \varphi_l \cos\theta\}} \tag{A-6}$$

$$\vec{S}_2(\theta) = \sum_{l=1}^{\infty} \frac{2l+1}{l(l+1)} \{a_l \phi_l \cos\theta + b_l \varphi_l \cos\theta\} \quad \text{(A-7)}$$

In equations (A-6) and (A-7), there are parameters a_l, b_l, ϕ_l, and φ_l. They are defined as:

$$a_l = \frac{\psi_l'(\tilde{n}\,ka)\,\psi_l(ka) - \tilde{n}\,\psi_l(\tilde{n}\,ka)\psi_l'(ka)}{\psi_l'(\tilde{n}\,ka)\,\xi_l(ka) - \tilde{n}\,\psi_l(\tilde{n}\,ka)\xi_l'(ka)} \quad \text{(A-8)}$$

$$b_l = \frac{\psi_l'(\tilde{n}\,ka)\,\psi_l(ka) - \tilde{n}\,\psi_l(\tilde{n}\,ka)\psi_l'(ka)}{\psi_l'(\tilde{n}\,ka)\,\xi_l(ka) - \tilde{n}\,\psi_l(\tilde{n}\,ka)\xi_l'(ka)} \quad \text{(A-9)}$$

$$\phi \cos\theta = \frac{1}{\sin\theta} P_l^{(1)} \cos\theta \quad \text{(A-10)}$$

$$\varphi \cos\theta = \frac{d}{d\theta} P_l^{(1)} \cos\theta \quad \text{(A-11)}$$

By symbolizing $\xi = ka$, several parameters in equations (A-8) and (A-9) are described as electromagnetic components:

$$\psi_l(\xi) = (-1)^l\, \xi^{l+1} \left(\frac{d}{\xi\, d\xi}\right)^l \left(\frac{\sin\xi}{\xi}\right) \quad \text{(A-12)}$$

$$\chi_l(\xi) = (-1)^l\, \xi^{l+1} \left(\frac{d}{\xi\, d\xi}\right)^l \left(\frac{\cos\xi}{\xi}\right) \quad \text{(A-13)}$$

$$\xi_l(\xi) = \psi_l(\xi) K + i\, \chi_l(\xi) \quad \text{(A-14)}$$

Back to equation (A-3) as a differential cross-section of aerosol scattering, it is represented in the integral equation:

$$\sigma_{scat} = \iint \frac{d\sigma_{sca}}{d\Omega} \sin\theta\, d\theta\, d\varphi \quad \text{(A-15)}$$

By involving amplitude function (S) in equation (A-4) to (A-7), the scattering equation is written in:

$$\sigma_{scat} = \frac{\pi}{k^2} \int_0^{\pi} \left\{ \left|\vec{S}_1(\theta)\right|^2 + \left|\vec{S}_1(\theta)\right|^2 \right\} \sin\theta\, d\theta \quad \text{(A-16)}$$

Moreover, by means equation (A-8) to (A-14) into equation (A-16), the general formulation of scattering cross-section is found as:

$$\sigma_{scat} = \frac{4\pi}{k^2} \sum_{l=1}^{\infty} (2l+1)\, \mathrm{Im}\, [|a_l|^2 + |b_l|^2] \quad \text{(A-17)}$$

The absorption cross-section, on the other hand, is reported as real part by establishing scattering cross-section as:

$$\sigma_{abs} = \frac{4\pi}{k^2} \sum_{l=1}^{\infty} \left(l + \frac{1}{2}\right) \mathrm{Re}\, [|a_l|^2 + |b_l|^2] \quad \text{(A-18)}$$

Another parameter is indispensable in calculating lidar ratio is phase function as the ratio between differential cross-section in equation (A-3) and the scattering cross-section in equation (A-17):

$$\boldsymbol{f}\cos\boldsymbol{\theta} = \frac{\mathbf{1}}{\boldsymbol{\sigma_{sca}}}\left(\frac{\boldsymbol{d\sigma}}{\boldsymbol{d\Omega}}\right)_{\boldsymbol{\theta}} \tag{A-19}$$

Finally, the general formula of lidar ratio due to aerosol scattering is written in:

$$\boldsymbol{S_1} = \frac{\boldsymbol{\sigma_{sca}}}{\left(\frac{\boldsymbol{d\sigma}}{\boldsymbol{d\Omega}}\right)_{\boldsymbol{\theta}}} = \frac{\mathbf{1}}{\boldsymbol{f}\cos\boldsymbol{\theta}} \tag{A-20}$$

Rayleigh scattering

The lidar ratio formulation due to a molecule of air particle is started from the basic principle where lidar ratio of the molecule (S_2) is the ratio between extinction (α_2) and backscattering (β_2).

$$\boldsymbol{S_2} = \frac{\boldsymbol{\alpha_2}}{\boldsymbol{\beta_2}} \tag{A-21}$$

The extinction coefficient of an air molecule is reported as:

$$\boldsymbol{\alpha_2(z)} = \boldsymbol{n(z)}\,\boldsymbol{\sigma_R} = \boldsymbol{n(z)}\,\frac{\mathbf{8\pi}}{\mathbf{3}}\left(\frac{\tilde{\boldsymbol{a}}\boldsymbol{k^2}}{\mathbf{4\pi\varepsilon_0}}\right)^{\mathbf{2}} \tag{A-22}$$

Where parameters n, and σ represent the molecule density and cross-section respectively. The differential cross-section is written in:

$$\frac{\boldsymbol{d\sigma_R}}{\boldsymbol{d\Omega}} = \frac{\mathbf{1}}{\mathbf{1+2\gamma}}\left(\frac{\tilde{\boldsymbol{a}}\boldsymbol{k^2}}{\mathbf{4\pi\varepsilon_0}}\right)^{\mathbf{2}}\left[\{\cos^{\mathbf{2}}\boldsymbol{\theta} + \boldsymbol{\gamma}(\mathbf{1}+\sin^{\mathbf{2}}\boldsymbol{\theta}\}\cos^{\mathbf{2}}\boldsymbol{\varphi} + (\mathbf{1}+\boldsymbol{\gamma})\sin^{\mathbf{2}}\boldsymbol{\varphi}\right] \tag{A-23}$$

For backscattering where $\theta = \pi$, the cross-section in equation (A-23) become:

$$\left(\frac{\boldsymbol{d\sigma_R}}{\boldsymbol{d\Omega}}\right)_{\boldsymbol{\theta=\pi}} = \frac{\mathbf{1+\gamma}}{\mathbf{1+2\gamma}}\left(\frac{\tilde{\boldsymbol{a}}\boldsymbol{k^2}}{\mathbf{4\pi\varepsilon_0}}\right)^{\mathbf{2}} \tag{A-24}$$

Furthermore, the backscattering coefficient is expressed as:

$$\boldsymbol{\beta_2(z)} = \boldsymbol{n(z)}\left(\frac{\boldsymbol{d\sigma_R}}{\boldsymbol{d\Omega}}\right)_{\boldsymbol{\theta=\pi}} = \boldsymbol{n(z)}\frac{\mathbf{1+\gamma}}{\mathbf{1+2\gamma}}\left(\frac{\tilde{\boldsymbol{a}}\boldsymbol{k^2}}{\mathbf{4\pi\varepsilon_0}}\right)^{\mathbf{2}} \tag{A-25}$$

Since the basic principle of molecule lidar ratio in equation (A-21) is governed by inputting extinction in equation (A-22) and backscattering in equation (A-25), the molecule extinction to backscattering ratio is found as:

$$\boldsymbol{S_2} = \frac{\mathbf{8\pi}}{\mathbf{3}}\left(\frac{\mathbf{1+\gamma}}{\mathbf{1+2\gamma}}\right) \tag{A-26}$$

The Chandrasekhar's parameter (γ) is related to the depolarization factor (Δ) through:

$$\boldsymbol{\gamma = \frac{\Delta}{2-\Delta}} \tag{A-27}$$

Consequently, equation (A-26) can be written in:

$$\boldsymbol{S_2 = \frac{8\pi}{3}\left(1 + \frac{\Delta}{2}\right)} \tag{A-28}$$

By assump Δ (air molecule) = 0.0350 in equation (A-28), the lidar ratio of molecule constant is found as 8.25 sr^{-1}.

APPENDIX B : FERNALD METHOD

A Fernald method is an analytical calculation for determining extinction coefficient measured using lidar system. Conventionally lidar data is analyzed by using the Fernald method, in which the lidar equation

$$\boldsymbol{P(z) = \frac{K}{z^2}\left(\beta_1(z) + \beta_2(z)\right)\exp\left[-2\int_0^z \alpha_1(z')dz' - 2\int_0^z \alpha_2(z')dz'\right]} \quad \text{(B-1)}$$

Here, P means the power of light, K is the system constant which is consist of overlapping function. Moreover, parameters z, $X(z)$, and z_c used in this formulation represent the range, range-signal, and range-corrected-signal respectively. Other parameters are employed in this formulation are only mathematics symbol without physical value. To solve the lidar equation, assumption related to extinction (α) to backscattering (β) ratio is defined for both aerosol (S_1) and molecule (S_2):

$$\boldsymbol{S_1 = \frac{\alpha_1}{\beta_1}} \quad \text{(B-2)}$$

$$\boldsymbol{S_2 = \frac{\alpha_2}{\beta_2}} \quad \text{(B-3)}$$

The range corrected signal is defined as:

$$\boldsymbol{X(z) = z^2\, P(z)} \quad \text{(B-4)}$$

By using $P(z)$ in equation (B-1) into equation (B-4), the $X(z)$ is written in:

$$\boldsymbol{X(z) = K\left(\frac{\alpha_1(z)}{S_1(z)} + \frac{\alpha_2(z)}{S_2}\right)\exp\left[-2\int_0^z \alpha_1(z')dz' - 2\int_0^z \alpha_2(z')dz'\right]} \quad \text{(B-5)}$$

Equation (B-4) is written in logarithm, then by substituting equation (B-1), (B-2), and (B-3) in equation (B-4), the result is:

$$\boldsymbol{\ln X(z) = \ln K + \ln\left(\frac{\alpha_1(z)}{S_1(z)} + \frac{\alpha_2(z)}{S_2}\right) - 2\int_0^z \alpha_1(z')dz' - 2\int_0^z \alpha_2(z')dz'} \quad \text{(B-6)}$$

The next definition taken from equation (B-6) is:

$$\boldsymbol{\mu(z) \equiv \frac{X(z)}{\frac{\alpha_1(z)}{S_1(z)} + \frac{\alpha_2(z)}{S_2}}} \quad \text{(B-7)}$$

Equation (B-7) result:

$$\boldsymbol{\alpha_1(z) = S_1(z)\left[\frac{X(z)}{u(z)} + \frac{\alpha_2(z)}{S_2}\right]} \quad \text{(B-8)}$$

Equation (B-7) is used in equation (B-6):

$$\boldsymbol{u(z) = K\exp\left[-2\int_0^z \alpha_1(z')dz' - 2\int_0^z \alpha_2(z')dz'\right]} \quad \text{(B-9)}$$

Equation (B-9) is expressed in logarithm:

$$\ln u(z) = \ln K - 2\int_0^z \alpha_1(z')dz' - 2\int_0^z \alpha_2(z')dz' \quad \text{(B-10)}$$

The result of differentiation to equation (B-10) is:

$$\frac{1}{u(z)}\frac{du}{dz} = -2\,\alpha_1(z) - 2\,\alpha_2(z) \quad \text{(B-11)}$$

Equation (B-8) is substituted in equation (B-11), the result is:

$$\frac{1}{u(z)}\frac{du}{dz} = -2\,S_1(z)\left[\frac{X(z)}{u(z)} + \frac{\alpha_2(z)}{S_2}\right] - 2\,\alpha_2(z) \quad \text{(B-12)}$$

Multiplying both parts of equation (B-12) give the following differential:

$$\frac{du}{dz} = -2\,S_1(z)\left[\frac{X(z)}{u(z)} + \frac{\alpha_2(z)}{S_2}\right]u(z) - 2\,\alpha_2(z)\,u(z) \quad \text{(B-13)}$$

By governing equation (B-13), another differential is obtained in the form:

$$\frac{du}{dz} = 2\left[\frac{S_1(z)}{S_2} - 1\right]\alpha_2(z)\,u(z) - 2\,S_1(z)\,X(z) \quad \text{(B-14)}$$

By assuming a homogeneous case where the 2 $S_1(z)$ $X(z)$ - part is negligible, equation (B-14) is written in:

$$du = 2\left[\frac{S_1(z)}{S_2} - 1\right]\alpha_2(z)\,u(z)\,dz \quad \text{(B-15)}$$

As a homogeneous case, by integrating of equation (B-15) results in an anzats:

$$u = \int 2\left(\frac{S_1(z)}{S_2} - 1\right)\alpha_2(z)\,u(z)\,dz \quad \text{(B-16)}$$

Furthermore, a basic concept about the solution of the differential equation where $du/dz=x$ has a general solution in the form:

$$u(z) = c(z)\,e^{-x} \quad \text{(B-17)}$$

Therefore, the general solution of equation (B-14) inhomogeneous case is

$$u(z) = c(z)\exp\left[-2\int_z^{z_c}\left(\frac{S_1(z')}{S_2} - 1\right)\alpha_2(z')\,dz'\right] \quad \text{(B-18)}$$

Equation (B-18) is substituted into the right part of the equation (B-14), the condition is:

$$\frac{du}{dz} = 2\left[\frac{S_1(z)}{S_2} - 1\right]\alpha_2(z)\,u(z) - 2\,S_1(z)\,X(z) \quad \text{(B-19)}$$

The $c(z)$-parameter is a function to be determined by naming the boundary condition:

$$u(z_c) = c(z_c) \quad \text{(B-20)}$$

The boundary condition in equation (B-20) gives a new anzats by employing equation (B-18):

$$\boldsymbol{c(z) = \frac{u(z)}{\exp\left[-2\int_z^{z_c}\left(\frac{S_1(z')}{S_2}-1\right)\alpha_2(z')\,dz'\right]}} \quad \text{(B-21)}$$

Moreover, by governing anzats in equations (B-18) and (B-21) into equation (B-19) simultaneously, it is given two differential equations in forms:

$$\boldsymbol{\frac{du}{dz} = -2\,S_1(z)\,X(z) + 2\left(\frac{S_1(z)}{S_2}-1\right)\alpha_2(z)\,u(z)} \quad \text{(B-22)}$$

$$\boldsymbol{\frac{dc}{dz} = -2\,S_1(z)\,X(z)\exp\left[-2\int_z^{z_c}\left(\frac{S_1(z')}{S_2}-1\right)\alpha_2(z')\,dz'\right]} \quad \text{(B-23)}$$

The next, Equation (B-23) is written in:

$$\boldsymbol{dc = -2\,S_1(z)\,X(z)\exp\left[2\int_z^{z_c}\left(\frac{S_1(z')}{S_2}-1\right)\alpha_2(z')\,dz'\right]dz} \quad \text{(B-24)}$$

Integrating equation (B-24), defining its exponential part as

$$\boldsymbol{I(z') \equiv 2\int_z^{z_c}\left(\frac{S_1(z'')}{S_2}-1\right)\alpha_2(z'')\,dz''} \quad \text{(B-25)}$$

and considering boundary condition in equation (B-20) gives:

$$\boldsymbol{c = u(z_c) + 2\int_z^{z_c} S_1(z')\,X(z')I(z')dz'} \quad \text{(B-26)}$$

Before continuing to the next step, due to the double integration process, equation (B-24) can be expressed in (only one upper index):

$$\boldsymbol{I(z) \equiv 2\int_z^{z_c}\left(\frac{S_1(z')}{S_2}-1\right)\alpha_2(z')\,dz'} \quad \text{(B-27)}$$

Again, equation (B-27) is involved in equation (B-18) results in a new simple anzats:

$$\boldsymbol{u(z)\exp I(z) = c(z)} \quad \text{(B-28)}$$

Then, by using $c(z)$ in equation (B-27) in equation (B-26) is resulted:

$$\boldsymbol{u(z)\exp I(z) = u(z_c) + \int_z^{z_c} S_1(z')\,X(z')\exp I(z')\,dz'} \quad \text{(B-29)}$$

By defining the right part of the equation (B-29) as:

$$\boldsymbol{J(z) \equiv \int_z^{z_c} S_1(z')\,X(z')\exp I(z')\,dz'} \quad \text{(B-30)}$$

Equation (B-29) can be written in simple form as:

$$\boldsymbol{u(z)\exp I(z) = u(z_c) + J(z)} \quad \text{(B-31)}$$

Since $\alpha_1(z)$ is related to $u(z)$ through equation (B-7) and condition in equation (B-31), the equation for calculating the extinction coefficient of lidar measurement is found:

$$\boldsymbol{\alpha_1(z) = -\frac{S_1(z)}{S_2}\,\alpha_2(z) + \frac{S_1(z)\,X(z)\exp[I(z)]}{\frac{X(z_c)}{\frac{\alpha_1(z_c)}{S_1(z_c)}+\frac{\alpha_2(z)}{S_2}}+J(z)}} \tag{B-32}$$

By substituting $I(z)$ and $J(z)$ of equations (B-27) and (B-30) into equation (B-32), the extinction coefficient formula became:

$$\boldsymbol{\alpha_1(z) = -\frac{S_1(z)}{S_2}\,\alpha_2(z) +}$$

$$\boldsymbol{+\frac{S_1(z)\,X(z)\exp\left[2\int_z^{z_c}\left(\frac{S_1(z')}{S_2}-1\right)\alpha_2(z')\,dz'\right]}{\frac{X(z_c)}{\frac{\alpha_1(z_c)}{S_1(z_c)}+\frac{\alpha_2(z)}{S_2}}+\int_z^{z_c}S_1(z')\,X(z')\exp\left[2\int_z^{z_c}\left(\frac{S_1(z')}{S_2}-1\right)\alpha_2(z')\,dz'\right]dz'}} \tag{B-33}$$

APPENDIX C : TRANSMITTANCE AND RADIANCE

Radiative transfer is the method to separate reflectance of both surface and atmosphere which is derived from satellite remote sensing data. Approximation below evaluate the amount of atmospheric correction by employing single scattering principle. These explanations are divided into transmittance and radiance. The concepts are used in radiative transfer using LOWTRAN (LOw resolution atmospheric radiance and TRANsmittance), 6S (Second Simulation of a Satellite Signal in the Solar Spectrum), MODTRAN (MODerate resolution atmospheric TRANsmission), and RSTAR (System for Transfer of Atmospheric Radiation).

Transmittance

The first formulation about transmittance due to air molecule and aerosol is started from the definition of light transmittance (T) through the atmosphere layer in:

$$\boldsymbol{T_t(\lambda,\theta) = T_m(\lambda,\theta)\, T_a(\lambda,\theta)} \quad \text{(C-1)}$$

Transmittance formulated in equation (C-1) is a function of wavelength (λ) and zenith angle (θ). Indexes t, m, and a are a representation of total, molecule, and aerosol transmittances respectively. Molecule transmittance is defined as:

$$\boldsymbol{T_m(\lambda,\theta) = \exp\left[-\sigma_R(\lambda)\int_0^\infty n(z')\frac{dz'}{\cos\theta}\right] = \exp\left[\frac{-\sigma_R(\lambda)N_c}{\cos\theta}\right]} \quad \text{(C-2)}$$

The new parameters are the column of air molecule (N_c=2.7×1029 m^{-2}) and Rayleigh cross-section (σ_R). Moreover, the Rayleigh cross-section is given as:

$$\boldsymbol{\sigma_R(\lambda) = \frac{8\pi}{3}\left(\frac{\tilde{\alpha}\,k^2}{4\pi\varepsilon_0}\right)^2 = \frac{8\pi}{3}\left(\frac{\tilde{\alpha}}{4\pi\varepsilon_0}\frac{4\pi^2}{\lambda^2}\right)^2 = (4.30\times10^{-31})\left(\frac{550}{\lambda}\right)^4\ [\mathrm{m^2}]} \quad \text{(C-3)}$$

The refractive index ($\tilde{\alpha} / 4\pi\varepsilon_0$) value is 4.30×10^{-31}. By defining optical thickness due to Rayleigh scattering as:

$$\boldsymbol{\tau_R(\lambda) = \sigma_R(\lambda)\, N_c} \quad \text{(C-4)}$$

The general formula of transmittance due to air molecule can be written in:

$$\boldsymbol{T_m(\lambda,\theta) = \exp\left[\frac{-\tau_R(\lambda)}{\cos\theta}\right]} \quad \text{(C-5)}$$

The formulation in equation (C-5) is established for expressing transmittance due to an aerosol by writing:

$$\boldsymbol{T_a(\lambda,\theta) = \exp\left[\frac{-\tau_a(\lambda)}{\cos\theta}\right]} \quad \text{(C-6)}$$

Aerosol optical thickness is developed by using aerosol extinction (α_a) coefficient concept as a function of wavelength (λ) and vertical distribution (z):

$$\boldsymbol{\alpha_a(\lambda,z) = \sigma_a(\lambda)\, n_a(z)} \quad \text{(C-7)}$$

Here, parameters σ_a and n_a are Mie cross-section and aerosol particulate density. Furthermore, by using:

$$\boldsymbol{n_a(z) = \alpha_a(\lambda,0)\exp\left[\frac{-z}{h_a}\right]} \quad \text{(C-8)}$$

In equation (C-7), it is found:

$$\boldsymbol{\alpha_a(\lambda,z) = \sigma_a(\lambda)\,\alpha_a(\lambda,0)\exp\left[\frac{-z}{h_a}\right]} \quad \text{(C-9)}$$

Parameter h_a means the scale height of the vertical aerosol distribution which has the conventional value 2 km. Both $\alpha_a(\lambda,z)$ and $\alpha_a(\lambda,0)$ describe extinction coefficient at high and ground levels respectively. For the ground level, the extinction coefficient related to ground horizontal visibility which is given in:

$$\boldsymbol{\alpha_a(\lambda,0) = \frac{K}{V}\left(\frac{550}{\lambda}\right)^p} \quad \text{(C-10)}$$

The new parameters in equation (C-10) are K as Koschmeider constant (3.912), V as visibility, and p as Ångström exponent. Moreover, the $\alpha_a(\lambda,0)$ in equation (C-10) is used in equation (C-9):

$$\boldsymbol{\alpha_a(\lambda,z) = \sigma_a(\lambda)\frac{K}{V}\left(\frac{550}{\lambda}\right)^p \exp\left[\frac{-z}{h_a}\right]} \quad \text{(C-11)}$$

By considering to altitude, the aerosol optical thickness is obtained by integrating equation of aerosol extinction coefficient:

$$\boldsymbol{\alpha_a(\lambda,z) = \int_0^\infty \sigma_a(\lambda)\frac{K}{V}\left(\frac{550}{\lambda}\right)^p \exp\left[\frac{-z}{h_a}\right] dz} \quad \text{(C-12)}$$

The result is an equation for calculating aerosol optical thickness:

$$\boldsymbol{\tau(\lambda) = K\left(\frac{h_a}{V}\right)\left(\frac{550}{\lambda}\right)^p} \quad \text{(C-13)}$$

By substituting equation (C-13) into equation (C-6), the formula for calculating transmittance due to aerosol is found as:

$$\boldsymbol{T_a(\lambda,\theta) = \exp\left[-\frac{K\,h_a}{V\cos\theta}\left(\frac{550}{\lambda}\right)^p\right]} \quad \text{(C-14)}$$

Radiance

The second formulation about radiative transfer is radiance as a result of reflectance from ground and atmosphere. In this formulation, it is considered the process in which the solar radiation is reflected from the ground surface and reaches the satellite sensor. Formulation is started from the definition that the solar intensity at the top of atmosphere (TOA), E_{TOA} [Wm^{-2}], is equal to the integration of the spectral irradiance, $E(\lambda)$ [Wm^2nm^{-1}], over the entire region:

$$\boldsymbol{E_{TOA} = \int_0^\infty E(\lambda)\, d\lambda} \quad \text{(C-15)}$$

The next step for this formulation is writing the solar flux at the ground (F_0) [$Wm^{-2}\,nm^{-1}$] as irradiance from the sun $E(\lambda)$ affected by the solar zenith angle (θ) and total transmittance due to both molecule and aerosol (T_t) as a function of wavelength and solar zenith angle:

$$\boldsymbol{F_0 = E(\lambda)\cos\theta_s\, T_t(\lambda,\theta_s)} \quad \text{(C-16)}$$

The radiance reflected from surface, $L_g(\lambda,0)$ [$Wm^{-2}sr^{-1}nm^{-1}$] is defined as multiplication of the solar flux in equation (C-16) and the bidirectional reflectance function (BRDF) as a function of wavelength, solar zenith angle, satellite zenith angle, and satellite azimuth respectively, $R(\lambda, \theta_s, \theta_\upsilon, \Delta\varphi)$ as

$$\boldsymbol{L_g(\lambda,0) = F_0\, R(\lambda,\theta_s,\theta_v,\Delta\varphi)\cos\theta_s\, T_t(\lambda,\theta_s)} \quad \text{(C-17)}$$

For the Lambertian scattering where the scattering completely happens, the albedo represented as $\rho(\lambda)$ is given by:

$$\boldsymbol{\rho(\lambda) = \pi\, R} \quad \text{(C-18)}$$

If there is not absorption, $\rho(\lambda) \equiv 1$, as a result, $R=1/\pi$. Consequently, the radiance reflected from the surface is written as:

$$\boldsymbol{L_g(\lambda,0) = \frac{1}{\pi}\, E(\lambda)\,\rho(\lambda)\cos\theta_s\, T_t(\lambda,\theta_s)} \quad \text{(C-19)}$$

Furthermore, by using equation (C-19) radiance reflected by the atmospheric particle is obtained by employing transmittance with the solar zenith angle is

negligible (θ_s=0). Therefore, radiance reflected by the atmospheric particle is given as:

$$\boldsymbol{L_p(\lambda) = \frac{1}{\pi}\, E(\lambda)\, \rho(\lambda) \cos\theta_s\, T_t(\lambda, \theta_s)\; T_t(\lambda, 0)} \quad \text{(C-20)}$$

APPENDIX D : INTERPOLATION METHOD

Linear Interpolation

A basic principle of interpolation is the determination of an unknown point inside of two or more known data by connecting each other. This method is usually called linear interpolation which is schematically figured out in the figure below

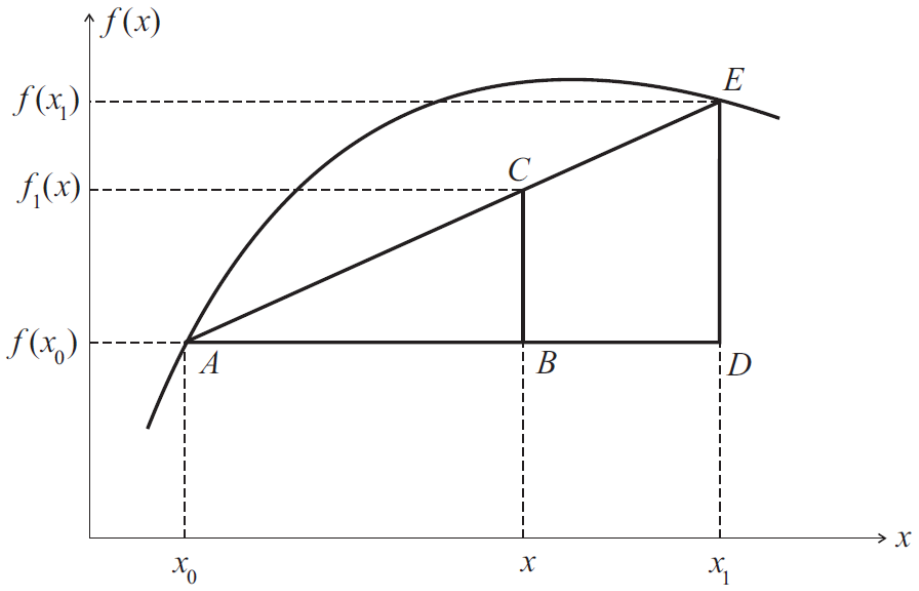

In the figure above, the function value in the two points x_0 and x_1 are $f(x_0)$ and $f(x_1)$. By using linear interpolation, the value of x-point, $f(x_0)$ and $f(x_1)$, can be estimated. Index-1 at $f_1(x)$ represents the order of interpolation, order-1. By involving a geometric concept to the figure, the triangle incongruence of ABC and ADE though comparison:

$$\frac{BC}{AB} = \frac{DE}{AD} \rightarrow \frac{f_1(x)-f(x_0)}{x-x_0} = \frac{f(x_1)-f(x_0)}{x_1-x_0} \quad \text{(D-1)}$$

By governing equation (D-1), we obtain a linear interpolation formula,

$$f_1(x) = f(x_0) + \frac{f(x_1)-f(x_0)}{x_1-x_0}\,(x - x_0) \quad \text{(D-2)}$$

Equation (D-2) is also popular as polynomial interpolation order-1.

Polynomial Interpolation

The polynomial interpolation order-1 in equation (D-2) can be improved to be an order-n. A procedure in obtaining polynomial order-n within n+1 data defining:

$$\boldsymbol{f_n(x) = b_0 + b_1(x - x_0) + b_2(x - x_0)(x - x_1)} + b_3(x - x_0)(x - x_1)(x - x_2) + \cdots + \boldsymbol{b_n(x - x_0)(x - x_1)(x - x_2) \ldots (x - x_{n-3})(x - x_{n-2})(x - x_{n-1})} \quad \text{(D-3)}$$

In equation (D.3), the data $x_0, x_1, x_2, x_3, \ldots, x_{n+1}$ are used for determining the point-n using polynomial order-n. Here, coefficients $b_0, b_1, b_2, b_3, \ldots, b_n$ are estimated using finite difference procedure:

$$\boldsymbol{b_0 = f(x_0)} \quad \text{(D-4)}$$

$$\boldsymbol{b_1 = f[x_1, x_0] = \frac{f(x_1) - f(x_0)}{x_1 - x_0}} \quad \text{(D-5)}$$

$$\boldsymbol{b_2 = f[x_2, x_1, x_0] = \frac{f[x_2, x_1] - f[x_1, x_0]}{x_2 - x_0}} \quad \text{(D-6)}$$

$$\boldsymbol{b_3 = f[x_3, x_2, x_1, x_0] = \frac{f[x_3, x_2, x_1] - f[x_2, x_1, x_0]}{x_3 - x_0}} \quad \text{(D-7)}$$

$$\vdots$$

$$\boldsymbol{b_n = f[x_n, x_{n-1}, x_{n-2}, x_{n-3} \cdots x_3, x_2, x_1, x_0]} = \boldsymbol{\frac{f[x_n, x_{n-1}, x_{n-2}, x_{n-3} \cdots x_3, x_2, x_1] - f[x_{n-1}, x_{n-2}, x_{n-3} \cdots x_3, x_2, x_1, x_0]}{x_n - x_0}} \quad \text{(D-8)}$$

Lagrange Interpolation

Lagrange interpolation is an improvisation of polynomial interpolation which can be formulated by writing the linear interpolation in equation (D-2) to be a finite difference notation:

$$\boldsymbol{f_1(x) = f(x_0) + f[x_1, x_0]\,(x - x_0)} \quad \text{(D-9)}$$

The finite difference notation in equation (D-9) is elucidated in the simple form:

$$\boldsymbol{f[x_1, x_0] = \frac{f(x_1) - f(x_0)}{x_1 - x_0} = \frac{f(x_1)}{x_1 - x_0} + \frac{f(x_0)}{x_1 - x_0}} \quad \text{(D-10)}$$

The right-part of equation (D-10) is substituted into equation (D-9), then governing it in the form of Lagrange interpolation order-1 below:

$$\boldsymbol{f_1(x) = \frac{x - x_1}{x_0 - x_1} f(x_0) + \frac{x - x_1}{x_1 - x_0} f(x_1)} \quad \text{(D-11)}$$

The order-1 of Lagrange interpolation in equation (D-10) can be improved in orders-2 and -3 below:

$$\boldsymbol{f_2(x)} = \frac{x-x_1}{x_0-x_1}\frac{x-x_2}{x_0-x_2}\boldsymbol{f(x_0)} + \frac{x-x_0}{x_1-x_0}\frac{x-x_2}{x_1-x_2}\boldsymbol{f(x_1)} + \frac{x-x_0}{x_2-x_0}\frac{x-x_1}{x_2-x_1}\boldsymbol{f(x_2)} \quad \text{(D-12)}$$

$$\boldsymbol{f_3(x)} = \frac{x-x_1}{x_0-x_1}\frac{x-x_2}{x_0-x_2}\frac{x-x_3}{x_0-x_3}\boldsymbol{f(x_0)} + \frac{x-x_0}{x_1-x_0}\frac{x-x_2}{x_1-x_2}\frac{x-x_3}{x_1-x_3}\boldsymbol{f(x_1)}$$
$$+ \frac{x-x_0}{x_2-x_0}\frac{x-x_1}{x_2-x_1}\frac{x-x_3}{x_2-x_3}\boldsymbol{f(x_2)} + \frac{x-x_0}{x_3-x_0}\frac{x-x_1}{x_3-x_1}\frac{x-x_2}{x_3-x_2}\boldsymbol{f(x_3)} \quad \text{(D-13)}$$

The procedure in the three lower orders above can be used for developing Lagrange interpolation order-*n*:

$$\boldsymbol{f_3(x)} = \frac{x-x_1}{x_0-x_1}\frac{x-x_2}{x_0-x_2}\frac{x-x_3}{x_0-x_3}\cdots\frac{x-x_n}{x_0-x_n}\boldsymbol{f(x_0)} + \frac{x-x_0}{x_1-x_0}\frac{x-x_2}{x_1-x_2}\frac{x-x_3}{x_1-x_3}\cdots\frac{x-x_n}{x_1-x_n}\boldsymbol{f(x_1)}$$
$$+ \frac{x-x_0}{x_2-x_0}\frac{x-x_1}{x_2-x_1}\frac{x-x_3}{x_2-x_3}\cdots\frac{x-x_n}{x_2-x_n}\boldsymbol{f(x_2)} + \frac{x-x_0}{x_3-x_0}\frac{x-x_1}{x_3-x_1}\frac{x-x_2}{x_3-x_2}\cdots\frac{x-x_n}{x_3-x_n}\boldsymbol{f(x_3)}$$
$$+ \cdots + \frac{x-x_0}{x_n-x_0}\frac{x-x_1}{x_n-x_1}\frac{x-x_3}{x_n-x_3}\cdots\frac{x-x_{n-1}}{x_n-x_{n-1}}\boldsymbol{f(x_n)} \quad \text{(D-14)}$$

Coefficients in equation (D-14) are represented in multiplication ceres,

$$\boldsymbol{L_i(x)} = \prod_{\substack{i=0 \\ i\neq j}}^{n} \frac{x-x_j}{x_i-x_j} \quad \text{(D-15)}$$

As a result, we obtain a general form of Lagrange interpolation:

$$\boldsymbol{f_n(x)} = \sum_{i=0}^{n} \boldsymbol{L_i(x)f(x_i)} \quad \text{(D-16)}$$